NTNU – Trondheim
Norwegian University of
Science and Technology

Development of a compact radiation monitor for space application

Timo Alexander Stein

MSc in Physics	
Submission date:	June 2015
Supervisor:	Ingve Simonsen, IFY
Co-supervisor:	Gunnar Maehlum, Integrated Detector Electronics AS

Norwegian University of Science and Technology
Department of Physics

Development of a Compact Radiation Monitor for Space Application

by

Timo A. Stein

- M. Sc. Thesis -

Submitted in Partial Fulfilment of the Requirements
for the Degree of M. Sc. in Physics

Department of Physics at
Norwegian University of Science and Technology
June 2015

Trondheim, Norway

To all the patient people who believe in me,
in particular Anastasiya and our familiy ...

... and to our dog Daika.

She thought it would be a great idea to play ”hide and seek” in the streets of Trondheim one hour before the submission deadline.

Abstract

In this work a compact radiation monitor prototype has been developed. The present device and its technology will directly contribute towards the CPT-SCOPE project, a Norwegian-German student project developing a radiation monitor for space application.

The present design utilises an application specific integrated circuit (ASIC) which provides a low-power and small-form factor solution. Such system is required for small satellites and CubeSats. The development of the device has been carried out in multiple design steps.

A functioning radiation monitor prototype has been developed, implemented and tested. First measurements of cosmic ray background, beta particle and low-energetic gamma ray sources verify its functionality.

This marks a major milestone towards a compact radiation monitor for nanosatellites. While this work deals with a technology demonstrator, it directly contributes to the CPT-SCOPE project.

The finished CPT-SCOPE instrument and its flight aboard BEXUS 20 in October 2015 will be the next milestone. In the future this should lead towards CPT-SCOPE 2.0, a CubeSat-ready compact radiation monitor.

The project demonstrated the usability of COTS components in hybrid with specialised, radiation-hard integrated circuits for radiation detection. This approach allows for rapid and inexpensive developments for small satellite and CubeSat instrumentation.

Preface

The present master thesis has been submitted in partial fulfilment of the requirements for the degree of Master of Science (M.Sc.) in Physics to the Department of Physics at the Norwegian University of Science and Technology (NTNU). The project has been carried out during the time period of September 2014 and June 2015. A specialisation project on the used integrated circuit has been done in the summer of 2014 [54].

The work has been carried out as collaboration with the Integrated Detector Electronics AS (IDEAS), an Oslo-based company specialised in radiation-hard integrated circuit technology and its application for radiation detection. Hence relevant work was done in Oslo and Trondheim.

In addition, the project directly contributes towards the Norwegian-German Cosmic Particle Telescope (CPT-SCOPE) project. CPT-SCOPE was established by the author during the summer of 2014 and aims at creating a functioning radiation monitor to fly aboard the BEXUS 20 mission in October 2015. This allows for the present work to be directly utilised within a research project rather than being purely academic in its nature.

The last year has been exciting and challenging. It has led to the first selected Norwegian BEXUS proposal by the European Space Agency (ESA). Several conference presentations and proceedings have already been authored about the project.

Acknowledgements

The presented work is interdisciplinary with a focus on physics, electronics and software development. Such project relies on the help and mentorship of numerous people that have assisted me along the way: First and foremost, I would like to thank my supervisors Prof. Ingve Simonsen (NTNU) and Gunnar Mæhlum (IDEAS). I am thankful to IDEAS for providing the necessary resources and beyond. I have had the most fruitful collaboration with many IDEAS employees. In particular I would like to express my gratitude to Dirk Meier (detector physics), Tor Magnus Johansen and Bahram Najafiuchevler (VHDL programming), Codin Gheorghe, Philip Påhlsson, David Steenari, Petter Øya (electronics) and Willy Dang (wire bonding).

This work would not have been possible without the great CPT-SCOPE team, namely: Michael Beermann, Anastasiya Dykyy, Fabian Freyer, Lucas Kempe, Arnstein Kleven, Julian Petrasch, Patrick Schönberg, Johannes Stahn, Anton Walter, Ron Wenzel and Grunde Wesenberg.

For this master thesis in particular the programming contribution done by Julian Petrasch has helped to control the configuration of the ASIC. He has spent uncountable hours at IDEAS during a work placement in spring 2015.

Lastly, I would like to thank my family which has always been supportive and understanding. Their patience is truly infinite and I am most grateful to have such great and loving people around me.

My work has been financially supported by the Studienstiftung des Deutschen Volkes which granted me a full scholarship for my studies. Furthermore, IDEAS has been the main sponsor on this project providing free lab access and office space for CPT-SCOPE as well as major financial support for material and parts.

The CPT-SCOPE project has also been supported by Sparebanken Midt-Norge, the Anette og Brynjulf Skaugens Veldedige Stiftelse, NUUG, SNSB / DLR / ESA, Numato Lab, Ikalogic, Advanced Energy Industries, WIMA, First Sensor AG, Webspace-Verkauf.de, with additional contributions of other sponsors and partners to which the CPT-SCOPE team is grateful.

Table of Contents

List of Tables

List of Figures

Abbreviations

AC	Alternating Current, coupling via capacitor
ADC	Analog-to-Digital Converter
Al	Aluminium
Am	Americium
ASIC	Application-Specific Integrated Circuit
BEXUS	Balloon EXperiment for University Students
BG	Background
Cd	Cadmium
Cf	Californium
CMOS	Complementary Metal-Oxide-Semiconductor
Co	Cobalt
COTS	Commercial Off-The-Shelf
CPS	Counts per second
CPT-SCOPE	Cosmic Particle Telescope
Cs	Caesium
CS	Chip Select (SPI)
CSA	Charge Sensitive (Pre-)Amplifier
CSV	Comma-separated values
CZT	Cadmium zinc telluride, CdZnTe
DAC	Digital-to-Analog Converter
DC	Direct Current
DFF	Data Flip-flop
EC	Electron Capture
EM	Electromagnetic
ENC	Equivalent Noise Charge
ESA	European Space Agency
ESD	Electrostatic Discharge
Eu	Europium
Fe	Iron
FF	Flip-Flop
FPGA	Field-Programmable Gate Array
FS	First Sensor AG
FSM	Finite State Machine
GND	Ground (elec.)
GPIO	General Purpose Input and Output
HDL	Hardware Description Language
HMRM	Highly Miniaturized Radiation Monitor
IAEA	International Atomic Energy Agency

IC	Integrated Circuit
IC	Integrated Circuit
IDEAS	Integrated Detector Electronics AS
IEEE	Institute of Electrical and Electronics Engineers
JUICE	JUpiter ICy moons Explorer
LDO	Low-dropout regulator
LSB	Least Significant Bit
LUT	Look-up table
MIP	Minimum ionising particles
MISO	Master In Slave Out (SPI)
MOSFET	Metal-Oxide-Semiconductor Field-Effect Transistor
MOSI	Master Out Slave In (SPI)
MSB	Most Significant Bit
MUX	Multiplexer
NASA	National Aeronautics and Space Administration
NGRM	Next Generation Radiation Monitor
NTNU	Norwegian University of Science and Technology
NUTS	NTNU Test Satellite
OBC	On-Board Computer
OS	Operating System
PATA	Parallel ATA
Pb	Lead
PCB	Printed Circuit Board
PET	Polyethylene-terephthalate
PP	Polypropylene
PPS	Polyphenylene-Sulphide
PSU	Power Supply Unit
REXUS	Rocket EXperiment for University Students
ROIC	Readout Integrated Circuit
S-G	Savitzky-Golay filter
S/N	Signal to Noise ratio
SCLK	Serial Clock (SPI)
SD	Secure Digital
SEL	Single Event Latch-up
SEU	Single Event Upset
Si	Silicon
SI	International System of Units
SMD	Surface Mounted Device
SoC	System on a chip
SPI	Serial Peripheral Interface
Sr	Strontium
sr	Steradian
SRL	Shift Register LUT
SSH	Secure Shell
Tl	Thallium

UTC	Coordinated Universal Time
VATA	IDEAS ASIC combining VA- and TA-technology
VHDL	VHSIC Hardware Description Language
VHSIC	Very High Speed Integrated Circuit
XRF	X-Ray Fluorescence

Symbols

μ	total linear attenuation coefficient
(μ/ρ)	(total) mass attenuation coefficient
κ	linear attenuation coefficient due to pair production
λ	wavelength, decay constant, mean free path
λ_C	Compton wavelength
ν	frequency
σ	linear attenuation coefficient due to Compton scattering
ρ	density
τ	mean lifetime, linear attenuation coefficient due to photoelectric absorption
A	mass number
C	capacitance
l	absorber thickness
L	mass thickness
I	current, intensity
N	neutron number, number of radioactive atoms / photons / particles etc.
U	voltage
r	distance, radius
$t_{1/2}$	half-life time
t	time
Q	charge, Q-value (available energy)
X	chemical symbol (original radioisotope)
Y	chemical symbol (daughter radioisotope)
Z	atomic mass number

Physical Constants

Symbol	**Name**	**Value**	**Unit**
c	Speed of light in vacuum	299792458	$\mathrm{m\,s^{-1}}$
e	Electron charge magnitude	$1.602176565(35)\times10^{-19}$	C
k_B	Boltzmann constant	$1.3806488(13)\times10^{-23}$	$\mathrm{J\,K^{-1}}$
h	Planck's constant	$6.62606957(29)\times10^{-34}$	J s
		$= 4.135\times10^{-15}$	eV s
m_e	Electron mass	0.510998828(11)	MeV $\mathrm{c^{-2}}$
m_p	Proton mass	938.272046(21)	MeV $\mathrm{c^{-2}}$
m_n	Neutron mass	939.5653(79)	MeV $\mathrm{c^{-2}}$

All constants taken from Ref. [8].

Chapter 1

Introduction

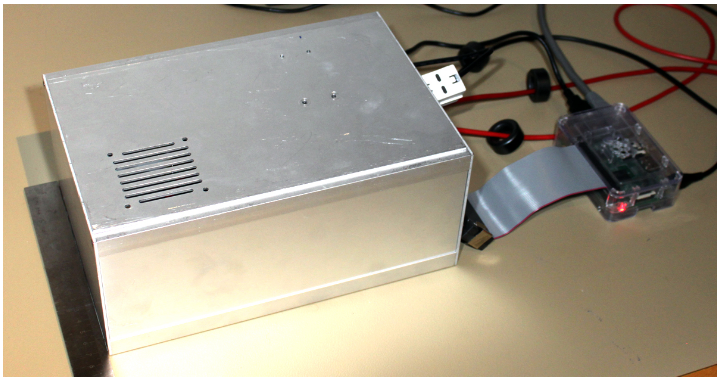

Figure 1.1: Finished technology demonstrator in its metal casing with attached OBC and external power supply.

1.1 Overview

The present thesis describes the development of a technology demonstrator for a particle radiation detector tailored for space application. The device is based on a reverse-biased silicon (Si) diode, front-end electronics using a radiation-hard VATA application-specific integrated circuit (ASIC), a FPGA-based back-end and a Raspberry Pi B+ as on-board computer (OBC) which allows remote-access to the device via Ethernet. The device also aims at simplifying data handling and allowing for high count rates by utilising threshold-based trigger counting instead of conventional analogue-to-digital conversion with required post-processing for each event. The detector is sensitive to energetic subatomic particles such as electrons, and low-energetic gamma rays. The main goal of the demonstrator is to test key technologies for a future miniature radiation detector to be used on nanosatellites. The finished technology demonstrator is shown in Fig. 1.1 inside its metal housing with the external OBC and power supply cables.

Conventional space-rated radiation monitors are too large, power consuming or expensive for nanosatellites. This type of spacecraft represent a new space industry trend towards smaller and less expensive solutions. It also allows private enterprises and educational institutions to carry out space missions.

In order to meet the nanosatellite requirements new instrumentation needs to be developed and implemented. Such devices must rely on state-of-the-art integrated circuit (IC) technology for true miniaturisation, in combination with low-cost and rapid development approaches such as the usage of commercial off-the-shelf (COTS) components.

Within the project the aforementioned subsystems were combined to create a functioning technology demonstrator for test and validation of key technologies. The successful completion of the device required an interdisciplinary approach involving physics, electronics, mechanical and software engineering. The presented thesis also uses results obtained in a previous specialisation project by the author [54]. The project aimed at characterising the VATA465 ASIC in regard to its temperature and input-frequency response in the summer of 2014.

Furthermore, the technology developed within this thesis work will directly contribute to the Norwegian-German Cosmic Particle Telescope (CPT-SCOPE) instrument. The project will produce a prototype compact radiation monitor to study energetic particle in the stratosphere. The CPT-SCOPE device is based on a stack of absorbers and silicon sensors, also known as particle telescope. The instrument is developed by eleven students from Trondheim, Norway and Berlin, Germany. It has been selected in December 2014 by an expert panel of the European Space Agency (ESA) to fly aboard the BEXUS 20 mission in October 2015. The Balloon EXperiment for University Students (BEXUS) is a German-Swedish collaboration with ESA support allowing up to six student teams from ESA-member states to launch their experiment annually aboard two stratospheric research balloon from Kiruna, Sweden. Ultimately this shall lead to CPT-SCOPE 2.0 a compact radiation monitor for nanosatellites.

Possible applications of the developed technology are within space weather monitoring, atmospheric physics, dosimetry and the protection space assets.

Furthermore, the present tests of the VATA-family ICs helps to characterise the ASIC and its response. The VATA465 successor ASIC (VATA466) is selected to fly aboard the ESA JUpiter ICy moons Explorer (JUICE) mission which is set for launch in 2022. The ASIC will be used for the RADEM instrument to measure energetic protons and electrons. JUICE will explore the environment of the Jovian moons which are important for planetary science and an improved understanding of the solar system's evolution.

Lastly, the creation of a compact radiation monitor for nanosatellites would be a direct consequence of the technology demonstrator and the CPT-SCOPE project.

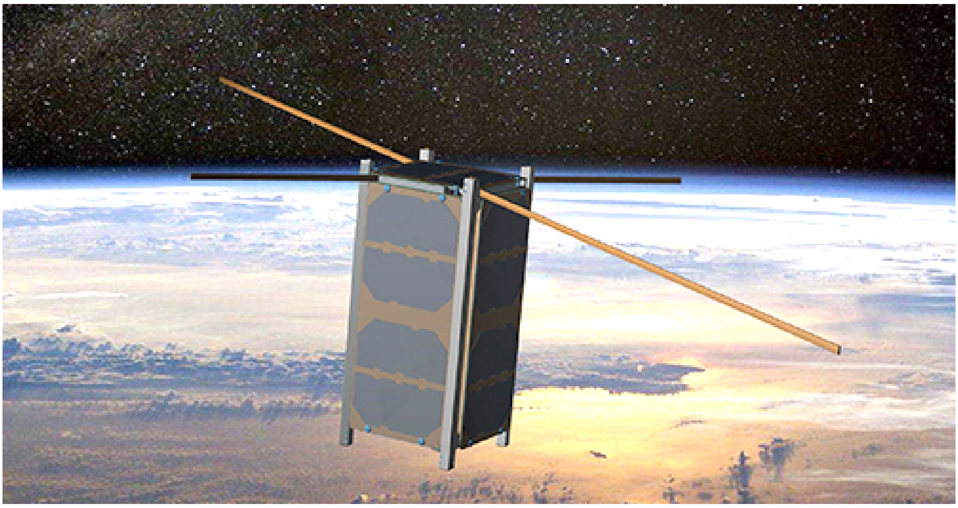

Figure 1.2: Artistic rendering of the NUTS CubeSat, this family of nanosatellites fullfil more and more important tasks in space. The size of this 2U CubeSat is not larger nore heavier than a regular 1.75l milk container. Credit: NUTS.

1.2 Motivation

Satellites have a critical importance in our everyday life. From navigation and telecommunications to earth observation and fundamental research, mankind has seen many technological advancements due to pushing the space frontier.

Sputnik 1 (COSPAR ID: 1957-001B) was developed by the Soviet Union bringing the Cold War Space Race with the United States of America to full speed. On October 4, 1957, it became the first satellite launched into orbit. Its main body was an aluminium sphere with 58 cm in diameter and four external antennas. The satellite weighted 83.6 kg. In today's standard it would be classified as microsatelltite. The satellite was able to transmit radio signals at 20.005 MHz and 40.002 MHz for about three weeks before the internal batteries failed. At the time discrete electronics were in use and the technology was in an early stage.

The advancement of several key space technologies occurred at a fast paste over the next decades. Today even highly complex satellites such as the ESA ENVISAT (COSPAR ID: 2002-009A) carrying ten payloads for earth observation have been successfully launched into space. At a total weight of ca. 8.2 tons, dimensions of 26 m x 10 m x 5 m and over 3 kW in available solar cell power it was the largest civilian satellite built by ESA so far. It operated from 2002 until 2012, delivering important data to map our planet and study its environment. The project cost are estimated at 2.3 billion Euro with a development time of some 10 years [20].

Today the industry trend shifts towards micro- and nanosatellites [12] which have a rapid development cycle of only 1-3 years. In addition, one accepts higher risks for failure in order to cut costs significantly to 1-7 M£ for micro- and 0.1-1 M£ for nanosatellites, respectively. These emerging satellite types require miniature electronics and low-cost approaches.

The Norwegian University of Science and Technology (NTNU) works since 2010 on the NTNU Test Satellite (NUTS) [9]. This satellite belongs to the group of nanosatellites, known as CubeSats [59]. It is a 2U CubeSat which is developed by NTNU students. As a result of a NUTS future payload study in which the author was involved the idea for the present master thesis project and CPT-SCOPE arose. The author then established with fellow students the CPT-SCOPE project in which, by now, eleven students work jointly in Berlin, Germany and Trondheim, Norway. Both the NUTS and CPT-SCOPE projects address the emerging and dynamic nanosatellite community.

Lastly, contact was established with the Integrated Detector Electronics AS (IDEAS), an Oslo-based company specialised in radiation-hard integrated circuit technology for space application. They offer a wide range of ASIC solutions among users for radiation detector front-end electronics. The IDEAS VATA465 ASIC was ideal for the development of CPT-SCOPE. In order to achieve the goal of implementing a prototype compact radiation monitor the ASIC needed to be characterised and a technology demonstration be carried out within a student project. This is done within the present master thesis work.

1.3 Goals

The project aims at implementing key technologies in order to create a functioning technology demonstrator, namely using:

- the VATA465 ASIC as front-end electronics solution,
- and COTS components to facilitate the back-end, control and detection.

The device shall be able to detect:

- low-energetic gamma rays,
- charged subatomic particles such as electrons or muons.

These goals shall be achieved within the given time frame of the master thesis which equals to approx. one year.

1.4 Publications and Technical papers

This master thesis has directly contributed to several technical papers, presentations and conference contributions. Many of those are related to the CPT-SCOPE project. A list of relevant technical documents, papers and presentations is listed below:

Paper:

- R. Birkeland, T.A. Stein, M. Beermann, A. Gjersvik, J. Petrasch and M. Tømmer: ”The NUTS Cubesat Project: Spin-offs and Technology Development”, Proceedings of the 22nd ESA PAC Symposium, Jun. 2015. See [9].

Technical papers:

- T.A. Stein *et. al.*: ”Student Experiment Documentation (SED): CPT-SCOPE”, BEXUS experiment documentation, Jun. 2015.
- T.A. Stein: ”Report for Physics - Special Syllabus (FY3490): Characterisation of the IDEAS ASIC VATA465 with focus on temperature and input-signal frequency response”, term paper, unpublished. See [54].

Presentations (selection):

- T.A. Stein: ”CubeSat-ready Radiation Monitor Front-End Electronics”, 6th European CubeSat Symposium, Oct. 2014. See [55].
- G. Wesenberg, T.A. Stein, *et. al.*: ”The Cosmic Particle Telescope (CPT-SCOPE) - a Norwegian-German compact radiation monitor for small satellite application developed by students”, Nordic Physics Days, Jun. 2015.
- T.A. Stein: ”Space Activity at NTNU: International Collaboration and Opportunity for Norway”, Talk at the Permanent Mission of Norway in Geneva, unpublished, Jan. 2015.

A number of papers and conference participations are planned within the CPT-SCOPE project.

Chapter 2

Background and Literature Review

This section will explore the necessary background, both scientific and technical, to provide a solid foundation for the remaining chapters.

2.1 Scientific background

2.1.1 Radioactivity

Radioactivity describes the disintegration of a radioisotope. The most common decay modes are the α-, β- and γ-decay. Often this leads to changes of the radioisotope's inner structure and the emission of subatomic particle and/or gamma rays.

The subject of radioactivity is covered in a number of text books. The main source of this section is [36]. Decay schemes and relevant information can be obtained from numerous sources online f.i. from the International Atomic Energy Agency (IAEA) - Nuclear Data Section[1] or the LBNL Isotopes Project - LUNDS Universitet Nuclear Data Dissemination Home Page[2]. All relevant decay schemes for this work are taken from [4–7, 36].

2.1.1.1 Introduction

We will now describe the activity of a radioactive source assuming a single decay process and not considering the contribution of daughter nuclei etc. Under these assumptions the

---

[1] IAEA - Nuclear Data Section web page: `https://www-nds.iaea.org/`

[2] Link: `http://ie.lbl.gov/toi.html`

activity is defined by the change in the number of mother nuclei $N(t)$ as function of time t via a simple differential equation:

$$\frac{dN(t)}{dt} = -\lambda N(t). \tag{2.1}$$

If the decay constant λ is constant its solution is an exponential decay with an initial number of nuclei $N_0 = N(t = 0)$:

$$N(t) = N_0 \cdot \exp\left(-t/\lambda\right). \tag{2.2}$$

The decay constant λ is henceforth assumed to be constant. It is easily converted to a mean life time τ:

$$\tau = \frac{1}{\lambda}. \tag{2.3}$$

After time $t = \tau$ only ca. 36.8% (=$exp(-1)$) of the original radioactive atoms have not yet decayed. A more convenient measure is the half-life time $t_{1/2}$ which is defined as:

$$t_{1/2} = \ln 2 \cdot \tau = \frac{\ln 2}{\lambda}. \tag{2.4}$$

After time $t_{1/2}$ has passed only half of the initial nuclei are present. The unit of radioactive activity is the becquerel (Bq) which is defined as one decay per second. The historic unit is curie (Ci) which is defined as the activity of 1 g of the radioisotope $^{226}\mathrm{Ra}$. The conversion between becquerel and curie is as follows:

$$1\,\mathrm{Bq} = 2.703 \cdot 10^{-11}\,\mathrm{Ci} \quad \Leftrightarrow \quad 1\,\mathrm{Ci} = 3.700 \cdot 10^{10}\,\mathrm{Bq}. \tag{2.5}$$

Common submultiples are mili- (mCi) and microcurie (μCi), as well as kilo- (kBq) and megabecquerel (MBq).

It should be noted that not every disintegration leads to a single emission of decay products or photons. For example a single decay may result in two gamma rays being emitted by the source. Therefore the knowledge of the radioisotope's decay scheme is of vital importance.

The energy in nuclear / particle physics applications is commonly measured in electron volts (eV). The conversion between the SI-unit joule (J) is as follows:

$$1\,\mathrm{eV} = 1.602 \cdot 10^{-19}\,\mathrm{J} \quad \Leftrightarrow \quad 1\,\mathrm{J} = 6.242 \cdot 10^{18}\,\mathrm{eV}. \tag{2.6}$$

Typical kinetic energy values for radioactive decay products are of the order of 0.1 MeV to 10 MeV. Gamma rays from 1 keV to 10 MeV. The Planck relation links the energy of a photon E_γ to its wavelength λ or frequency f via the speed of light c and the Planck's constant h as follows:

$$E_\gamma = h \cdot f = \frac{h \cdot c}{\lambda}. \tag{2.7}$$

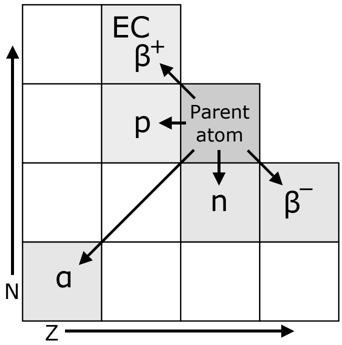

Figure 2.1: Radioactive decay modes. Credit: User MarsRover, Wiki Commons, under GNU free documentation license, `http://en.wikipedia.org/wiki/File:Radioactive_decay_modes.svg`

2.1.1.2 Radioactive Decay Modes

A nuclide ${}^{A}_{Z}\mathrm{X}_{N}$ is described by the chemical element symbol ”X”, its mass number A and the number of protons Z and neutrons N located in the atomic nucleus. These numbers are related by a simple relation: $A = Z + N$. It is common to drop N and/or Z since A along with the chemical symbol ”X” are sufficient to identify the nuclide. Therefore the strontium (Sr) radioisotope ${}^{90}_{38}\mathrm{Sr}_{52}$ is fully described by ${}^{90}\mathrm{Sr}$ or Sr-90.

A radioisotope decays after a finite time. The individual disintegration may appears at random time intervals. However, in large numbers it behaves in a stochastic fashion with specific properties and parameters such as the half-life time. Every radioisotope may have various decay channels which create one or more daughter nuclei each. It also changes the composition of the nuclide which may or may not transform the daughter nucleus into another chemical element.

Common decay modes are shown in Fig. 2.1 where the number of $\{$neutrons, protons$\}$ increases $\{$bottom to top, left to right$\}$. The daughter nucleus is different from the parent atom in either Z, N or both.

The available energy, also known as Q-value (Q), for the disintegration of the parent atom determines possible daughter products and their kinetic energy. Also reactions with a large Q-value have often a shorter life-time unless the transition is forbidden by quantum mechanics.

We will now outline the reactions associated to the common decay channels, namely the α-, $\beta^{\pm}$- and γ-decay, or via electron capture (EC).

2.1.1.2.1 α-decay

This decay results into the emission of an alpha particle (${}^{4}_{2}\alpha$, short: α) which correspondents to a ^{4}He nucleus. It is caused by the α-particle to have successfully tunnelled through the nuclear potential barrier. This process is described by the following decay:

$$\alpha\text{−decay}: \quad {}^{A}_{Z}\mathrm{X} \quad \rightarrow \quad {}^{\mathrm{A-4}}_{\mathrm{Z-2}}\mathrm{Y} + \alpha, \tag{2.8}$$

where X and Y are the initial and final nucleus, respectively. This decay mode is only common for heavy radioisotopes such as Am-241. The energy of the emitted alphas is discrete and often appearing in groups due to varying energies in the final state of the daughter nucleus Y. Typical energy values of commonly used alpha emitters are between 4 and 6 MeV. Alpha particles interact strongly with matter and are easily stopped by a piece of paper.

2.1.1.2.2 $\beta^{\pm}$-decay

The emission of an energetic electron or positron occurs in the β^- and β^+ decay, respectively. These are described by the following processes:

$$\beta^-\text{−decay}: \quad {}^{A}_{Z}\mathrm{X} \quad \rightarrow \quad {}^{\mathrm{A}}_{\mathrm{Z+1}}\mathrm{Y} + \bar{\nu}_{\mathrm{e}} + \mathrm{e}^-, \tag{2.9}$$

$$\beta^+\text{−decay}: \quad {}^{A}_{Z}\mathrm{X} \quad \rightarrow \quad {}^{\mathrm{A}}_{\mathrm{Z-1}}\mathrm{Y} + \nu_{\mathrm{e}} + \mathrm{e}^+. \tag{2.10}$$

with X and Y being the initial and final nucleus. Note that the $\{\beta^-, \beta^+\}$-decay is producing, in addition to the {electron (e^-), positron (e^+)}, an electron {anti- ($\bar{\nu}_e$), neutrino (ν_e)}. This is due to the fact that the process is mediated by the weak force where the total lepton number needs to be conserved. A more fundamental treatment of the β energy spectrum can be found in [26].

The neutrino interacts only via the weak force and is therefore for all practical purposes assumed to be not detectable. Only the β-particle can be measured.

Since the mass of the daughter nucleus is in all practical cases dominant over the mass of the remaining byproducts it experiences virtually no recoil. Hence in a β^--decay all available energy is provided to both the electron and electron antineutrino, and shared among them. This leads to a continuous spectrum for the β-particle kinetic energy. Its value varies between zero and the end-point energy $E_\beta^{(\mathrm{max})}$. The spectrum is asymmetric with an average energy $E_\beta^{(\mathrm{avg})}$.

Often the decay can lead to several final states where the daughter nuclide is in an excited state. In such case gamma rays with discrete energy are emitted shortly after the first transition took place. This leads to overlapped β-spectra with varying end-point energies due to the difference in available energy Q for the primary β-decay byproducts.

In a few radioisotopes the direct transition from the parent to the daughter nuclide's ground state dominates. These produce so called pure beta emitter f.i. the thallium (Tl) isotope Tl-204. They have clean beta spectra with a well defined end-point energy.

Beta activity is easily created by neutron bombardment and a wide range of radioisotopes are available. The entire range of life-times is covered and end-point energies are typical of the order of 100 keV to several MeV. The $\{\beta^-, \beta^+\}$ is dominant for {neutron, proton}-rich nuclides. Since the rest mass of the electron / positron m_e is approx. 511 keV/c^2 beta particles are often relativistic, moving close to the speed of light c. Therefore beta particles can penetrate deeper into material. They are easily stopped by a thin sheet of aluminium (Al).

The β^+-decay creates a positron which quickly annihilates when interacting with local electrons. This creates two gamma rays of 511 keV, corresponding to the rest mass of the involved electron and positron, respectively. These gamma rays will appear in the recorded gamma spectra as annihilation peaks.

2.1.1.2.3 EC-decay

Electron capture (EC, ε) is a similar and competing process to the β^+-decay. It converts an internal u- into a d-quark via the weak force, effectively transmuting a proton into a neutron. However, it does so by capturing a bound, inner shell electron and emitting a monoenergetic electron neutrino. The process is outlined as follows:

$$\mathrm{EC-decay:}\quad {}^{A}_{Z}\mathrm{X} + \mathrm{e}^- \quad \rightarrow \quad {}^{\mathrm{A}}_{\mathrm{Z-1}}\mathrm{Y} \, + \, \nu_{\mathrm{e}}. \tag{2.11}$$

In this case only a not detectable neutrino is produced. However, the daughter nuclide is left in an excited state in the majority of cases, causing the emission of secondary gamma or X-rays with discrete energies. A good example for this is the iron (Fe) isotope Fe-55.

The EC decay is always possible when the β^+-process is. However, when the available energy $Q < 2m_ec^2$ only the EC mode is allowed since the energy is not sufficient to create a positron[3].

2.1.1.2.4 γ-decay

Daughter nuclides are often in an excited energy state. Such metastable state is followed by the relaxation to a lower or the ground state. This is carried out via various pathways: Commonly the de-excitation occurs with the emission of gamma rays. Less common, but possible, are internal conversion processes (see below).

A gamma ray is an energetic photon with energy E_γ. The energy threshold between X- and gamma rays is varying around 10 keV - 100 keV. The main difference between X-rays and gamma rays lies in their origin. While the former is based on atomic processes, such as shell electron reordering due to inner shell vacancies, the latter stem from nuclear processes which - generally speaking - occur at higher energies. Optical light photons, for comparison, have a significantly smaller energy on the order of 1 eV.

Gamma rays produced by the γ-decay of radioisotopes generate a discrete line spectrum. Each gamma line is caused by a transition of the daughter nuclide between different excited and the ground state where the final state (n_f) is always lower than the initial one (n_i). The energy of the emitted gamma ray E_γ is due to the energy difference ΔE:

$$E_\gamma = \Delta E = E_f - E_i. \tag{2.12}$$

---

[3] The minimum Q-value of $Q = 2m_ec^2$ stems from the fact that in the β^+-decay one needs to account for the mass of both the beta particle (positron) and an additional electron in the daughter nuclide (atom vs. nuclear masses).

Several decay pathways and hence number of lines are possible. Each of them has varying transition probabilities, potentially leading to complex gamma spectra. Each radioisotope has a characteristic gamma spectrum which can be used for identification purposes. Note that i) although attributed to the parent nuclide the gamma rays are actually emitted by the daughter nuclide - example see below; ii) the life time of these excited states are of the order of pico- to nanoseconds making the gamma emission appear virtually instantaneous as compared to many common beta or alpha emitter's half-life time of seconds to hundreds of years which justifies i).

Below some additional decay modes are presented. No processes to obtain neutrons will be discussed.

2.1.2 Interaction in Matter

Subatomic particles interact with matter. Their characteristic behaviour differs greatly both depending on the particle type and interaction partner i.e. the absorber or scatterer. Charged particles interact significantly more than uncharged ones. Similarly, heavier particles have a much shorter characteristic distance and hence are stopped after a shorter distance than low- or even massless particles.

In this section we will elaborate important concepts relevant for measurements taken within the framework of this thesis and provide an overview on the underlying processes. These are described with focus on β-particles, i.e. fast electrons and positrons, as well as on high-energetic photons, i.e. X- and gamma rays. Heavier particles such as alphas will not be discussed in great detail since they are not part of the later measurements. These are discussed in great detail in [8, 36, 45]

2.1.2.1 Charged particle interactions

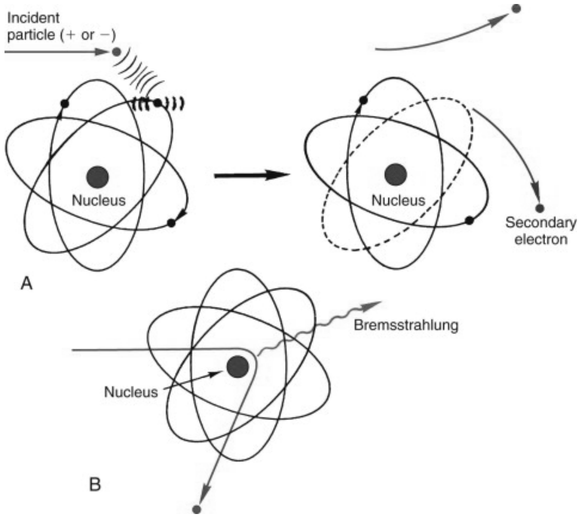

Figure 2.2: Selected interaction processes of charged particle in matter: (A) excitation, (B) ionisation and (C) radiative losses. Source: [14].

When a charged particle enters matter it immediately starts interacting with its surrounding via the electromagnetic force (EM). In particular the electrons of the bulk material are susceptible for Coulomb interactions due to their low mass and relatively small binding energy. The charged particle may excite its interaction partner i.e. the shell electron changes energy level (excitation) but remains bound, or it ionises an absorber atom and removes a shell electron (ionisation). This is shown in Fig. 2.2. At each interaction the primary particle losses a small amount of its kinetic energy. This eventually leads to the complete loss of energy for an absorber with infinite thickness.

However, when either the particle energy E is very high or the absorber thin the primary particle may only loose a fraction of its energy ΔE.

The differential energy loss is also known as linear stopping power S which is the defined as:

$$S = -\frac{dE}{dx}. \tag{2.13}$$

The above rate is the specific energy loss. Classically, the Bethe formula is used to describe the energy loss:

$$-\frac{dE}{dx} = \frac{4\pi e^4 z^2}{m_e v^2} \cdot NZ \left[\ln\left(\frac{2m_e v^2}{I}\right) - \ln\left(1 - \frac{v^2}{c^2}\right) - \frac{v^2}{c^2} \right]. \tag{2.14}$$

Here we identify the variables as follows: the absorber material average excitation and ionisation energy I, the velocity v and charge z or the primary particle, the number density N and atomic number Z of the absorber material, the electron rest mass m_e and electron charge e [36]. The bracket term only varies slightly with the energy of the incident particle, while the behaviour is dominated by the velocity square term in the first denominator of Eq. (2.14). For non-relativistic particles such as alphas only the first bracket term contributes ($v \ll c$). One can also see that particles with higher charge will have a larger specific energy loss. Conversely, heavier materials will absorb the energy of a charged particle stronger due to their increased electron density ($N\ Z$).

The specific energy loss is a function of the primary particle energy and type for fixed absorber material parameters. A broad minimum of S exists which correspondents to a value of approx. $S = 2$ MeV / (g/cm^2) (cf. Fig. 2.1 in [36]). Particles located in this minimum are also known as minimum ionising particles (MIP) [36]. The minimum extends over a wide range of energies and depends on the type of particles. Fast electrons with energies on the order of 1 MeV are also considered as MIPs since they travel with relativistic speed at these energies already.

The Bethe formula is valid over a wide range of energies. However, at low energies charge exchange becomes dominant and positive and negative primary particles exhibit a significantly different behaviour. Likewise at high energies radiation effect become dominant. Nevertheless, for all practical purposes within this work the Bethe formula is sufficient.

The graph showing the stopping power S as function of the penetration depth x is called a Bragg curve. For many particles the energy loss increases as they slow down. This decelerates them even faster leading to a rapid energy loss for low energies. When the particle is stopped the stopping power drops to zero since all energy is entirely deposited inside the absorber. From the characteristic behaviour of particles they species can be determined or likewise for a given particle source the aborber / target can be investigated.

Another important concept is the range R_l. It describes the distance a particle group of monoenergetic particles has to pass through a material in order to absorb half of them. Its numerical value depends on the primary particle type, energy and absorber material.

For a thin absorber the energy deposition inside of the material ΔE can be approximated by the average stopping power and absorber thickness l:

$$\Delta E = -\left(\frac{dE}{dx}\right)_{avg} \cdot l. \tag{2.15}$$

For small specific energy loss values i.e. MIPs the initial value of S for the particle's energy can be used. The case of the thin absorber is relevant in many applications such as particle detectors. For example a high energetic muon from atmospheric cosmic ray interactions has an average energy on the order of 1 GeV. For this particle the used silicon sensor of 250 μm will appear as thin and no significant energy loss will be suffered by the particle. Nevertheless, the passage will create enough electron-hole pairs to create enough signal current for a detection. This approximation also be used for many instrument estimates.

2.1.2.1.1 Stopping power for fast electrons

In this work we will test the radiation monitor prototype using beta emitters. These are fast electrons interacting with matter along its way f.i. the detector. For these particles additional aspects have to be considered. This is due to their low mass which makes a deflection by nuclei likely. The direction of the particle may change significantly. Hence the path taken by betas is usually more spread out as compared to heavy particles such as alphas. This behaviour requires modification of the Bethe formula in Eq. (2.14). Furthermore, radiative losses due to Bremsstrahlung or other EM waves emitted along the way lead to energy loss which need to be accounted for (see Fig. 2.2). Both modifications are relevant for a detailed study. However, for the scope of this project they go to far and these are not further discussed. References can be found in textbooks such as [8, 27, 28, 36].

Due to the deflections the behaviour of betas in terms of absorption is quite different. Even for thin absorber material betas are scattered. The amount of absorbed betas increases continuously. Furthermore, is the modelling complicated by the fact that betas are emitted over a continuous range of energies as compared to alphas which are for all practical purposes considered monoenergetic. Hoewever, due to their lower mass the effective stopping power at identical kinetic energy is still much lower than for heavy particles. Therefore betas can penetrate a material much deeper. As a rule of the range of betas are 2mm or 1 mm per MeV for a low-Z and medium-Z material respectively [36]. This needs to be considered when beta source must be shielded. The betas may also backscatter due to the possibility for large angle deflections. For beta(+) particles the stopping power is similar to their negative counterparts. However, when the positron is slowed down it will annihilate and create two gamma rays with an energy of 511 keV each.

2.1.2.2 High-Energetic Photons

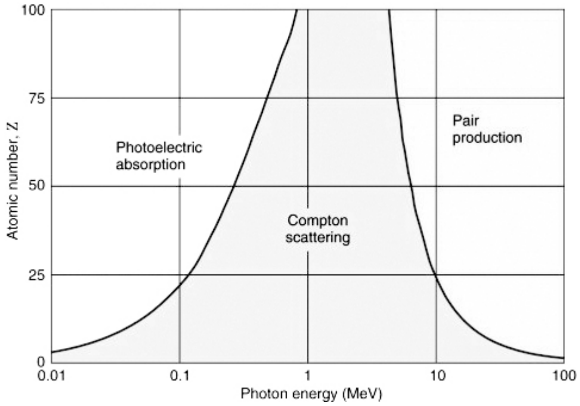

Figure 2.3: Graph indicating the dominant interaction process for gamma rays as function of energy E_γ and the absorber material atomic number Z. Source: [14].

The following section will outline the major interaction mechanisms and absorption of gamma rays. Excellent resources for further reading about this section are [2, 36, 44, 49, 60].

Gamma photons interact different than particles with matter. There are four major interaction mechanisms:

- photoelectric effect,
- Compton scattering,
- and pair production

Other effects such as the high-energetic photodisintegration will not be covered. A in depth discussion of the fundamental concepts from the particle physics perspective are covered in textbooks such as [26].

We will now briefly outline all four processes and their relevance in our application. Each occurs at different energies and depend on the density of the material.

2.1.2.2.1 Photoelectric effect

The gamma ray can be absorbed by an inner shell electron which is tightly bound. This releases a so-called photoelectron. The photon energy E_γ must be at least equal to the electron's binding energy E_b. The available remainder is the kinetic energy of the photoelectron E_e:

$$E_e = E_\gamma - E_b. \tag{2.16}$$

Consequently, sharp absorption edges are created where the photon energy drops below the binding energy of the K-, L-, M-shell etc. The binding energy of the absorber material increases with its atomic number Z. Therefore heavy materials such as lead (Pb) are used for gamma ray shielding. The characteristic energies for many elements are tabulated in [60].

The created electron vacancy is filled by reordering of the remaining electrons. In this process characteristic X-rays with lower energy than the incident gamma ray are emitted. In addition, Auger electrons may be released during the atomic relaxation. The photoelectric effect can only appear for bound electrons.

The photoelectric absorption only occurs for low energetic gamma rays close to the binding energy E_b of the absorber material. Typical values for the K-shell are 88 keV (Pb, Z=82), 7. keV (Fe, Z=26) or 1.8 keV (Si, Z=14); L- or M-shell values are substantially lower [60].

This process is hence dominant for low-energetic gamma rays of energies lower than 100 keV. It further explains as to why high-Z materials such as the semiconductor cadmium zinc telluride (CdZnTe, CZT) are used for gamma detectors.

2.1.2.2.2 Compton scattering

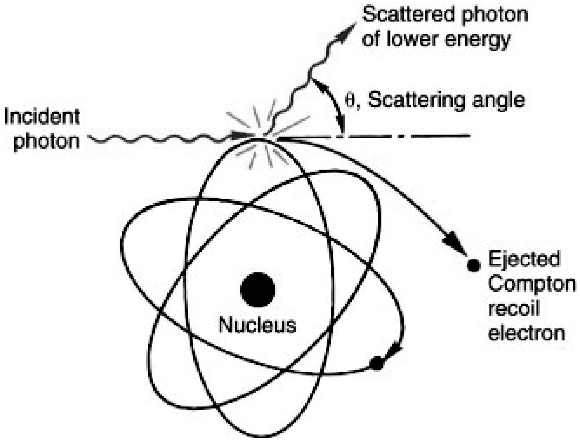

Figure 2.4: Sketch for Compton scattering. Source: [14].

Incident gamma rays with energy E_γ may be scattered by electrons inside the detector, the surroundings or both. For the rest of the paragraph we only study the case that the gamma ray has not yet interacted with matter and experiences scattering only inside the detector. There are three possible cases:

- i) both the electron and scattered gamma ray deposit their full energy,
- ii) only the recoil electron is detected and the scattered photon escapes or
- iii) *vice versa*.

The first case (i) contributes to the so-called photopeak where the full gamma ray energy E_γ is measured. In the remaining two cases energy is lost to the environment as it escapes the detector. We will only study case ii) since the escape of an electron (iii) is only possible when it close to the detector surface.

When a gamma ray is scattered by an electron the photon transfers part of its momentum. The energy of the scattered photon $E_\gamma^{'}$ is lower or equal than the original one: $E_\gamma^{'} \leq E_\gamma$. This is due to the conservation of the four momentum x^μ i.e. the simultaneous conservation of energy and momentum. When assuming the original electron at rest and free i.e. not bound to an atom or bulk material the scattered photon energy $E_\gamma^{'}$ is given by:

$$E_\gamma^{'} = \frac{E_\gamma}{1 + \frac{E_\gamma}{m_e c^2} \left(1 - \cos\theta\right)}. \tag{2.17}$$

Here represents m_e the electron rest mass (ca. 511 keV/c^2), c the speed of light and θ the angle between the direction of the incident and scattered photon. A sketch for the Compton scattering is shown in Fig. 2.4. The value of θ is in the range of $[0, \pi]$, with $\theta = 0$ indicating no and $\theta = \pi$ maximal scattering and hence largest energy loss of the photon.

Commonly the Compton effect and its mathematical expression is written in terms of the gamma rays' wavelength λ and $\lambda^{'}$ for the initial and scattered photon, respectively. For this one utilises the relationship between the wavelength λ, frequency ν and the speed of light c (vacuum): $c = \lambda \cdot \nu$. Using this relation we arrive at the following expression for the wavelength of the initial and scattered photon [16]:

$$\lambda^{'} = \lambda + \frac{h}{m_e c} \left(1 - \cos\theta\right) \tag{2.18}$$

$$= \lambda + \lambda_c \left(1 - \cos\theta\right). \tag{2.19}$$

In Eq. (2.19) λ_c stands for the Compton wavelength which is determined by the Planck's constant h, electron mass m_e and the speed of light.

It should be noted that the above Eqs. (2.17), and (2.19) are derived in the electrons rest-frame. However, in many cases the gamma ray is scattered by a (weakly) bound electron inside the absorbing layer such as the detector (see above assumption). Hence these models require a modification. This is discussed in chapter 13 of [36]. For all practical purposes of this thesis the above model is sufficient. The angular distribution of the Compton effect is described by the Klein-Nishina formula (not shown) [35, 36]. The ability of a material to create Compton scattering is proportional to the local electron density. Hence high-Z materials such as lead scatter more than low-Z material. Qualitatively, the effect is not dependent on the atomic number Z.

The effect of Compton scattering is evident in gamma spectroscopy as it creates several distinct features. Among them are i) the a Compton continuum - escaped scattered gamma rays, and ii) the Compton edge. Due to complications in the detector response function a number of other features may appear such as backscatter or escape peaks. Other effects such as X-ray fluorescence (XRF) of surrounding material or detector may further contaminate the obtained gamma spectrum. These issues may be reduced by methods such as Compton suppression where anti-coincidence is used to only detect non-scattered gammas.

The Compton edge represents the maximal possible energy of the recoil electron. It is caused by the photon being backscattered i.e. $\theta = \pi$. The energy of the backscattered photon as compared to its original value is given by:

$$E_\gamma^{(min)}/E_\gamma = \left(1 + (2E_\gamma)/(m_e c^2)\right)^{-1} .$$

Generally speaking, Compton scattering creates a continuous background with the well defined Compton edge. As a consequence weaker low-energetic spectral features may be obscured by the Compton scattering of a strong high-energetic peak.

The Compton effect is scaled by the electron rest mass m_e and the energy of the incident gamma ray E_γ as seen in the denominator of Eq. (2.17). This makes it the dominant gamma ray interaction for energies of 100 keV and 10 MeV.

2.1.2.2.3 Pair creation

When the gamma ray E_γ energy exceeds the equivalent of twice the electron rest mass (= 1.022 MeV) the creation of an electron-positron pair becomes possible. The pair production, however, becomes only dominant for energies above 10 MeV. Furthermore, the pair creation must take place in the direct proximity of a nucleus where the gamma ray is absorbed completely. There is no simple expression describing the probability of pair creation. However, its likelihood increases with the atomic number Z for fixed E_γ. The remaining energy of the absorbed gamma ray is provided to the electron and positron as kinetic energy.

The produced positron quickly annihilates with an electron creating two photons with an energy of $E_\gamma = 511$ keV, also known as annihilation peaks. The photons are emitted normal to each other in the pair rest frame.

2.1.2.2.4 Gamma ray attenuation

In the following paragraph we will outline different attenuation coefficients for gamma rays and their intensity as function of distance r. The main resources for this paragraph are [36, 44].

Linear attenuation coefficient

For an absorber of thickness l the number of gamma rays with energy E_γ, expressed as N, reduces exponentially with l:

$$N(E_\gamma) = N_0(E_\gamma) \cdot \exp\left(-\mu(E_\gamma, Z, \rho) \cdot l\right). \tag{2.20}$$

This is due to the fact that the total linear attenuation coefficient μ is constant to first order for a fixed gamma ray energy E_γ [36]:

$$\frac{\mathrm{dN(E_\gamma)}}{\mathrm{dl}} = -\mu(E_\gamma, Z, \rho) \cdot N(E_\gamma). \tag{2.21}$$

Table 2.1: Overview on linear attenuation coefficients (Lin. atten. coeff.) and their underlying process.

Process	**Lin. atten. coeff.**
Photoelectric absorption	τ
Compton scattering	σ
Pair production	κ
Total	μ

In this simplified treatment we will only consider the first three processes by which gamma rays may interact with matter. It should be noted that the total linear attenuation coefficient μ is the sum of all of the above processes:

$$\mu = \tau + \sigma + \kappa. \tag{2.22}$$

We identify the individual linear attenuation coefficients in Tab. 2.1. Their value changes as function of gamma energy E_γ, the absorber material (Z) and its density (ρ) as discussed above. For brevity they have been dropped in Eq. (2.22).

The attenuation of gamma rays can also be described using the mean free path λ. This reflects the average distance a photon traverses before it interacts. It is simply the inverse of the total linear attenuation coefficient:

$$\lambda = \frac{1}{\mu}. \tag{2.23}$$

Mass attenuation coefficient

In the above treatment the linear attenuation coefficient also depends on the absorber density ρ. However, the material attenuation coefficient remains the same for identical Z

absorber. As an example water has the same mass attenuation coefficient whether it is in a liquid, solid or gaseous state [36]. The mass attenuation coefficient is the quotient of the linear attenuation coefficient and density: (μ/ρ). It is physically the more meaningful parameter since it only depends on the gamma energy (E_γ) and material (Z).

For mixtures the compound mass attenuation coefficient $(\mu/\rho)_c$ can be calculated via the individual weight fractions w_i and mass attenuation coefficients $(\mu/\rho)_i$:

$$\left(\frac{\mu}{\rho}\right)_c = \sum_i w_i \cdot \left(\frac{\mu}{\rho}\right)_i \qquad \text{with } \sum_\mathrm{i} \mathrm{w_i} = 1. \tag{2.24}$$

In this form Eq. (2.20) can be rewritten to:

$$N = N_0 \cdot \exp\left[-\left(\frac{\mu}{\rho}\right) \cdot \rho \cdot l\right] \tag{2.25}$$

$$= N_0 \cdot \exp\left[-\left(\frac{\mu}{\rho}\right) \cdot L\right] \qquad \text{with L} = \rho \cdot \text{l}. \tag{2.26}$$

For historic reasons the unit for the mass attenuation coefficient (μ/ρ) is cm^2/mg. These are tabulated f.i. in [30]. Due to the better physical meaningfulness one often introduces a mass thickness L (units: mg/cm^2) instead of the physical absorber length l as shown in Eq. (2.26).

Intensity as function of distance

For a point source in vacuum the intensity $I(r)$ i.e. the number of photons per unit surface as function of distance r would simply fall off over its square:

$$I(r) = \frac{I_0}{r^2}. \tag{2.27}$$

However, when an absorber is present such as in the case of gamma rays travelling through lead shielding the observed intensity is a product of both geometric factors (source and instrument geometry / distribution, distance) as well as the above described absorption / scattering processes.

For typical low-energetic gamma rays the mean free path[4] λ in dry air is large e.g. approx. 40 m for E_γ=50 keV and 680 m for E_γ=1 MeV. In this way one can often neglect the absorption through air. This is, however, not true for low-energetic X-rays or subatomic particles and even air absorption needs to be considered.

Furthermore, the source geometry may restrict the allowed solid angle and hence also influences the intensity as function of distance $I(r)$.

---

[4] Assuming: $\rho^{(\mathrm{air})}$=1.225 g/cm^3; (μ/ρ)=0.2 cm^2/g at E_γ=50 keV and (μ/ρ)=0.06 cm^2/g at E_γ=1 MeV from [30].

2.2 Technical background

2.2.1 Semiconductor Radiation detectors

This section is an adapted version from the author's previous specialisation report, see [54].

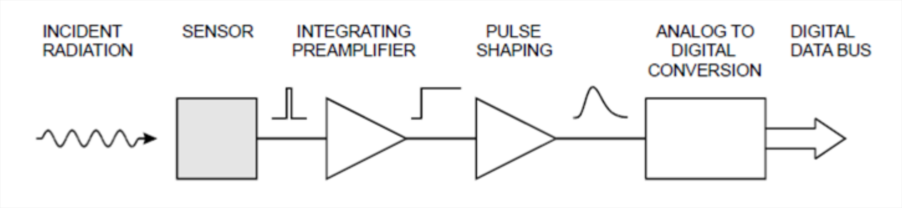

Figure 2.5: Overview of front-end electronics for signal processing in radiation detectors. Source: [52]

There is a variety of ways to detect ionising radiation such as Geiger-Müller-counters or scintillators-coupled photomultiplier tubes. A historic review is given in [24] showing nicely the evolution within the field. Henceforth, we will describe the underlying principles of a semiconductor radiation detector and provide an overview of its parts. The instrument is supposed to measure sub-atomic particles, namely electrons, protons or heavier ions, with sufficient energy as to create electron-hole pairs in a semiconductor active layer.

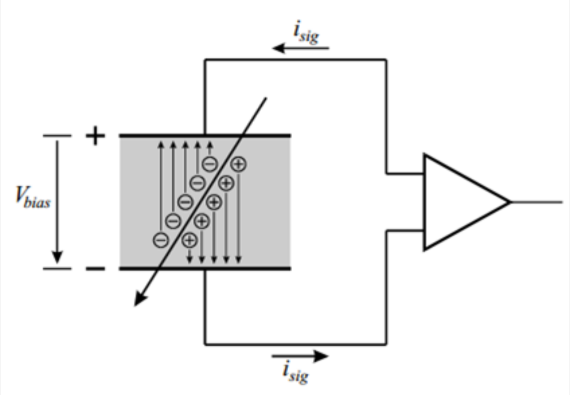

Figure 2.6: Sketch of functioning principle of semi-conductor-based radiation detectors. Source: [52]

An overview of the signal processing steps including all relevant components for such device are shown in Fig. 2.5. Almost exclusively a reverse-biased and fully depleted semiconductor diode serves as sensor as shown in Fig. 2.6. The incident particles enter the sensor and lose energy due to interaction with the absorber medium. Along their trajectory (indicated by the arrow) electron-hole pairs ($\oplus, \ominus$) are formed which drift apart and towards one of the electrodes due to the electric field created by the applied reverse-bias voltage V_{bias}. As charge is collected a current pulse i_{sig} is formed which is detected and amplified by a high-gain, low-noise charge sensitive pre-amplifier (CSA). At this stage the signal pulse, proportional to the total charge Q, is registered. A pulse-shaper modifies the signal's frequency spectrum to reduce noise. After several amplification stages and pulse shaping the charge signal is converted into digital data for further processing. These steps are carried out by the front-electronics of the system for each channel of the instrument i.e. for each sensor. Other sub-systems are necessary to provide power or carry out further data processing e.g. using an on-board computer (OBC) or field-programmable gate array (FPGA) as counter etc. The electronics attached to the front-end is known as back-end.

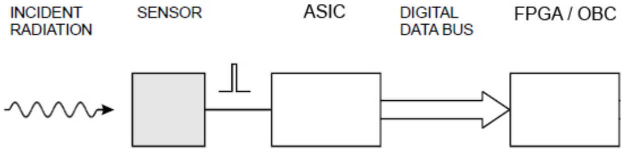

Figure 2.7: Front-end electronics sketch using ASIC for read-out. This leads to a highly integrated solution. Source: [54]

For a multi-channel design a large number of components, space, power consumption and heat dissipation result for a conventional discrete component approach. Furthermore, system performance and noise characteristics are likely worse compared to a highly-integrated design. Hence, using integrated circuit technology is the only viable option for satellite instrumentation. In the present design most of the signal processing and conditioning is carried out inside the ASIC which also allows to implement multi-channel capabilities. The new signal processing chain is shown in Fig. 2.7 and shows the highly integrated nature of this approach (cf. Fig. 2.5).

An excellent resource for semiconductor detectors is [36] and for the electronics the following reference is recommended [52].

2.2.2 IDEAS VATA465

This section is an adapted version from the author's previous specialisation report, see [54].

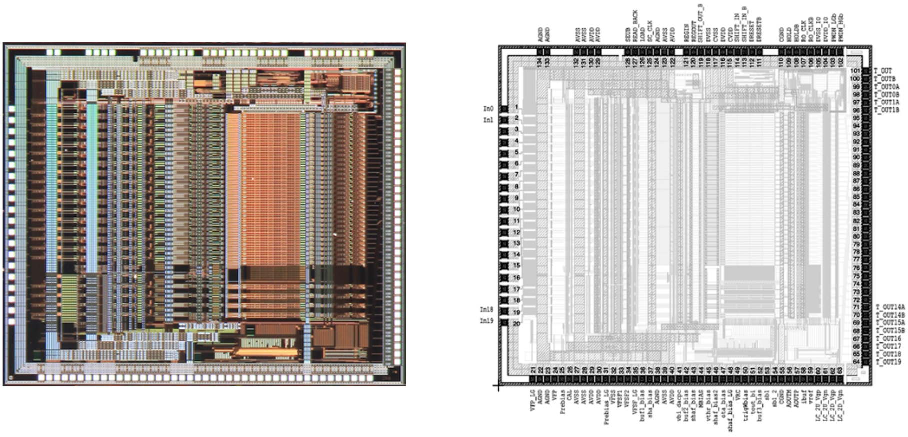

Figure 2.8: Photograph of VATA465 ASIC cut die (left) and pad overview (right). The inputs (**INx**, x={0,19}) are located on the left while one can find the individual channel outputs (**T-OUTxA/B**, x={0,15}; **T-OUTx**, x={16,19} and 'all-channel-ORed' outputs **T-OUT/B** to the right. Additional ports for configuration and testing are located on the top and bottom. Source: IDEAS

The ASIC will serve as critical part of in front-end electronics responsible for signal amplification, shaping and detection. The principles of the ASIC VATA-family are shown in Fig. 2.9 (left) and specifically for the VATA465 in Fig. 2.9 (right).

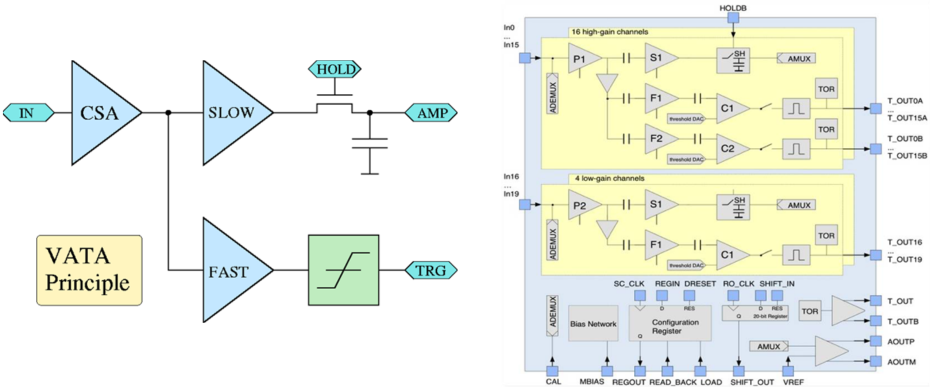

Figure 2.9: Overview over VATA family operation principles (left) and the detailed schematic for the VATA465 (right). Source: IDEAS

VATA ASICs are able to carry out energy spectroscopy and on-chip triggering for programmable thresholds on each input channel. The ASIC is radiation hard against single event upsets (SEU) by design and manufacture via custom component layouts, triple redundancy and error self-correction. The VATA465 is based on 0.35 μm CMOS technology and has dimensions of approx. 6.0 mm x 7.1 mm. A photograph is shown in Fig. 2.8 (left). The corresponding pad labels are provided in Fig. 2.8 (right).

For the VATA465 there are 20 inputs for positive charge carriers labelled INx (x=$\{0,19\}$) as indicated in Fig. 2.8 (right). Of those the first 16 channels (x=$\{0,15\}$)) are high-gain while the remaining 4 inputs (x=$\{16,19\}$)) are low-gain channels optimised for low-input charges of max. 2.6 pC and 26.0 pC, respectively.

Each input signal is amplified by a charge-sensitive amplifier (CSA, Px)[5] and then provided to a slow (cf. Fig. 2.9 top left, Sx, peaking time: ca. 1 μs) or fast shaper (bottom left, F1/F2; peaking time: ca. 250 ns). The slow shaper provides the signal to sample-and-hold circuitry (SH) which is connected to an analogue multiplexer (AMP, AMUX) for external energy spectroscopy i.e. the individual signal amplitudes are measured via an external analogue-to-digital converter (ADC).

The fast shaper supplies the amplified pulse to on-chip triggers. These consist of two comparators (C1/C2) which compare the signal amplitude to a generated analogue threshold value using an 8-bit digital-to-analogue converter (DAC). By combining two such comparator stages in parallel a window function can be achieved i.e. only signals within a specific range are registered (only available for high-gain channels INx, x=$\{0,15\}$). Each comparator has its own output terminal T_OUTxA for C1 and T_OUTxB for C2. The low-gain channels do not feature a window-function since only one comparator (C1) exists with output terminals T_OUTx (x=$\{16,19\}$). If the signal is in the allowed range a logical one (true) is provided as output, otherwise a logical zero (false). In addition the output T_OUT goes high (logical true) if any trigger is activated (TOR). The device can be configured via a 356-bit register which defines the mode of operation, DAC threshold values etc.

For the high-gain channel, low-threshold trigger outputs (T_OUTxA) a technical issue is present for some configuration which is relevant for this project: Due to an overshoot of the fast shaper output the lower threshold may retrigger several times for a single energetic event. This can be fixed by introducing a dead time counter to prevent the registration of erroneous triggers. The suggested dead time is 10 - 20 μs depending on the detector system and sample[6].

---

[5] Note that annotation in Fig. 2.9 left and right are different. The first refers to the general VATA sketch (left) and the second to the VATA465 specific one e.g. (CSA=VATA; Px=VATA465).

[6] Personal communications with D. Meier, Feb. 2015.

To summarise, the device key features are (cf. data sheet [41]):

- 20 charge-sensitive pre-amplifiers (CSA):
  - 16 high-gain inputs (positive charge, max. Q=2.6 pC),
  - 4 low-gain inputs (positive charge, max. Q=26 pC).
- 37 digital logic triggers (tested in this work):
  - 36 fast shapers (250 ns) and comparators,
  - 32 outputs with 2 thresholds (window-function, high-gain channels),
  - 4 outputs with 1 thresholds (low-gain channels),
  - 1 trigger from OR of all channels,
  - minimum rate capability 25 kcps/channel with 20 per cent loss.
- Pulse-height spectroscopy:
  - 20 slow shapers (1 μs) followed by sample-and-hold,
  - analogue multiplexer output from all channels,
  - maximum rate capability 2.5 kcps/channel.
- low-power operations: max. 65 mW, depending on settings/rate,
- radiation hard by design and manufacture (SEL/SEU).

For more details the VATA465 data sheet can be consulted [41].

2.3 Available Compact Radiation Monitors

At the present stage there is no low-cost, European compact radiation monitor available for small satellites and CubeSats.

Existing solutions or technology demonstrators which have flown in space are f.i. the US-American Relativistic Electron and Proton Telescope integrated little experiment (REPTile) which flew aboard the CSSWE CubeSat [39], the Relativistic Electron-Proton Telescope (REPT) [3] on board the NASA RBSP spacecraft or the European Standard Radiation Environment Monitor (SREM) [43]. However, those either do not fulfil the CubeSat requirements [13] (SREM, REPT) or do not utilise IC technology for true miniaturisation (REPTile, REPT). In particular the findings of the CSSWE mission are outstanding and proof that CubeSats can contribute to high-quality research. The above points led us to start our own instrument development.

The only known and substantially developed European compact radiation monitor which meets CubeSat standards is the Highly Miniaturized Radiation Monitor (HMRM) [29, 42] developed at Rutherford Appleton Laboratory and Imperial College London. Their technology is fully custom-made and is highly specialised. However, at 52 g, 20 mm x 25 mm x 30 mm in size, and requiring 1 Watt of power, it characteristics are promising. However, no in-flight have been published yet.

Our approach is quite different to HMRM, and uses a hybrid of COTS and specialised rad-hard IC technology. Developing a better alternative for the exiting radiation monitors and allowing the device to be CubeSat-ready are a good driving force for the outlined project.

2.4 CPT-SCOPE

This section is taken from [9]. The CPT-SCOPE section has been written by author and is used with permission.

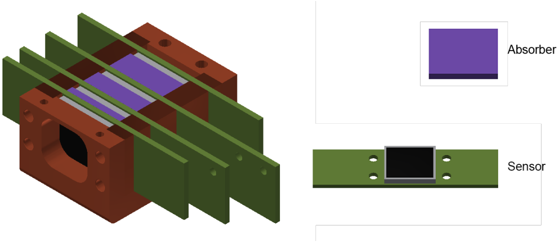

Figure 2.10: The mechanical design of one CPT-SCOPE particle telescope featuring four sensor modules (green). The absorbers are shown in purple and the mechanical support structure in red.

2.4.0.1 Overview

The Cosmic Particle Telescope (CPT-SCOPE) is a compact radiation monitor prototype for applications in atmospheric and space research. The instrument idea stems from efforts within the NUTS CubeSat project to investigate future payloads for small satellites and CubeSats. In mid-2014 CPT-SCOPE[7] started as first NUTS spin-off. In this project twelve students from Trondheim, Norway, and Berlin, Germany, work jointly.

In December 2014 the instrument has been selected as one of six European payloads to fly aboard the BEXUS[8] 20/21 mission. The launch of the two stratospheric balloons from Kiruna, Sweden, is planned for October 2015. The BEXUS programme aims at emulating a real ESA space mission realised by university students. Hence, the focus lies not exclusively on technical development or science but on project management, finances, proposal writing, outreach and verification.

Due to the short project life-cycle of less than one year the strategy was to use as many commercially available, low-cost components as possible. In regard of project management and sponsorship procurement numerous lessons learned from the NUTS project were successfully implemented, accelerating the project progress significantly.

2.4.0.2 Objectives

Mission statement: CPT-SCOPE shall measure the variable flux of energetic subatomic particles in the stratosphere while demonstrating the capabilities of a new radiation-hard

---

[7] CPT-SCOPE webpage: `http://www.cpt-scope.com/`.

[8] The Balloon Experiments for University Students (BEXUS) is a bilateral cooperation of the Swedish SNSB and German DLR with support of ESA. It is part of the annual REXUS/BEXUS program allowing student teams from ESA member states to test their experiments on sounding rockets and stratospheric balloons.

IDEAS VATA-family application-specific integrated circuit (ASIC) regarding future space missions.

Objectives (P - primary, S - secondary):

- **P1**: Build a functioning radiation monitor based on an IDEAS VATA46x ASIC and silicon sensors.
- **P2**: Establish bi-directional communication during the BEXUS flight.
- **P3**: Test the particle telescope capabilities and trigger pattern concept.
- **P4**: Measure the flux of energetic subatomic particles in the stratosphere.
- **S1**: Determine the particle species and their individual flux as function of energy.
- **S2**: Measure the altitude dependent flux of each particle species.
- **S3**: Compare results to simulations and other (BEXUS) experiments.

In addition to these scientific and technical objectives, the CPT-SCOPE projects has a strong outreach and education component. Two science teacher students are involved in giving space-related presentations, carrying out simple experiments and building a cloud chamber for the visualisation of subatomic particles in the classroom.

2.4.0.3 Technical Description

The instrument is for redundancy purposes built from two identical systems which act complementary, each is based on the following subsystems:

- science payload (sensor head, front- and back-end electronics),
- power supply unit,
- on-board computer,
- housekeeping module and interfacing.

A detailed system overview of the entire CPT-SCOPE instrument, designed for the upcoming BEXUS 20 flight, plus ground segment can be found in Fig. 2.11 and 2.12. The present design of CPT-SCOPE has a mass of $\leq$ 5 kg and dimensions of 26 cm x 31 cm x 40 cm. It should be noted that these parameters do not conform with the CubeSat requirements [13]. However, CPT-SCOPE will serve as demonstrator for key technologies, namely the radiation-hard front-end electronics IC and numerous COTS components. Hence, CPT-SCOPE will serve as important milestone towards CPT-SCOPE 2.0, a true miniature and CubeSat-ready radiation monitor.

In the following paragraph the subsystem will be outlined. A more detailed description will follow in future publications or is available on request.

A.1 Sensor head: The sensor head is composed of a stack of absorbers and silicon detectors, known as particle telescope. By adjusting the absorber material and thickness in the stack, information about the measured particles such as energy and species can be deduced.

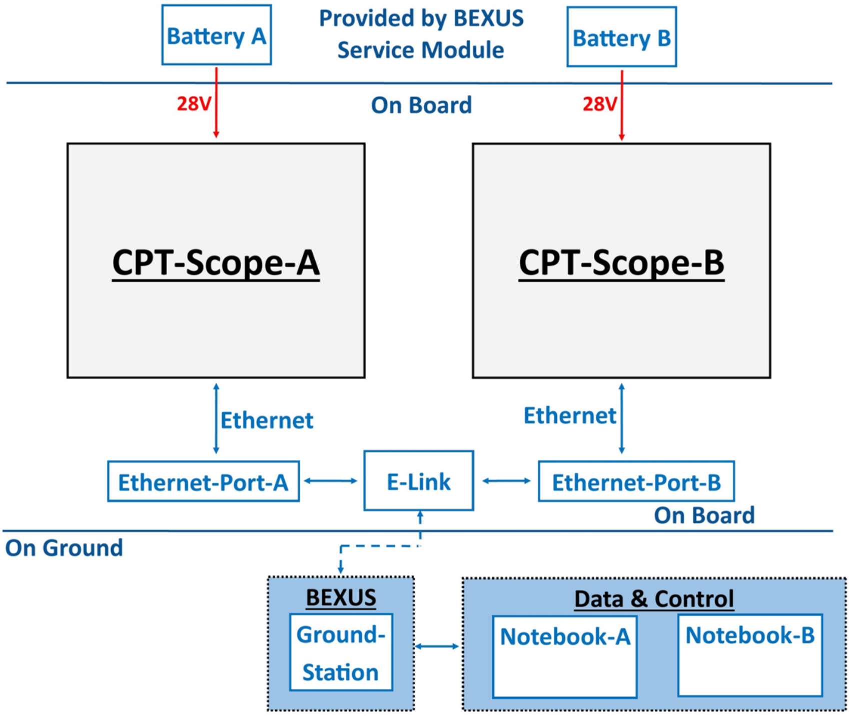

Figure 2.11: CPT-SCOPE system overview showing the entire instrument plus ground segment (bottom) and interfaces to the BEXUS module (top). The system diagram for the individual particle telescopes A/B are shown in Fig. 2.12.

These can be simulated using tools or directly acquired in calibration measurements using particle accelerators or other radiation sources. First Sensor X100-7 and Hamamatsu S3590-09 silicon diodes are used. The diodes are operated at a reverse bias voltage of 30-40 VDC. The current mechanical design can be seen in Fig. 2.10.

A.2 Front-end electronics: At the heart of the front-end electronics lies a radiation-hard *VATA*-family application specific integrated circuit (ASIC) developed by IDEAS. The weak signal pulses are amplified, shaped and digitised using the VATA46x ASIC. The analogue part (VA) of the VATA-ASIC is only in use for calibration purposes. CPT-SCOPE only uses the digital trigger (TA) outputs to optimise the device for high count rates.

A.3 Back-end electronics: The digital signals for each channel serve as inputs for a high-speed trigger pattern counters on a FPGA board. The FPGA device is interfaced with the on-board computer (OBC) using a quasi-SPI protocol. A Numato Mimas board is utilised featuring a Xilinx Spartan-6 FPGA. The OBC stores the raw count rates and corresponding timestamps. In addition it logs housekeeping data. The OBC is also directly connected to the read-out ASIC in order to program it via a serial interface. The OBC is programmed

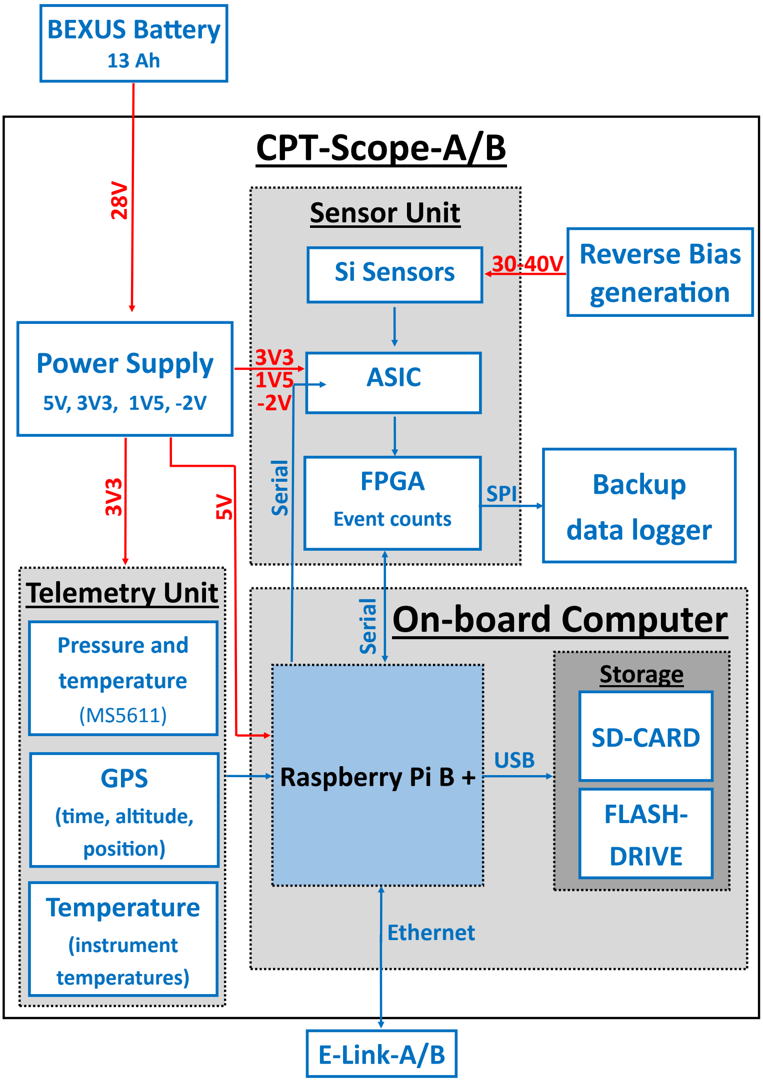

Figure 2.12: The diagram shows the detailed subsystems for each of the two particle telescopes, labelled CPT-SCOPE A/B. The entire CPT-SCOPE system diagram is shown in Fig. 2.11.

to work autonomously. However, it can be accessed via Ethernet, e.g. using the BEXUS E-link system during flight.

B. Power supply unit: The instrument is supplied from the BEXUS service module with +28 VDC. The generation of all relevant voltages, namely +5.0, +3.3, +1.5, -2.0 VDC, are carried out using a combination of switch-mode and low-dropout (LDO) converters.

C. On-board computer: For all on-board operations and communications a Raspberry Pi model B+ will be used. It hosts a powerful system on a chip (SoC) solution which allows to run a Debian-type Linux distribution, while being low-cost. Most of the software is written in Python which allows for simple and rapid development. The OBC communicates with the ground station using both the TCP and UDP protocol for commanding and data streaming, respectively.

D. Housekeeping and interfacing: In addition to science data, a total of 8 temperatures are measured at various points using analogue PT1000-thermistors. For pressure and temperature readings a MS5611 chip is utilised. The Adafruit Ultimate GPS Breakout v.3 is used to obtain GPS tracking, altitude and time during the flight.

All subsystems must be interconnected. The usage of dedicated commercial boards with different standards further complicate this issue. Hence a total of two interface boards had to be designed, for brevity not shown in system overview (Fig. 2.12). These are mounted on top of the OBC and ASIC card, respectively. The instrument is interfaced with the BEXUS service and communication module using two MIL-type RJ45 and two bipolar power connectors.

Mechanical and thermal structure: The instrument with all subsystems is mounted inside an aluminium box with all modules mounted to one of the outer sheets with screws. The whole instrument is then encased by a 35 mm Styrodur insulation layer.

2.4.0.4 Status and Outlook

The development of the sensor prototype are completed. The instrument has been presented at the BEXUS critical design review in late-May 2015. Production and testing should be completed by August 2015. Upon passing all further milestones the flight of CPT-SCOPE aboard the BEXUS 20 balloon is foreseen in October 2015. Post-flight data analysis and instrument calibration should be completed by December 2015 and the final report to ESA issued in January 2016.

The instrument approach of utilising low-cost commercial components and re-use of radiation-hard key components may allow the CubeSat and small satellite community to further miniaturise their (radiation) payloads, while keeping the cost at bay. So far two CubeSat missions have shown interest in hosting a future CPT-SCOPE 2.0 device, one of them being the proposed French-Taiwanese BIRDY mission [51]. The CPT-SCOPE team is interested in adapting the instrument towards other future missions and applications.

Chapter 3

Device Construction and Implementation

This section reflects the major part of the thesis work - the development and implementation of the radiation monitor technology demonstrator. It will outline the requirements and specifications, and their implementation in hard- and software. The paragraphs will extend over a wide range of disciplines, from physics over electronics to mechanical and software engineering. The reader is provided with brief introductions to each section but is referred to more specialised literature for a better in depth understanding of the various aspects involved.

The successful implementation of the device is the main goal of this work. Later measurements of physical samples will only serve as test and verification. Nevertheless, these are also relevant and help characterise the instrument.

3.1 Requirements and Specifications

In this work a radiation monitor capable of measuring energetic charged particles and low-energetic gamma rays is implemented. COTS silicon sensors shall be used. The device shall rely on COTS components whenever possible. At the heart of the device an IDEAS VATA465 ASIC shall be used as detector front-end. All components need to be interfaced and work properly together. The specific goals have also been outlined in chapter 1.

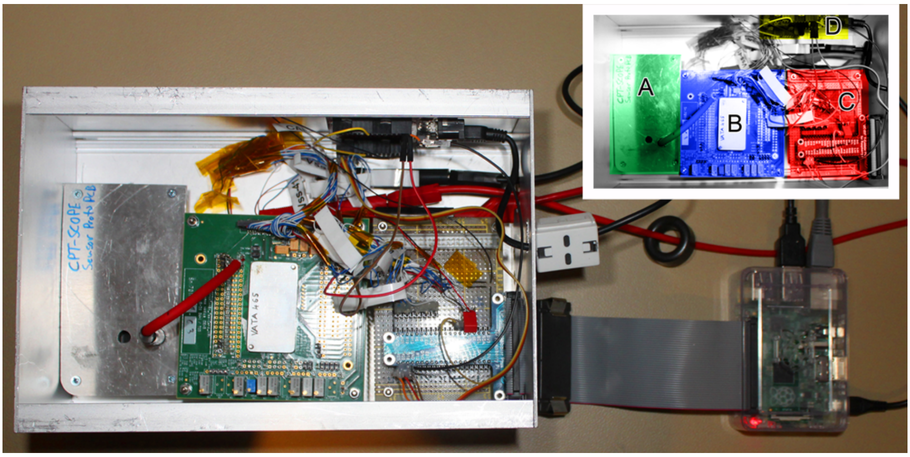

Figure 3.1: Photo of the main system components. The inset shows the individual modules which are labelled by capital letter A-D. These will be described in the text.

3.2 Implementation

The following sections will describe the system overview and its implementation in hard- and software.

3.2.1 System Overview

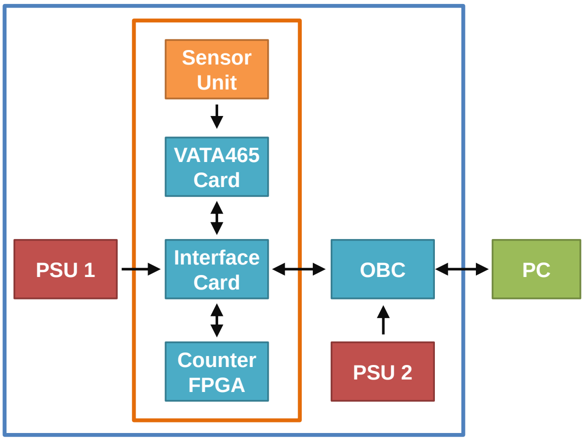

Figure 3.2: System overview.

A simplified system overview is shown in Fig. 3.2 while Fig. 3.1 is a picture of the actual main setup. The shown components are: the sensor unit (A), the VATA465 card (B), the interface card (C) and the counter FPGA (D). Located outside, to the right hand side is the on-board computer (OBC). The power supplies are not shown in the picture. All sensitive parts are located inside an aluminium box where they are mounted by screws to the surfaces. This reflects the physical implemented instrument with its modules.

3.2.2 Hardware

The following sections will describe the used hardware and components, its purpose, characteristics and electrical connections. All self-developed electronics was designed using the CadSoft EAGLE PCB Design Software, short EAGLE, version 7.2.0[1].

3.2.2.1 On-board computer

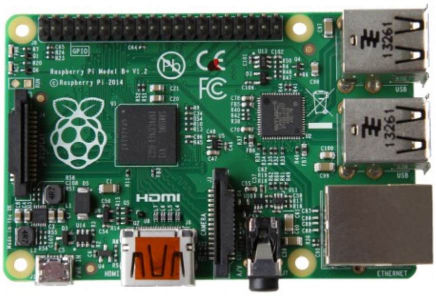

Figure 3.3: Raspberry Pi B+ board as seen from above (credit: Raspberry Pi Foundation).

Purpose: The on-board computer (OBC) controls the instrument, provides remote access and stores the data locally. It is part of the detector back-end.

Description: For data processing, storage and network access a Raspberry Pi B+ has been used. This system on a chip (SoC) device uses a single core Broadcom BCM2835 with 700 MHz and 512 MB of RAM. The processor architecture is ARM-6-based. It has four USB-ports, one Ethernet port and one combined video/stereo out jack. Furthermore, it allows for connecting a display and camera module using flat-band cables. Additionally, 40 general purpose input and output (GPIO) pins are available on two parallel pin banks which can be controlled or sensed via software. The pin spacing is 0.1 inch (100 mil). These can easily be accessed via a standard 40 pin Parallel ATA (PATA) cable and connected to a breakout board. The display output can be either accessed via a mini-HDMI output, composite video or flat-band cable connector. The device can boot from a Secure Digital (SD) card, type micro-SD, which can be inserted into a dedicated slot.

The dimensions of the Raspberry Pi B+ are 85 mm x 56 mm x 17 mm[2] and a total weight of 42 g. The size is comparable to a conventional credit card. The power consumption is well below 2 W with typical values of 1.3 W[3]. It requires a 5.0VDC input via a micro-USB adapter, conventionally found in modern mobile phone chargers. The on-board power supply unit (PSU) hosts filtered switch-mode voltage converters with high-efficiency. These

---

[1] EAGLE web page: `http://www.cadsoftusa.com/`.

[2] `https://www.raspberrypi.org/documentation/hardware/raspberrypi/mechanical/Raspberry-Pi-B-Plus-V1.2-Mechanical-Drawing.pdf`

[3] `http://raspi.tv/2014/how-much-less-power-does-the-raspberry-pi-b-use-than-the-old-model-b`

produce the required 3.3VDC and 1.8VDC for the Raspberry Pi B+ from the 5.0VDC input.

The unit cost is approximately 30 Euro (June 2015). The above features, small size and low-cost make the Raspberry Pi B+ an ideal development platform for this project.

3.2.2.2 Counter - FPGA

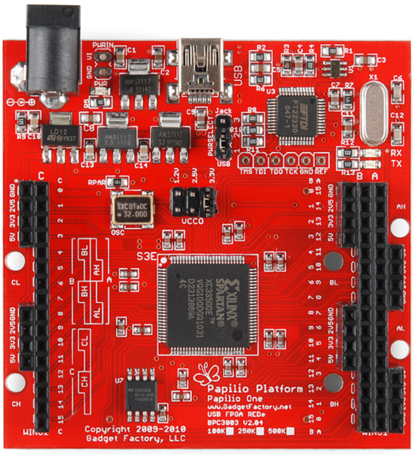

Figure 3.4: Papilio One 500K board as seen from on top. Featuring the FPGA (centre), and GPIO banks (left and right). (credit: Gadget Factory)

Purpose: The counter FPGA registers the triggers provided by the VATA465 card as part of the back-end electronics. It further implements a quasi-SPI slave to transmit the individual counter values to the OBC.

Description: In order to be able to achieve high count rates, and avoiding non-deterministic delays due to hardware running a non-real-time operating system, advantage has been taken by using a Field-Programmable Gate Array (FPGA). Such device allows to reconfigure several hundred thousand logic units at start-up in order to carry out tasks requiring speed and parallelism.

For this project a Papilio One 500K FPGA board (see Fig. 3.4) has been used which has been developed by Gadget Factory [23]. It features a Xilinx Spartan-3E FPGA (model: XC3S500E) which has 500,000 system gates which is approximately equivalent to 10,476 logic cells [65].

The board provides 48 GPIO lines, four power rails at 5.0VDC, 3.3VDC, 2.5VDC and 1.2VDC using low-dropout (LDO) linear regulators, on-board 4Mbit SPI flash memory and a FT2232D IC for serial communication and programming. The clock source is a 32 MHz oscillator.

The unit can be powered through a micro-USB adaptor (5.0VDC input) or via a 3.5 mm DC jack. In this case the FPGA is powered using an USB cable from the OBC. It can also be reconfigured via the USB port.

The 48 GPIO pins are available on three rows located on either side of the FPGA as shown in Fig. 3.4. The left-hand single row contains pins C1-C16 while the right-hand double row hosts pins A1-A16 and B1-B16. Additional ground (GND) and voltage rails are accessible as individual six 4-pin headers on either side of aforementioned rows. The pin spacing is 0.1 inch (100 mil). The GPIO pins can use different logic voltages. However, in this case a standard 3.3VDC logic levels are used (cf. 3.3VDC CMOS logic). The used FPGA pins and their functional names are provided in Tab. 3.1. All pins use 3.3VDC (LVCMOS33) besides the global clock (CLK) which uses the LVCMOS25 i.e. 2.5VDC logic levels. The board dimensions are 2.7 inch x 2.7 inch x 0.45 inch (68.6 mm x 68.6 mm x 12 mm) and weights 32 g. The unit cost is 65 USD (ca. 60 Euro, June 2015).

Table 3.1: Used FPGA pins labelled with the board GPIO name, Spartan-3E pin and its functional name.

Signal	FPGA Board GPIO	Spartan-3E Pin	Direction
CLK	N/A	P89	in
RST	A6	P53	in
TRG_IN_0	C0	P91	in
TRG_IN_1	C1	P92	in
FPGA_SCLK	A0	P18	in
FPGA_CS	A1	P23	in
FPGA_MOSI	A2	P26	in
FPGA_MISO	A3	P33	out

3.2.2.3 VATA465 ASIC Card

This section is an expanded version from the author's previous specialisation report, see [54].

Purpose: The VATA465 ASIC card hosts the necessary front-end electronics for the instruments. The PCB provides the IC with all necessary electronics and connects it to all other modules.

Description: The IDEAS ASIC model VATA465 is mounted on a custom-made evaluation card which has been developed for its predecessor model, the VATA464. Therefore minor modifications of the card, a printed circuit board (PCB), and its electrical connections were necessary (not shown, located on PCB back-side). The ASIC is mounted in the centre of the PCB and is protected by an aluminium casing. The housing has been electrochemically treated by the Alodine process which prevents the formation of a non-conductive oxide layer. The case is connected to common ground and protects the ASIC from external interference such as light and other electromagnetic radiation as well as mechanical stress.

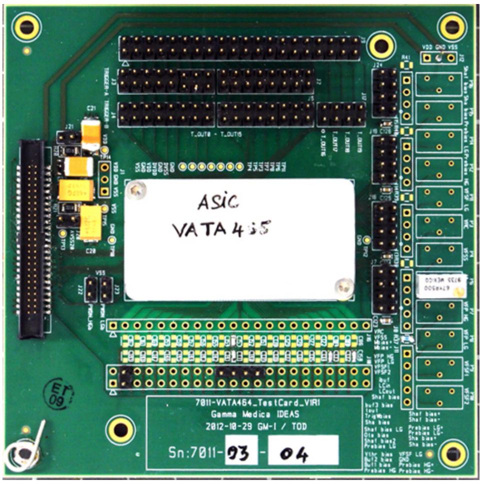

Figure 3.5: VATA465 evaluation card. (credit: IDEAS)

The ASIC is wire-bonded using thin 300 μm Al wires to establish electrical contact with the PCB and is glued to the test card using conductive epoxy. These are shown in Fig. 3.6.

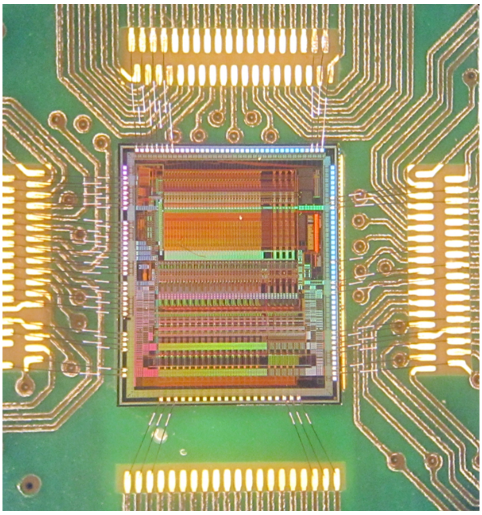

Figure 3.6: Wire-bonded VATA465 ASIC on evaluation card. The image was taken through a microscope and shows the connected input pads (bottom), trigger outputs (top) and configuration / power pads (left and right).

The card's hardware features will now be described in reference to Fig. 3.5:

- **Configuration register / PSU adaptor:** On the left is a 50 pin cable adaptor. It directly connects to the interface board providing i) the two required analogue voltages V_{SS}=-2.00VDC and V_{DD}=1.5VDC from the external power supply unit (PSU) number 1 (cf. Fig. 3.2), ii) the serial interface for programming and readout of the ASIC configuration register. Although not used, it also features a calibration input, the analogue multiplexer outputs and access to its control shift register.

- **Power line filtering:** The four SMD capacitors (yellow rectangle) located next to the aforementioned adaptor serve as power line filters to remove noise and spikes.
- **Bias generation:** The potentiometer located on the far right, lower centre provides a fixed current to the ASIC which is used for its internal bias generation network. Several biases can be setup, however, in our setup only one, the minimum number necessary, was used for simplicity. On some VATA465 cards multiple potentiometers may be installed. However, unless otherwise stated only the main MBIAS is generated.
- **Signal inputs:** On the bottom 20 input pads are provided. These are accessible via by several pin banks and also allow for AC-coupling via SMD capacitors. In our setup the signal is directly connected to the ASIC input pad (top-most row). These pins are in particular sensitive to ESD and require caution when handled.

  In the framework of this work only one channel input is used, namely input IN_01. The grounding and connection will be explained in the detector unit description below.
- **Trigger outputs:** The top rows represent several access points for the 36 trigger outputs. We use the top-most two row bank to access the individual digital triggers. The triggers are set to 3.3VDC logic levels.
- **Mounting holes:** The card features six mounting holes accepting M3 screws. These are located on each corner and two placed within the outer perimeter of the PCB. Their surrounding pads are connected to ground.

The card dimensions are 10 cm x 10 cm x 1 cm and weights less than 100 g. It is especially developed for the VATA46x-family ASIC and is hence not a COTS component.

The card is designed to operate with the IDEAS VATA ASIC test setup which uses expensive components to control and readout data. These are described in the specialisation project report [54] and the VATA465 validation report [46].

Since the approach of this thesis is in using COTS components, an interface card had to be made which will be described below.

3.2.2.4 Interface Card

Purpose: All relevant instrument modules are connected with each other via the interface card.

Description: The interface card serves as interconnect for the VATA465 card, the counter FPGA board and the OBC. It also provides power to the ASIC card. The card is labelled (C) in Fig. 3.1.

Table 3.2: OBC GPIO pin assignment for the FPGA quasi-SPI interface with the OBC and the ASIC serial shift register control.

Signal	OBC GPIO
FPGA_CS	21
FPGA_MOSI	20
FPGA_MISO	16
FPGA_SCLK	27
ASIC_LOAD	26
ASIC_REGIN	19
ASIC_SCLK	13
ASIC_REGOUT	6
ASIC_READBACK	5

The schematic is shown in Fig. 3.7. The schematic is divided into five sections:

A: The quasi-SPI interface providing communication between the counter FPGA and the OBC. The four relevant ports, labelled *FPGA_X*, are directly connected to the 40-pin OBC connector as indicated in Tab. 3.2. 3.3VDC logic levels are used. The connection is realised by placing prototyping wires between the interface card and FPGA board pins (cf. Tab. 3.1). All pins but *FPGA_MISO* are outputs going towards the FPGA.

B: A three pin header is provided to connect the 3.3VDC supply cable for the ASIC logic outputs (trigger/serial shift registers). A $2.2\mu F$ WIMA MKS2 capacitor (C1, [62]) has been placed between the 3.3VDC rail and ground (GND) in order to reduce noise. All pins are ”outputs” as they provide the 3.3VDC rail to the ASIC.

C: The 40-pin connector of the OBC (Raspberry Pi) is connected i) to the FPGA SPI interface (A, direction: in/out), ii) the ASIC 50-pin connector (E, direction: in/out) and provides the 3.3VDC rail for the ASIC (B, direction: out). The relevant GPIO labels are given in Tab. 3.2.

D: Ground (GND), as well as ASIC analogue voltages V_{SS} and V_{DD} are provided by an external laboratory power supply. A three pin connector is used to symbolise this. The respective voltage rails are routed through the interface card to the 50-pin ASIC connector (E).

E: A special 50-pin connector allows access to the VATA465 ASIC, connecting the ASIC’s serial configuration register (*ASIC_x*), ground and analogue voltages V_{SS} and V_{DD}.

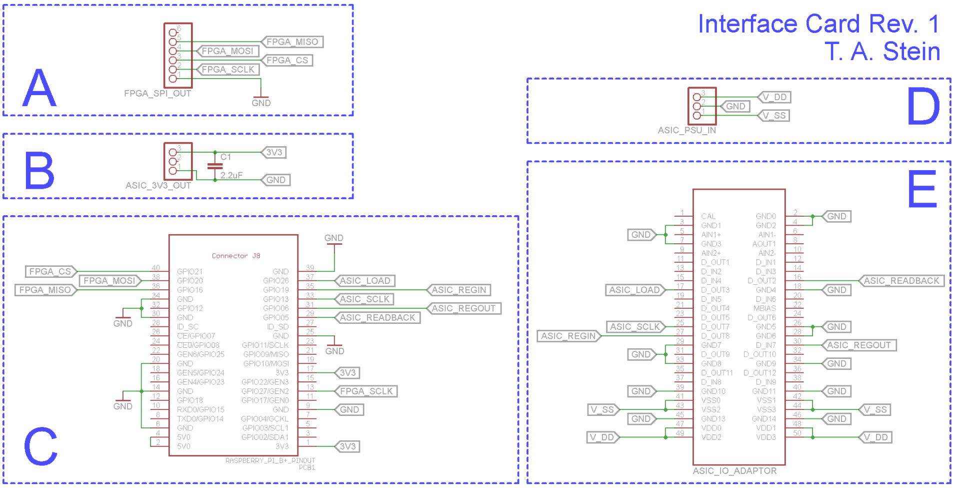

Figure 3.7: Interface card schematic showing the following sections: (A) FPGA SPI, (B) ASIC trigger voltage supply, (C) the OBC 40-pin connector, (D) ASIC analogue power supply (input) and (E) the ASIC 50-pin adaptor.

The interface card itself was made using a fibre-glass perfboard for through hole components and 100 mil pin pitch. All components are passive and were hand-soldered. The only necessary placement restriction was to keep distance between digital lines to the ASIC analogue voltage rails.

The OBC was interfaced (C) using a third-party breakout board similar to the Adafruit *Pi T-Cobbler Plus Kit*[4]. It allows to connect the breakout board with a 40-pin PATA flat-band cable to the Raspberry Pi B+ GPIO header. In order to allow for a flexible setup two 40 pin headers were soldered parallel to each other. This allowed to provide for each 20-pin row a second row into which prototyping wire or probes can be connected to in order to verify the pin function or establish electrical contact. This has been used to connect the FPGA-OBC quasi-SPI interface (A, C).

In order to suppress external noise a ferrite choke was placed around the flat-band cable and all other cable entering the instrument box (cf. Fig. 3.1).

The ASIC's 3.3VDC rail is provided by a three pin header into which a small cable from the VATA465 card can be inserted.

The external analogue voltages and ground (D) were connected by using standard insulated copper wires which were fixed and soldered to regular banana plug. This allows for a simple and robust connection to the external power supply (PSU 1).

The 50-pin ASIC connector is emulated by soldering all relevant cables from a female connector cable to the perfboard.

The above described approach may appear as too simple. However, it allows for rapid prototyping and putting focus on more important aspects of the project. Since all cards

---

[4] Raspi 40-pin T-cobbler kit by Adafruit: `http://www.adafruit.com/products/1989`

of the system are fixed to the instrument box and due to the exceptional mechanical stability of the interface card no attempts were made to turn the card design into a custom PCB.

The interface card has approximate dimensions of 11 cm x 8 cm x 2.5 cm and weights less than 100 g (including the breakout board). It is mounted to the instrument box using four M3 screws.

Later on, within the CPT-SCOPE project, the above interface card has served as basis for an improved card with added functionality such as temperature and pressure sensors. Based on the presented interface board a new custom PCB was designed and produced by the CPT-SCOPE team with involvement of the thesis author.

3.2.2.5 Detector Unit

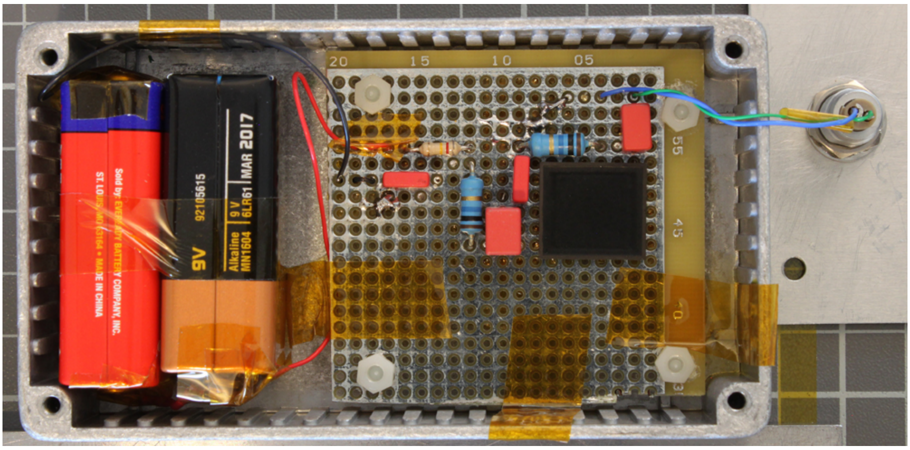

Figure 3.8: Sensor card board photo showing batteries (left), main sensor card (middle), connector (right) and housing.

3.2.2.5.1 Overall setup

Purpose: The detector unit is the heart of the radiation monitor. It measures the incident subatomic particles and provides their respective signal current pulses to the front-end electronics.

Description: The detector unit is located inside an aluminium box in order to shield it from external interference. It hosts a detector board, the batteries required for the reverse-bias generation and a signal interface towards the VATA465 card.

First the main electrical schematic and its function will be explained followed by a paragraph about the cabling with other instrument modules, grounding scheme and the First Sensor X100-7 silicon diode.

The function of the detector board is to:

- i) detect the incident particle and gamma radiation using a silicon diode,
- ii) generate a depleted zone within the diode via reverse biasing. This layer is sensitive for radiation.
- iii) filter the reverse-biasing voltage for noise-suppression and stability.
- iv) transmit the weak AC-coupled current pulses to the ASIC via a shielded twisted pair cable.

Schematic and parts: In order to fulfil those tasks three sections are located on the detector unit as shown in the electrical schematic in Fig. 3.9:

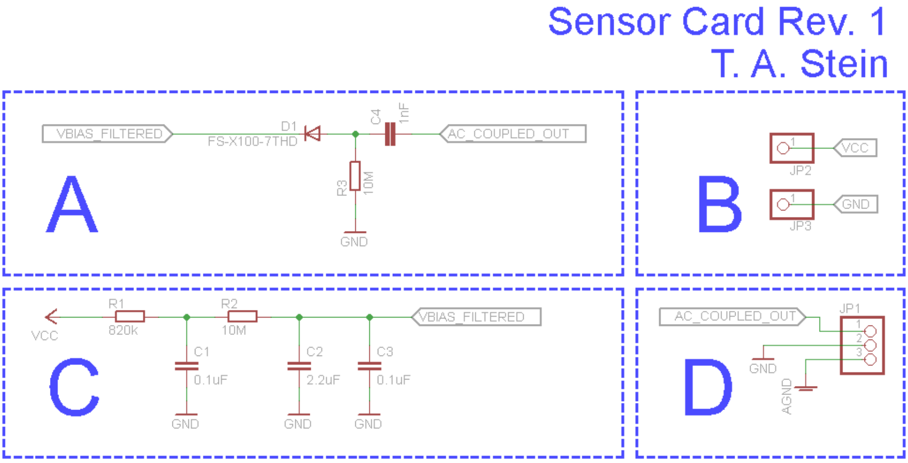

Figure 3.9: Sensor card schematic, rev. 1: (A), (B), (C), (D).

- silicon sensor diode and signal coupling (A),
- reverse-bias generation and filtering (B, C),
- signal interfacing (D).

We will now describe the design and parts choice more thoroughly:

Batteries: The following batteries were used:

- A standard 9VDC (model: Duracell MN1604, technology: Alkaline-Manganese Dioxide, [21]).
- A 22.5VDC electronics application battery (model: Eveready 412, technology: Zinc-Manganese Dioxide, [22]).

These have been placed in series to provide the necessary reverse-bias voltage V_{Bias} (nominal: 31.5VDC, measured: 33.7VDC). It should be noted that the batteries are not shown in the schematic but are clearly visible in Fig. 3.8 (left). In the schematic the positive battery pole is represented by *VCC* while the negative terminal is connected to *GND*. Batteries have been chosen due to their superior noise performance over voltage regulators etc. For several battery technologies this has been verified by measurement [10]. Due to the correlation of the in-coming and out-going charges shot noise (current) is suppressed and Johnson noise (voltage, temperature) dominates [10]. It should be noted that the battery ground (GND) is not connected with the chassis ground (AGND) and is hence floating. This is done to prevent any external noise pickup (cf. [36]).

B - Battery connection: The batteries are soldered directly to the sensor card via two insulated wires. In the schematic this is represented by two connector pins for rails *VCC* and *GND*.

C - Reverse-bias filtering: The provided voltage on *VCC* may still be noisy due to external pickup or other transient voltage spike sources. In order to eliminate any high-frequency noise sources a second order low-pass RC-filter is implemented in section C [61].

With the given resistor and capacitor values (cf. Tab. 3.3) a centre frequency[5] of $f_c = 0.1$ Hz is achieved. This was verified with an on-line tool by OKAWA Electirc Design [18] and the MATLAB Control System toolbox (not shown).

While the slope of the second order low-pass filter is increased (-40dB/decade) its cut-off frequency[6] is slightly shifted to $f_{(-3\mathrm{dB})}$ = 0.08 Hz [61]. Due to the long time constant of approx. 12.5 s, the detector should only be used for readout ca. 60 s time after connecting it to the batteries.

High-quality WIMA MKS2 capacitors were used which are based on metallised polyester foil (PET) technology. These are used in bypassing or timing applications [62].

The filtered bias voltage is denoted *VBIAS_FILTERED* and is supplied to the detector diode in section A.

A - Sensor diode and signal coupling: The First sensor X100-7 Si diode [1] is used to detect the incident particle and gamma radiation. It is placed in reverse-bias mode such that it blocks current passing through unless an ionising particle creates electron-hole pairs which in turn are responsible for a signal current pulse. In order to restrict the bias current a 10MΩ bias resistor (R3) is placed to GND. The chosen bias resistor value represents a compromise between: i) low-noise requirement (large R_{Bias}), ii) the induced voltage drop ($R_1 + R_2$ vs. R_3) at high count rates[7] and iii) available parts.

The signal current is AC-coupled via a high-quality WIMA 1000 pF FKP2 foil capacitor (C4). The Polypropylene (PP) foil technology based capacitor has very low losses and is hence optimal for the use in low-noise scientific instrumentation or

---

[5] Centre frequency calculation (adapted from [61]): $f_c = \frac{1}{2\pi\sqrt{R_1 \cdot C_1 \cdot R_2 \cdot (C_2 + C_3)}} = 0.1$ Hz.

[6] Cut-off frequency calculation [61]: $f_{(-3\mathrm{dB})} = f_c \cdot \sqrt{2^{(1/n)} - 1} = f_c \cdot \sqrt{2^{(1/2)} - 1} = 0.08$ Hz, $n = 2$.

[7] personal communications D. Meier, Mar. 2015.

audio applications [52, 63]. It is important to use a large coupling ($C_{coupl.}$) compared to the detector capacitance $C_{coupl.} \ll C_{diode}$. This insures maximum charge transfer to the preamplifier input [52]. The detector capacitance at 30VDC reverse-biasing is approx. $C_{diode} \approx 50$ pF [1]. In fact, the current setup has a high charge transfer rate of 95.2% (cf. Eq. (2.102) in [52]).

The AC-coupling of the signal (*AC_COUPLED_OUT*) may decrease the detector performance marginally [52] but makes the device independent of the diode's dark current.

D - Signal interfacing: The weak current pulse generated in the Si diode by energetic particles is AC-coupled to a twisted wire cable pair. The green and blue wire are connected to the signal rail (*AC_COUPLED_OUT*) and ground (*GND*), respectively as shown in Fig. 3.8. The entire sensor unit is not electrically connected to the housing (*AGND*) in order to prevent noise pickup. This symbolised by the three pin header in schematic section D.

The twisted pair cable is connected to a female LEMO K connector with 2 contacts [38]. The box ground (AGND) is connected to the external cable shield.

Table 3.3: Sensor board parts overview, all through-hole.

Item	Type	Component	Section	Comment
D1	diode	First Sensor X100-7 THD	A	radiation detector
R1	resistor	820kΩ, 5%	C	low-pass filter
R2	resistor	10MΩ, 5%	C	low-pass filter
R3	resistor	10MΩ, 5%	A	bias resistor
C1	capacitor	WIMA MKS2 0.1 uF - 63VDC	C	low-pass filter
C2	capacitor	WIMA MKS2 2.2 uF - 50VDC	C	low-pass filter
C3	capacitor	WIMA MKS2 0.1 uF - 63VDC	C	low-pass filter
C4	capacitor	WIMA FKP2 1000 pF - 100VDC	A	AC-coupling

Board and part placement: All components are mounted on a regular fibreglass-reinforced epoxy perfboard (FR-4) with 100 mil pad spacing for through hole parts. These were hand soldered. Electrical connection was established using regular tinned copper wire. The top layer acts as ground plane, while the bottom layer is divided into individual pads which are all tinned.

The sensor board schematic is shown in Fig. 3.10 while the actual detector unit photo is presented in Fig. 3.8.

The placement of parts is relevant to reduce noise and increase the detector efficiency. Care has been taken to separate the bias filtering section (left) from the diode and signal coupling (right). The ground current return paths are indicated by orange arrows in Fig. 3.10. The distance from the bypass capacitor and R_3 ground terminals to the battery ground had to be made as short as practically possible while being away from the Si diode and the AC-coupling capacitor. This allows interference currents to return to ground without being injected into the signal path.

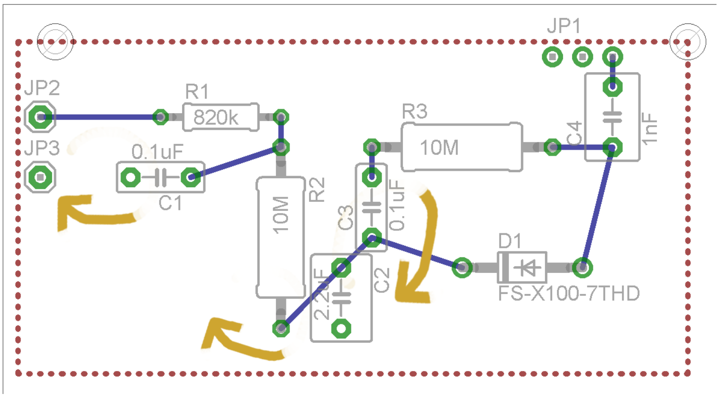

Figure 3.10: Sensor card board sketch without batteries and signal connector. The bottom layer connections are marked blue, pads in green and the top layer ground plane is indicated by its red outline. The orange arrows indicate current return paths to ground, see text.

The distances between the AC-coupling capacitor and the diode had to be small. The signal cables were twisted in order to prevent pickup. This is achieved by the compensating current flows in both cables [52].

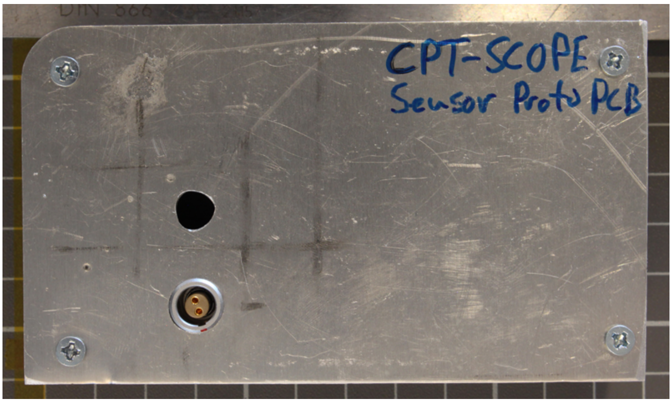

Figure 3.11: Detector unit, top view (photo).

Housing - mechanical and electrical aspects: The detector unit is housed in a 2 mm thick, conductive Al casing which has on the top surface in each corner a M3 size screw hole [34]. Its dimensions are approx. 12 cm x 7 cm x 4 cm (L x W x H).

All components are placed inside the box and fixed with non-conductive Kapton (polyamide) tape[8]. The sensor board is elevated from the box bottom by M3 spacers made of non-conductive Teflon. Other relevant sections are prevented from electrical contact with the

---

[8] Kapton information sheet: `http://www.dupont.com/content/dam/assets/products-and-services/membranes-films/assets/DEC-Kapton-summary-of-properties.pdf`

surrounding by taping Kapton over them.

A 1 mm conductive Al sheet is used as top plate as shown in Fig. 3.11. In the picture is is labelled as "Sensor Proto PCB". Four M3 screws hold the top plate in place. At the location of the Si diode a hole with approx. 7 mm diameter has been drilled to allow incident particles and low-energetic gamma rays to pass through. The signal interface adaptor is shown below the sensor entrance hole.

The grounding scheme will be discussed below. However, first the signal interfacing will be described.

3.2.2.5.2 Cable connector to VATA465 card

An important role plays the connection between the detector and the front-end electronics.

Figure 3.12: Shielded twisted pair cable by Van Damme (photo credit: Van Damme, adapted from [17]).

Here several aspects must be kept in mind:

- keeping the cable length and hence parasitic capacitance at a minimum,
- external noise has to be shielded from the signal wires,
- the resistance of the cable has to be kept at a minimum to reduce losses.

While these electrical characteristics have to be fulfilled also mechanical stability has to be provided.

Usually, the detector anode or cathode are directly wire-bonded to the front-end ASIC's input pads[9] e.g. when using DC-coupling [52]. Typical distances are in the range of a few millimetres. In such cases the front-end electronics and detector are in the same metal casing shielding it from external interferences. This mode of operation will not be possible in CPT-SCOPE and hence the technology demonstrator of this thesis has to test an external

Table 3.4: Selected Van Damme Pro Grade Classic XKE pro-patch characteristics from [17].

Characteristic	**Value**	**Unit**
Capacitance (core to core)	50	pF / m
Capacitance (core to screen)	95	pF / m
Resistance (conductor, screen)	< 85	Ω / km
Overall diameter	4.85	mm
Weight	39	g / m

---

[9] personal correspondence with G. Mæhlum, Feb. 2015.

cable connection between the detector and VAT465 ASIC board. In the present case a high-quality audio cable has been used. The Van Damme Pro Grade Classic XKE pro-patch is a shielded twisted pair cable providing excellent electrical and mechanical characteristics. A photo of a white Van Damme cable is shown in Fig. 3.12: the two inner conductors (red, green), braided shielding and outer synthetic material jacket. The key characteristics are listed in Tab. 3.4.

The used cable is the red type (Van Damme article number: 268-009-020) with an approx. length of $L = 15$ cm. The resulting parasitic capacitance is 7.5 pF. This adds to the detector capacitance (both are in parallel) resulting in minimally reduced total charge transfer efficiency of 94.5% (calculated using [52]). The expected cable resistance is less than 0.02 Ω, which is negligible.

The cable is on the detector unit connected to a male LEMCO K connector [38] and on the VATA465 card side directly soldered to an ASIC input pad, namely to channel IN_01, as shown in Fig. 3.1.

Previous trials with simple coaxial cables and BNC adaptors have been unsuccessful as the noise level increased significantly, not allowing the detection of ionising radiation (data not shown). Hence, the utilisation of a shielded twisted pair cable was important and improved the detector performance significantly.

3.2.2.5.3 Grounding Scheme and Noise Reduction for Analogue Electronics

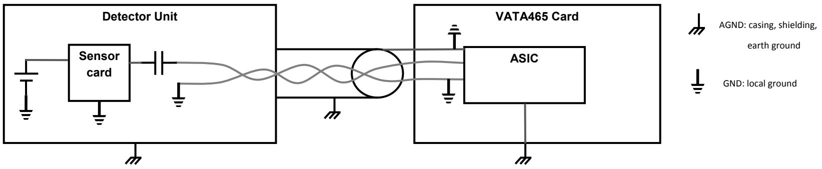

Figure 3.13: Grounding scheme for sensitive analogue part of the instrument.

Great care has been taken to reduce possible noise pickup by the sensitive analogue detector and front-end electronics. This has been outlined in previous sections above. However, the grounding scheme deserves an overview with a few remarks. The scheme is shown in Fig. 3.13 which displays the detector unit (left) and VATA465 card (right).

The casing ground (AGND) of the detector unit is electrically only connected to the twisted pair cable's outer shield via the LEMO K connector. The metal case serves as quasi-Faraday cage to prevent external interference to be injected into the sensitive sensor electronics. For this reason also the batteries are located inside the box. The negative battery terminal is connected to the sensor card's local ground (GND). Its battery and main ground (GND) are floating in respect to the housing. The sensor board has a ground plane and the components have been carefully placed to allow for optimal ground current return paths via bypass capacitors (cf. schematic section). Electrically the sensor board is only AC-coupled to other components.

The cable's signal ground (GND) and detector box ground (AGND, case) are connected on a common ground pin (GND) close to the ASIC as shown in the figure. The VATA465 card has a ground plane which is connected to both the local ground (GND) and case ground (AGND). These practises reduces noise pickup[10] [52].

In future iterations the cable shield may not be connected to the case ground on the detector unit. This is under discussion for CPT-SCOPE.

3.2.2.5.4 The Si-Sensor Diode

The First Sensor (FS) silicon PIN-diode[11], model X100-7 THD (#501400), is an application-specific semiconductor device to detect ionising radiation (data sheet: [1]). It provides 100 mm^2 (10 mm x 10 mm) of active surface. The diode is in a ceramic package (thickness ca. 0.4 mm) which is filled with a black epoxy. This protects the silicon diode from mechanical stress, dust and visible light.

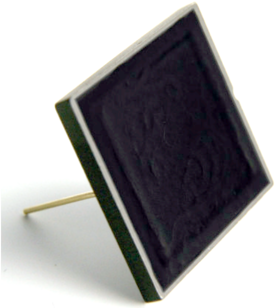

Figure 3.14: Picture of the First Sensor X100-7 Si diode (credit: First Sensor AG, [1]).

Two pins are available to connect to the anode (notch side) and cathode respectively. The diode has a good performance at low-cost (ca. 40 Euro per unit, Mar. 2015). Its dark current (left) and capacitance (right) characteristics are shown as function of reverse-biasing voltage V_{Bias} in Fig. 3.15. Since it is readily available and relatively inexpensive it is a COTS component.

At a temperature of 23°C and $V_{Bias} = 30$ VDC a typical FS X100-7 diode has a dark current of $I_D = 5$ nA and capacitance of $C_{diode} \approx 50$ pF. Depending on the device the dark current may vary at $V_{Bias} = 30$ VDC from 1 nA to 10 nA. These values were confirmed by measurements of the above setup (not shown). The recommended maximum reverse bias voltage is $V_{Bias}^{(\max)} = 50$ VDC. It should be noted that the diode is never fully depleted

---

[10] personal communication with G. Mæhlum, March 2015.

[11] This type of diode has an intrinsic Si layer sandwiched in between a highly doped n- and p-Si-layer which are electrically contacted. This device differs from the classical PN-diode but has in many cases superior properties for ionising radiation measurements due to its thick depleted zone and better electrical performance [36].

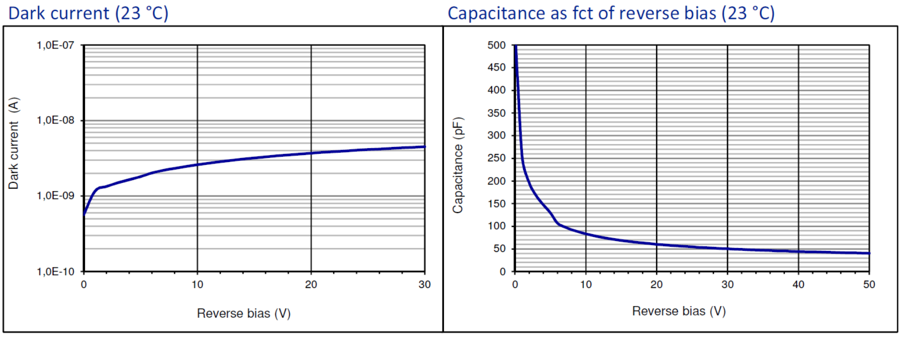

Figure 3.15: Dark current (left) and capacitance (right) characteristics as function of the reverse-bias voltage V_{Bias} of the First Sensor X100-7 diode. The data was taken at a temperature of 23°C for a typical device. The individual diodes may vary (credit: First Sensor AG, [1]).

within the qualified bias range. The following depletion thicknesses for a typical X100-7 diode were provided by First Sensor and are shown in Tab. 3.5. In the framework of this master thesis the diode will be operated at a reverse bias voltage of some 33 VDC which correspondents to a depletion thickness of at least $d = 255\ \mu m$. This value is close to standard silicon radiation detectors with approx. 300 μm depletion thickness [52].

Table 3.5: Typical depletion thickness d of a FS X100-7 PIN diode as function of V_{Bias} (source: First Sensor, personal communications - Feb. 2015).

V_{Bias} / V	d / μm
5.0	100
9.5	150
17.0	200
28.5	250
30.0	255

The depletion thickness can also be derived from the measured capacitance and active surface size. This is well reflected in the capacitance curve Fig. 3.15 (right) and Tab. 3.5: as the separation of the anode and cathode (d) decreases the diode capacitance C_{diode} increases in accordance to the classical plate capacitor with constant surface A.

Due to the low atomic number of silicon ($Z = 14$) and the small absorber thickness the X100-7, like most other Si radiation detectors, is only sensitive to low-energetic gamma rays. The absorption probability of a gamma ray in the active layer of the X100-7 diode as function of E_γ is shown in Fig. 3.16. There are three energy regimes:

- $E_\gamma < 1.5$ keV: the gamma ray is already absorbed in the epoxy layer and is not detected. The detection probability drops quickly below 1%.
- 1.5 keV $< E_\gamma <$ 300 keV: In this energy range most gamma rays reach the sensitive layer. A detection is only higher than 10% for the energy range between 2 keV and

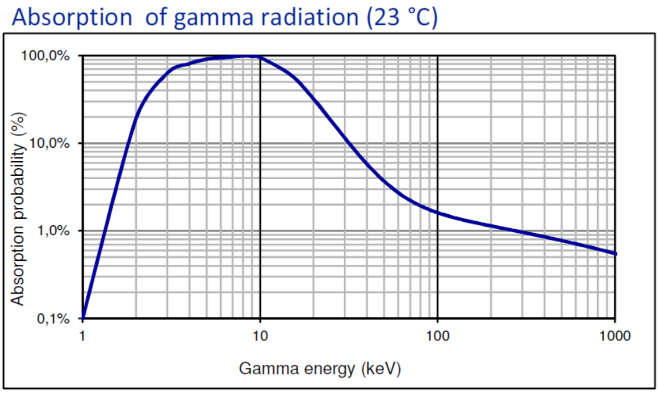

Figure 3.16: Gamma photon absorption probability of a First Sensor X100-7 diode as function of its energy E_γ (credit: First Sensor AG, [1]).

30 keV, the detection probability peaks with over 80% for 4 keV and 10 keV.

- $E_\gamma > 300$ keV: The mean free path λ of the gamma ray is significantly larger than the depletion layer thickness. An absorption is no longer likely and the probability of detection sinks steadily below 1%.

For all gamma rays with $E_\gamma < 100$ keV the dominant interaction process in silicon is photoelectric absorption [52].

The FS X100-7 has been chosen due to its low-cost and large active surface area of 100 mm^2. The large active area is necessary in order to maximise the possible count rate of the CPT-SCOPE instrument.

First Sensor also provided a smaller (10 mm^2) PIN diode for radiation detection with superior noise performance, full depletion with ca. $d = 300\ \mu m$ and a guard ring to reduce dark current significantly. The FS X10-γ diode will serve as candidate for a planned CubeSat-ready radiation monitor device following the CPT-SCOPE development and flight in October 2015.

3.2.2.6 Power Supplies and Distribution

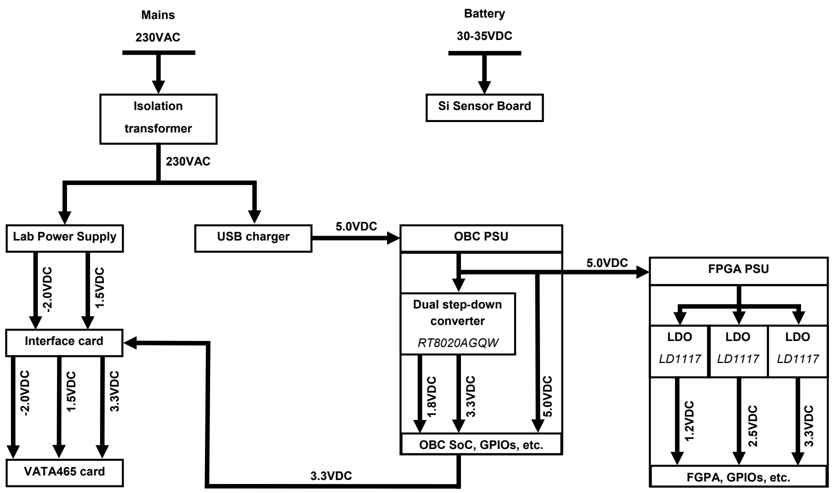

Figure 3.17: Instrument power distribution, showing all modules and relevant voltage rails.

The power supply and distribution overview are shown in Fig. 3.17. There are two independent systems: i) the detector unit (top right) powered from batteries (30-35 VDC) and ii) the rest of the instrument powered by mains (230 VAC).

The battery-powered sensor board has been outlined in detail before (c.f. detector unit section).

The remaining instrument modules require external power with +5.0VDC, +1.5VDC and -2.0VDC voltage rails. These rails have different functions and requirements which have been described in the hardware overview above.

All external power supplies were connected to mains via an isolation transformer[12] by Rätt Kraftförösörjning RKA AB[13] (model: RDS 125). This device prevents common ground loop pick-up and reduces voltage spikes or other transient events caused by power-demanding equipment [25].

Additionally, all external cables entering the radiation detector are wrapped around a ferrite material to further reduce external interference. The combination of ferrite cores and the decoupling transformer have improved the noise pickup of the system which previously caused erroneous readings (data not shown). Many instrument modules also feature internal voltage rail filtering.

---

[12] Noise Protection Transformer in data sheet.

[13] Rätt Kraftförösörjning RKA AB webpage: `http://www.rattkraft.se`

The mains 230VAC are used by two power supply units (PSU): i) a high-quality, filtered and dual-line laboratory bench supply with voltage rails of V_{SS} =-2.0VDC and V_{DD} =1.5VDC. Both lines were measured with a current consumption of $I \leq 20$ mA each. These are connected via the interface board to the VATA465 card. The additional 3.3VDC line is connected also via the interface card but from the OBC 3.3VDC output.

The two most power-consuming modules, the OBC and FPGA boards, are powered by a regular Samsung 5.0VDC charger with USB adaptor. Each of the modules feature its own on-board PSU. It should be noted that the Raspberry Pi B+ (OBC) powers the FPGA board via it USB connection.

The OBC generates in addition 3.3VDC and 1.8VDC via a dual step-down converter (model: RT8020AGQW). The FPGA converts the supplied 5.0VDC to 3.3VDC, 2.5VDC and 1.2VDC via three LDOs (model: LD1117).

The power consumption of the individual modules are:

- VATA465 card: P_{SS}= 40 mW, P_{DD} = 30 mW, 3.3VDC depending on count rate, estimated at less than 20 mW. Total: $P_{ASIC} < 90$ mW.
- Raspberry Pi B+: < 1.5 W (assuming medium CPU load, source: Raspi.tv[14])
- FPGA board: ca. P_{FPGA} =250 mW
  of which Spartan-3E: ca. 90 mW (according to Xilinx XPower Analyzer (simulation, default settings).
- Si-diode (worst case): $I = 100$ nA at $V_{Bias} = 35$ V, $P_{diode} = 3.5$ μW.

Therefore the total instrument power is estimated at $P_{total} = 1840$ mW. (Calculation see footnote[15].)

The dominant power consumer is the OBC with approx. 1.5 W. In future iterations a microcontroller can meet significantly lower power requirements.

---

[14] `http://raspi.tv/2014/how-much-less-power-does-the-raspberry-pi-b-use-than-the-old-model-b`

[15] $P_{total} = P_{ASIC} + P_{OBC} + P_{FPGA} + P_{diode}$ = 90 mW + 1500mW + 250mW + 0 mW = 1840 mW.

3.2.3 Software

The development of software is equally important to the electrical and mechanical aspects described in the section before. The following text splits into two parts: i) the OBC programmed using Python and ii) the FPGA software written in VHDL. Both systems require fundamentally different approaches which are outlined below. However, only when both function together at the same time the instrument can be operated and take data.

It should be noted that the text assumes basic knowledge of the Linux operating system (OS), Python and VHDL. Further reading is provided in the text and bibliography. The post-processing routines will be treated separately in one of the following chapters.

Each section will state the software's purpose and structure, relevant hardware for operations, debugging and testing as well as utilised libraries and other resources.

3.2.3.1 On-board Computer and VATA465 ASIC

3.2.3.1.1 Overview and requirements

The OBC is the interface of the instrument with the outside world. The device is connected via Ethernet to the local network. In addition, it may send data via email which is useful to track the progress of or identify problems during long measurements. The user can setup the type of measurement and its parameters. Internally, the OBC is i) in control of the VATA465 configuration register and ii) able to read-out the individual counter registers on the FPGA.

In summary the OBC shall be able to carry out the following tasks:

OBC.A: Configure and read the VATA465 356-bit configuration register via a serial interface in accordance to [41].

OBC.B: Interface with the FPGA via a quasi-SPI interface. The OBC will act as SPI master.

OBC.C: Retrieve individual counter values using OBC.B and detect counter overflows.

OBC.D: Store the data with timestamps in a file on the local machine.

OBC.E: The OBC and its software have to be remotely accessible and controlled via Ethernet.

OBC.F: Optionally the measurement file(s) should be send via e-Mail to the user. This requires Internet access of the OBC.

These tasks are subject to the following requirements and specifications:

- A Raspberry Pi B+ is used as OBC (3.3VDC logic levels).
- The OBC will run the Rasbian OS, version[16] ”Wheezy” (dated: 2015-02-16), a Debian-based Linux distribution for the ARM6 architecture.

---

[16] Earlier versions have been used in previous development stages.

- Python (version: 2.7.6) is to be used.
- The Python library RPi.GPIO[17] (version: 0.5.9 or later) will be utilised to control the OBC GPIOs.
- The quasi-SPI data is transmitted LSB-first.
- The Secure Shell (SSH) network protocol is used to remotely control the OBC.

3.2.3.1.2 Implementation

The above tasks were implemented using and combining the advantages of a Raspberry Pi B+, a cheap and easily available SoC system, and Python, a simple but powerful interpreter programming language.

Two custom Python classes have been written:

- `ASIC_CONF.py`
- `FPGA_READ_OUT_CLASS.py`.

Both rely on the readily available Python library `RPi.GPIO`. This library allows to control and register the available GPIO pins on the Raspberry Pi. Below the two self-written classes and their relevant public functions will be described.

Description of Python class ASIC_CONF.py

The Python class `ASIC_CONF.py` has been written by Julian Petrasch with contributions of the author and is used with permission[18] for this master thesis. Julian is a CPT-SCOPE team member and has carried out the programming during a work placement at IDEAS in early 2015. Within `ASIC_CONF.py` only the following two public functions have been used for the master thesis work:

- `setHighGainChannel(` N_{channel}, $W_{\mathrm{a/b}}$, $T_{\mathrm{thres.}}$ `):`
  Purpose:
  Set the local register configuration for the threshold of ASIC input channel N_{channel} for the lower or upper trigger window ($W_{\mathrm{a/b}}$) to value $T_{\mathrm{thres.}}$. Only works for high-gain input channels IN_x, $x \in [0, 15]$.
  Input:
  N_{channel} - channel number, type unsigned integer, valid range: 0-15,
  $W_{\mathrm{a/b}}$ - upper or lower trigger window, type: character - only valid: 'a' or 'b',
  $T_{\mathrm{thres.}}$ - threshold for DAC in the respective trigger channel, type: unsinged int (8bit, range: 0-255);
  Output:
  counter value, type: unsigned integer (32 bit).
- `sendToAsicAndVerify():`
  Purpose:

---

[17] Available here: `https://pypi.python.org/pypi/RPi.GPIO`.

[18] Personal communications with J. Petrasch, Mar. 2015

Send the local ASIC configuration register to the VATA465 via a serial interface and validate it by reading it back.
Input:
none
Output:
none, unless error occurs prompting a text message to screen.

It should be noted that there are several other public functions available to configure specific sections of the local ASIC configuration register f.i. for the low-gain channels. The public functions are relying on several private one which are not accessible from outside. For brevity these are not explained in this thesis but are documented in the Student Experiment Documentation for BEXUS: CPT-SCOPE (v.2.2.) [53]. The source code can be provided and both are available on request.

Description of Python class FPGA_READ_OUT_CLASS.py

In order to communicate with the FPGA logic a quasi-SPI master has been implemented in the Python class `FPGA_READ_OUT_CLASS.py`. The module has been written by the author with assistance of Julian Petrasch. The class `FPGA_READ_OUT_CLASS.py` provides only one relevant public function, namely:

- `readCounter(`i`):`
  Purpose:
  Obtain the value of the counter register with address i.
  Input:
  i - address of requested counter, type: unsigned integer (8 bit, range: 0-255),
  Output:
  counter value, type: unsigned integer (32 bit).

The class implements a SPI master closely following the SPI mode 0: CPOL=0 and CPHA=0 [37]. This means that data is read on rising edges only and the clock line (*SCLK*) is low when no SPI communication is on-going.

Software SPI has been used instead of the existing hardware SPI of the Raspberry Pi B+. In this way one could easily change the GPIO pins and adapt their behaviour to the self-written quasi-SPI protocol. The successful use of software SPI is also thanks to the ability of the FPGA quasi-SPI slave to handle low speeds, of around 40 kHz or less, and delays caused f.i. by OS background tasks. In Python it is not possible to control the GPIOs with higher speeds than 40 kHz unless an extension is written f.i. using the programming language C with appropriate libraries and drivers.

The details to the implemented quasi-SPI protocol will be described and discussed in the following section on the FPGA software implementation.

Description of the count rate determination

For all measurements count rates $R_j^{(\mathrm{k})}$ are deduced from the following parameters:

- $t_i(j)$ - time at the beginning of the current data point j,

- $t_f(j)$ - time at the end of the current data point j,
- $C_i^{(\mathrm{k})}$ - Counter value for address k at time t_i,
- $C_f^{(\mathrm{k})}$ - Counter value for address k at time t_f.

These result into two relevant parameters for measurement j:

- the count rate $R_j^{(\mathrm{k})}$
- and the mid-point time $t_m(j)$.

The mid-point time $t_m(j)$ is deduced as follows:

$$t_m(j) = t_i(j) + \frac{1}{2}\,\Delta t(j), \quad \text{with :} \quad \Delta \mathrm{t(j)} = \mathrm{t_f(j)} - \mathrm{t_i(j)}. \tag{3.1}$$

Here reflects $\Delta t(j)$ the real integration time for the data point j, which ideally should be identical to the nominal integration time t_{exp}, specified in the measurement script. This calculation is simple and implemented using the UNIX system time t of the OBC. In order to access t the standard Python libraries `time`[19] and `datetime`[20] are used. While the former is absolutely necessary and used to obtain t, the latter is utilised for time structure conversions in order to make them human readable. The accuracy of the applied `time.time()` function is completely satisfactory for typcal exposure times t_{exp} of 10-120 s (data not shown).

First the counter difference $\Delta C^{(\mathrm{k})}(j)$ is determined from the initial $C_i^{(\mathrm{k})}(j)$ and final counter value $C_f^{(\mathrm{k})}(j)$ for counter address k and data point j:

$$\Delta C^{(\mathrm{k})}(j) = \left(C_f^{(\mathrm{k})}(j) - C_i^{(\mathrm{k})}(j)\right) \quad \text{(no overflow)}. \tag{3.2}$$

However, it should be noted that the counter may have experienced an overflow. We will from here on only consider the possibility of a single overflow and not multiple ones.

A single overflow can be detected by the condition:

$$C_f^{(\mathrm{k})}(j) \; < \; C_i^{(\mathrm{k})}(j),$$

i.e. the final counter value is smaller than the initial one. In such case the count difference must be calculated differently to Eq. (3.2):

$$\Delta C^{(\mathrm{k})}(j) = \left(C_f^{(\mathrm{k})}(j) + \left(C_{max} - C_i^{(\mathrm{k})}(j)\right)\right) \quad \text{(single overflow)} \tag{3.3}$$

where C_{max} is the maximal possible value of the counter. For a M-bit binary counter the value is given by:

$$C_{max} = \left(2^M - 1\right).$$

---

[19] Python library `time`: `https://docs.python.org/2/library/time.html`

[20] Python library `datetime`: `https://docs.python.org/2/library/datetime.html`

The software is unable to distinguish multiple overflow events. It is in the responsibility of the experimenter to minimise such possibility by a wise choice of measurement parameters and settings. Namely, by using a sufficiently large counter register (M-bit) or adjusting the maximum exposure time t_{exp} for a given sample.

In both cases the count rate $R_j^{(\mathrm{k})}$ is obtained from the following equation:

$$R_j^{(\mathrm{k})} = \left(\frac{\Delta C^{(\mathrm{k})}(j)}{\Delta t(j)} \right). \tag{3.4}$$

In pseudo code (Alg. 1) each count rate measurement $R_j^{(\mathrm{k})}$ and associated mid-point time $t_m(j)$ for data point j is carried out as follows:

```
Result: Count rate $R_j^{(\mathrm{k})}$, difference $\Delta C^{(\mathrm{k})}(j)$ and mid-point time $t_m(j)$ for data point $j$.
get $t_i(j)$;
get $C_i^{(\mathrm{k})}(j)$;
wait for $t_{exp}$;
get $t_f(j)$;
get $C_f^{(\mathrm{k})}(j)$;
calculate $\Delta t(j)$ according to Eq.(3.1);
calculate $t_m(j)$ according to Eq.(3.1);
if $\left( C_f^{(\mathrm{k})}(j) < C_f^{(\mathrm{k})}(j) \right)$ then
    calculate $\Delta C^{(\mathrm{k})}(j)$ for overflow according to Eq.(3.3);
else
    calculate $\Delta C^{(\mathrm{k})}(j)$ for no overflow according to Eq.(3.2);
end
calculate $R_j^{(\mathrm{k})}$ according to Eq.(3.4);
```

Algorithm 1: Count rate and mid-time determination for counter address k.

The counter values $C_i^{(\mathrm{k})}(j)$ and $C_f^{(\mathrm{k})}(j)$ are obtained from the FPGA via the public functions of the aforementioned Python class `FPGA_READ_OUT_CLASS.py`.

Description of the Python a single channel measurement script

The aim of a measurement is the take N data points for the data tuple $\{j,\, t_m(j),\, R_j^{(\mathrm{k})},\, \Delta C^{(\mathrm{k})}(j)\}$ for a specific ASIC configuration and counter address k. These data tuples and a preceding header shall be saved to a file `f`. In pseudo code (Alg. 2) this may be expressed as:

```
initialise;
open file f;
write header to f;
for $j \in [0, (N-1)]$ do
    set ASIC-configuration;
    get $\{t_m(j), R_j^{(\mathrm{k})}, \Delta C^{(\mathrm{k})}(j)\}$ according to Alg. 1;
    write $\{j, t_m(j), R_j^{(\mathrm{k})}, \Delta C^{(\mathrm{k})}(j)\}$ to f;
    print $\{j, t_m(j), R_j^{(\mathrm{k})}, \Delta C^{(\mathrm{k})}(j)\}$ to screen (optional);
end
close file f;
send email with f (optional);
```

Algorithm 2: Single measurement of N data points using Alg. 1.

The shown procedure in Alg. 2 deserves a number of remarks:

i) The initialisation sections reads the pre-configured measurement parameters and sets the hardware settings accordingly f.i. which GPIOs are used for the quasi-SPI interface. In addition, the constructors for classes `ASIC_CONF.py` and `FPGA_READ_OUT_CLASS.py` are called.

ii) A self-written function (`send_message()`) allows sending an email containing the measurement file `f`. This is optional and defined separately. The email function can be controlled via setting a parameter. The implementation is based on the Python libraries `smtplib`[21] and `email.mime`[22]. This requires the OBC to have Internet available, a SMTP-client installed and a SMTP-server accessible.

iii) The printing of data results or status messages to the command line can be controlled via a parameter and is optional.

iv) A standard ASCII text file is written using built-in Python functions under an user-defined path and file name.

v) The ASIC configuration is controlled via the aforementioned public functions of the Python class `ASIC_CONF.py`. Their parameters will vary for each type of measurement and will be discussed below.

Description of the Python a multi-channel measurement script

The keen observer has seen that procedures shown in Alg. 1 and Alg. 2 only measure the count rate for a single channel with address k. In order to take multi-channel data both procedures have to be adapted to read and process counter values from addresses k_i with $i \in [1, N_{channel}]$. Here $N_{channel}$ stands for the number of channels.

---

[21] Python library `smtplib`:`https://docs.python.org/2/library/smtplib.html`.

[22] Python library `email.mime`:`https://docs.python.org/2/library/email.mime.html`.

In Alg. 1 not only the initial time $t_i(j)$ and counter value C_i^{k} have to be taken once but for each channel k_i individually. This happens before the system waits until the exposure time t_{exp} is over. Likewise, the final values and timestamps have to be read for the different channels k_i. This results in $N_{channel}$ data tuples instead of just one set per measurement.

The measurement procedure (Alg. 2) has to store the $N_{channel}$ data tuples in the file `f`. In the present implementation the data tuples are simply concatenated for each data point j and written to the same line. Currently, only two channels are used ($N_{channel} = 2$), namely the trigger outputs T_OUT01A and T_OUT01B with assigned addresses $k_i = \{1, 2\}$.

Available measurement scripts
There are two measurement types used in this work which require a specific Python script each:

- **Threshold scans**: used for obtaining cumulative energy spectra,
- **Time series**: utilised to take data with a fixed ASIC configuration over a period of time.

Both of them use the aforementioned procedures adapted for the use of two channels. The scripts are written in a way such that they allow for N_{set} measurement runs, as shown in Alg. 2. Hence N_{set} data files are created. These are saved in a sub-folder. The default path is `./data/`. The filename base is defined by the user e.g. `measurement_file` and the current run number N_{set} is appended to the name.

The respective scripts only vary in the ASIC configuration sequence and measurement file format. These will be briefly summarised below.

Threshold scans
In this mode the value of the threshold T_{thres} will be swept within a fixed range $T_{thres}^{(\min)}$ and $T_{thres}^{(\max)}$. The scan starts with the highest DAC threshold values and decrements by an user-configured step-size (default: 1).

The order of threshold values is due to an improved noise performance caused by the reduced pre-amplifier feedback[23]. This behaviour has been verified by test measurements (data not shown).

Both triggers, T_OUT01A and T_OUT01B, have been configured to use the same threshold value T_{thres}. The threshold is changed at each step. The nominal integration time t_{exp} remains the same and is user defined. The measurement script is named `meas_threshold_scan.py`. The latest version is V.1.1-TS.

Usually several scans are taken in order to obtain average values and remove outliers caused by external interference such as energetic cosmic rays. The obtained data sets allow conclusions about the samples energy spectrum in a course way.

---

[23] Private communications with G. Mæhlum, Mar. 2015

Time series

The measurement of time series is carried out by keeping the ASIC configuration fixed and taking data points over a given amount of time. The measurement script is named `meas_fixedthreshold_timeseries.py` and its latest version is V.1.3-FTT.

The thresholds for triggers T_OUT01A and T_OUT01B can be set to fixed but different values $T_{thres}^{(\mathrm{A})}$ and $T_{thres}^{(\mathrm{B})}$, respectively. The integration time t_{exp} and amount of data points N are user defined.

It should be noted that due to the short but non-zero amount of time (ca. 0.05 s) it takes to write to the file and appearing other OS background tasks, the true experiment run time will be longer than the estimated integration time. Furthermore, measurements with intervals of less than 1/10 s are not possible. A possible solution would be to buffer the data and write larger blocks. However, for all practical purposes concerning the present work no limitation by the above minimum time interval has been found.

Time series where only used to study background trigger rates mainly caused by cosmic rays. A slightly simplified version was also used for count rate measurements as a function of distance or absorber thickness. These will be explained in detail in the next chapter.

Header information

Each file `f` written by the measurement scripts will contain a basic header providing enough information about the experiment to carry out an useful analysis of the data. The given information is preceded by a hashtag # to mark it as comment. In this way the post-processing scripts can skip these lines and only evaluate the data points regardless of the number of header lines.

The following information is provided with the latest versions of the measurement scripts:

- Trigger DAC threshold information (range for threshold scans, fixed values for time series.)
- Nominal exposure time per data point t_{exp}
- Sample information
- Used input channel(s) and respective output triggers
- Counter bit length M
- Measurement script type and version
- Comments (contains ambient temperature, environmental / setup details, etc.)
- Start time and date in UTC for the measurement
- Path and filename
- Heading explaining data tuples and their units.

How to run a measurement

In this final paragraph about the OBC software a typical measurement run and its configuration will be outlined. The user logs into the OBC either via the Ethernet using a SSH client such as PUTTY, or directly uses the Raspberry Pi B+ on a monitor, mouse and keyboard setup. We will assume the user uses SSH allowing for remote access[24] and the Raspbian OS in the specified version ”Wheezy” (dated: 2015-02-16). Furthermore, the user is able to carry out simple UNIX command line operations such as changing directory or moving files.

In a specific folder (default: `/home/pi/Desktop/CPTSCOPE`) the measurement scripts are located. In the default configuration a sub-folder `data` has to be present to write the measurement files to. It is important to remove all files from previous runs since they may be overwritten.

The user then opens the measurement script in any text editor such as VIM. Then the measurement parameters and header information is modified. The user variables for the email and print function can be set as well. After all settings are saved the script can be run.

In order to do so one has to have administrative rights since hardware GPIOs will be accessed and modified. This is done by the preceding command `sudo`. All following commands will be executed with elevated privileges. For example the time series script is then started[25] by the command line using Python:

```
sudo python meas_fixedthreshold_timeseries.py
```

The user is then prompted with basic information confirming that the measurement is ongoing. If activated the script will prompt each data tuple. In the end of the measurement a message is prompted and an email with the data file send to a specified recipient, given that this option has been activated.

In case the script needs to be terminated the following key combination can be used: CTRL + C. This will throw an error indicating that the script has been terminated in an unexpected way.

Finally, the data can be downloaded using a FTP-client on the local machine, accessing the OBC via the network. Alternatively one can transfer the data using a flash drive or process them directly on the OBC.

---

[24] In order to have long term measurements running and being able to log off the remote machine without stopping the measurement the `screen` window manager is recommended to be installed and used. More information is available here: `http://www.gnu.org/software/screen/manual/screen.html`.

[25] After restarting the OBC it is recommended to start a measurement with a single data point to set the GPIO pin configurations correctly. Otherwise the first data point may contain erroneous count rates.

3.2.3.2 High-speed Counter - FPGA

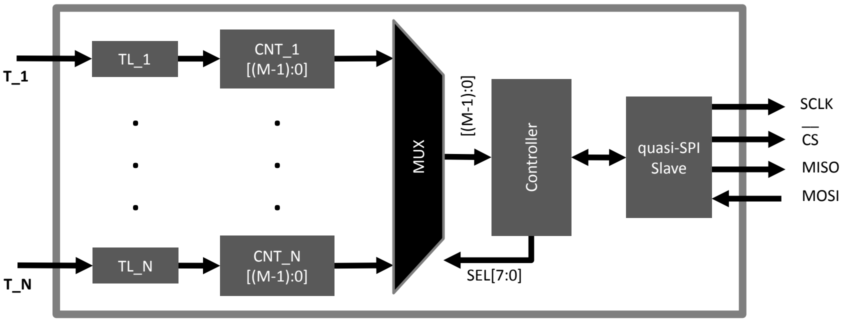

Figure 3.18: FPGA layout.

3.2.3.2.1 Overview and requirements

The FPGA module shall be able to carry out the following tasks (cf. Fig. 3.18):

A: Serve as counter for registered trigger pulses from N inputs, *T_x* with $x \in [1, N]$.

B: A trigger acceptance logic *TL_x* allows only valid events to increment the respective counter and synchronises the pulses to the FPGA global clock domain.

C: A total of N counters (*CNT_x*) with M-bits each shall run in parallel.

D: The individual counter values *CNT_x* shall be accessible via a quasi-SPI interface with the FPGA being in slave mode, while the OBC serves as master.

The following requirements must be met in addition:

- Two individual counters shall be used ($N = 2$).
- The counter bit length shall be 32 bits ($M = 32$). This allows for counter values in the range of 0 and 4,294,967,295 ($= 2^{32} - 1$), making counter overflows unlikely and easily recognisable.
- Each counter can be accessed via an 8-bit address, allowing for a maximum number of 256 individual registers.
- The SPI slave must function at a serial clock ($SCLK$) frequency of the order of 10 kHz.
- The maximum possible design speed must exceed 40 MHz at least to allow for high count rates and using the full potential of the used FPGA hardware running at 32 MHz.
- The design must fit onto and work on a Xilinx Spartan-3E (model: XC3S500E, [65]).

3.2.3.2.2 Implementation

The schematic layout of the FPGA implementation is shown in Fig. 3.18 where the notation follows the components and labels used in the above overview and requirements. The FPGA implementation was carried out in VHDL[26] according to the IEEE 1076-2008 standard (see [33, 47] for details). For good introductions and tutorials on VHDL the reader is referred to [15, 40, 47].

The VHDL source code for all modules is available on request.

Introduction

V

Software environment:

In this work we will use the freely available Xilinx ISE WebPACK[27] software suite (version: 14.7). It features a complete development environment, simulators and FPGA design and synthesis tools. The ISE WebPACK offers free access to the complete FPGA development toolchain for many older Xilinx FPGA families such as the Spartan-3E or Spartan-6. More recent and powerful models such as the Xilinx Virtex family require the new Xilinx Vivado Design Suite for which a license must be purchased or is provided with bought hardware.

For all VHDL modules the following standard libraries have been used:

- `IEEE.std_logic_1164`
  - logic types (IEEE 1164-1993, [31]),
- `IEEE.numeric_std`
  - mathematical operations, unsigned / signed types (IEEE 1076.2-1996, [32]).

Digital Circuit Design

In this section we will describe the design of the digital circuitry. It should be noted that for brevity only the module topography is described. The source code fall all modules is available in the appendix or on request. It is assumed that the reader has basic knowledge of FPGA and digital circuit design. Basic proficiency in VHDL is recommend.

Top Module (level 0): `cptscope_top_final`

On the top level the device, a multi-channel high-speed counter with SPI-slave, is implemented in the top module `cptscope_top_final` as shown in Fig. 3.19. It has the in- (left) and output (right) ports. These are summarised in Tab. 3.6.

These in- and outputs are the only ports connected to the outside world i.e. the interface card. It should be noted that ports *TEST*, *TEST_PULSE_0* and *TEST_PULSE_1* are optional

---

[26] VHDL stands for: Very High Speed Integrated Circuit (VHSIC) Hardware Description Language.

[27] `http://www.xilinx.com/products/design-tools/ise-design-suite/ise-webpack.html`

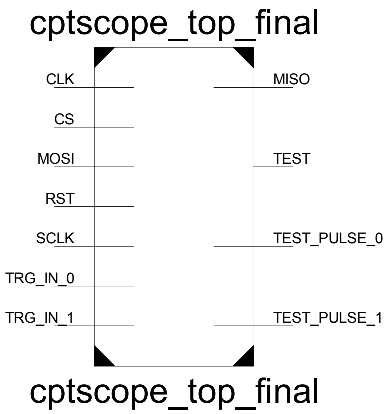

Figure 3.19: FPGA top module (level 0) `cptscope_top_final` schematic. Overview only showing in- (left) and outputs (right) accessible to the outside world.

Table 3.6: In- and output ports of the `cptscope_top_final` top module. The PCB signal labels are taken from the interface card (cf. Tab. 3.2).

Signal	Direction	Description	PCB signal label
CLK	in	Global clock (32 MHz), FPGA board	CLK
CS	in	SPI CS line	FPGA_CS
MOSI	in	SPI MOSI line	FPGA_MOSI
RST	in	FPGA global reset line, connected to GND	N/A
SCLK	in	SPI SCLK line	FPGA_SCLK
TRG_IN_0	in	Trigger input, channel 1, T_OUT01A	N/A
TRG_IN_1	in	Trigger input, channel 1, T_OUT01B	N/A
MISO	out	SPI MISO line	FPGA_MISO
TEST	out	Test output, reconfigurable for debugging	N/A
TEST_PULSE_0	out	Creates output pulses in config. intervals	N/A
TEST_PULSE_1	out	Creates output pulses in config. intervals	N/A

and serve for testing and debugging purposes. In particular the output *TEST* may be connected to one of many internal signals. In the present implementation it is not connected at all.

The top module connects all other modules internally and is highest in the module hierarchy as shown in Fig. 3.30.

The level 0 and 1 module tree is as follows:

cptscope_top_final -
    counter0 complete_counter_unit_v2
    counter1 complete_counter_unit_v2
    spi_slave01 spi_slave
    TEST_PULSE_0 misc.

In this description we have shown the top (0) and next level (1) only. The labels indicate the instantiated component by their identifier (bold) and the name of the underlying module (regular). For instance `spi_slave01` is an instantiation of the module `spi_slave`.

It should be noted that the TEST_PULSE_0 is generated from a simple binary counter (not shown in Fig. 3.30). Whenever a specified maximum value is reached the output fires, i.e. is logic high, for a single clock cycle and then resets the counter to zero. By choosing the correct maximum value in respect to the global clock frequency of 32 MHz one can control the period between two events. Both outputs, *TEST_PULSE_0* and *TEST_PULSE_1*, are connected to the output of module TEST_PULSE_0.

We will now describe the remaining modules in more detail.

Module (level 1): `complete_counter_unit_v2`

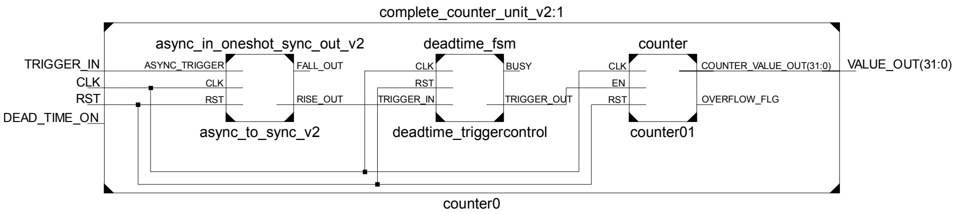

Figure 3.20: FPGA schematic of the module (level 1) `complete_counter_unit_v2`. Besides in- and outputs it also shows the internal submodules (level 2).

This module has three functions which are referenced to the objectives described before:

- synchronise and register only valid triggers (part of *TL_x*)
- use a deadtime module (optional) to fix a re-triggering issue (part of *TL_x*)
- count valid events using a M-bit counter (part of *CNT_x*)
- provide the counter value to other modules (part of *CNT_x*).

The module is composed of three sub-modules as shown in the following hierarchy tree with levels 1 and 2 as compared to the top module:

complete_counter_unit_v2 -
    async_to_sync_v2 async_in_oneshot_sync_out_v2
    deadtime_triggercontrol deadtime_fsm
    counter01 counter

This is also visualised in Fig. 3.20. The module's in- and outputs as well as their function are described in Tab. 3.7.

The underlying modules of level 2 for `complete_counter_unit_v2` will now be outlined.

Table 3.7: In- and outputs of module `complete_counter_unit_v2`.

Signal	**Direction**	**Description**
TRIGGER_IN	in	Async. trigger input
CLK	in	Global clock
RST	in	Global reset
DEAD_TIME_ON	in	Switch for activation of deadtime module
VALUE_OUT(M:0)	out	Counter value (M-bit bus)

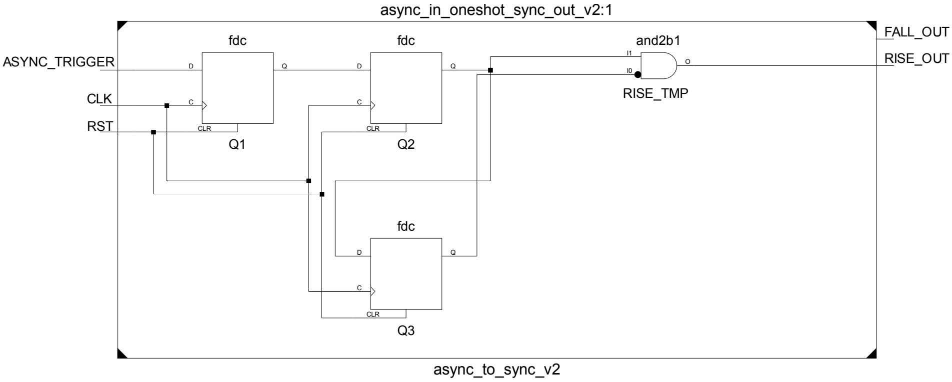

Figure 3.21: A two stage DFF synchroniser with rising-edge detection using a total of 3 DFFs and one AND gate. The falling edge detection is not connected.

Module (level 2): `async_in_oneshot_sync_out_v2`

The raw trigger inputs from the VATA465 ASIC are asynchronous. However, in digital circuits it is mandatory to work synchronous to the global clock domain[28]. In order to achieve synchronisation and the selection of correct trigger pulses (cf. *TL_x*), the module `async_in_oneshot_sync_out_v2` was written.

Besides synchronisation, it only fires once per detected rising edge. This is relevant since the regular pulse duration of the ASIC trigger may be up to 120 ns long (data not shown), depending on resistive and capacitive load of the trigger pin T_OUTxA/B. Within this time period the 32 MHz FPGA clock has undergone several ticks. While the trigger signal is above or equal the high logic level for the LVCMOS33 standard the counter will increment by one if the module `async_in_oneshot_sync_out_v2` were not present. This would lead to false readings and must be mitigated.

A standard approach has been implemented using two flip-flops (FF) as synchroniser followed by a third FF and comparing logic to detect a rising or falling edge. Data flip-flops (DFF) which are clocked using the FPGA global clock (CLK) are used and connected to the global reset line (RST). This implementation has been adopted from [19] where

---

[28] Here we use only one clock domain. In general several are possible and regularly used for more complex circuits.

the aspects of synchronisation are well outlined. This subject is also discussed in many introductory FPGA text books.

In Xilinx Spartan-3 devices the synthesis tool tries to implement the circuit using a Shift Register LUT (SRL, [64]), where LUT stands for Look-up table. In this case a SRL16 macro has been implemented bye Xilinx ISE which may cause false synchronisation. This has been discussed online on the Xilinx forum quite thoroughly[29]. In order to avoid this behaviour, the VHDL code has been written such that the Xilinx toolchain is forced to implement 3 DFFs during synthesis.

The raising and falling edge detection is done by the following simple logic comparing the bit vector ("Q_2 & Q_3", cf. 2-bit shift register), where the output value (Q) of the second and third DFF are concatenated. A $\{$ falling, rising $\}$ edge is given for the resulting logic vector $\{$ "10", "01" $\}$. The result is provided to the respective output pin, *FALL_OUT* and *RISE_OUT*. In the present design no falling edge detection was necessary. Therefore, its logic got removed in the optimisation process and only the rising edge detection using an `and` gate (RISE_TMP) to compare Q_2 and $\bar{Q_3}$. This is shown in Fig. 3.21, along with the 3 DFFs.

The circuit has been tested in simulations and using the test pulse generators with varying external cable delay lines to cause asynchronisation (data not shown).

The module is providing a synchronous single firing logic pulse output for each valid input trigger pulse. In the next paragraph the following logic unit, a deadtime counter is explained.

Module (level 2): `deadtime_fsm`

The VATA465 high-gain channels, low-threshold trigger outputs T_OUTxA suffer under specific conditions retriggering (described in the technical background section). This means that for a single valid event the trigger out may fire several times. Such behaviour would lead to false counter readings.

The issue has been investigated, among other in the author's specialisation report [54]. For all relevant measurement samples the retriggering time was studied (data not shown). This lead to the following conclusions:

- Trigger values $T_{thres} < 10$ should not be used for triggers T_OUTxA.
- For the valid threshold range a deadtime window of $t_{off} = 10$ μs is recommended to be used for triggers T_OUTxA.

In both cases the values may change depending on the input charge to the pre-amplifier[30]. The above values have been determined for a Sr-90 sample which deposits the highest expected energy into the detector (data not shown). In addition, the effect of cosmic rays has been studied which conform with the above findings (data not shown).

---

[29] see: `http://forums.xilinx.com/t5/Implementation/SRL16-as-a-synchronizer-again/td-p/144806`.

[30] Personal communications with P. Påhlsson, Apr. 2015.

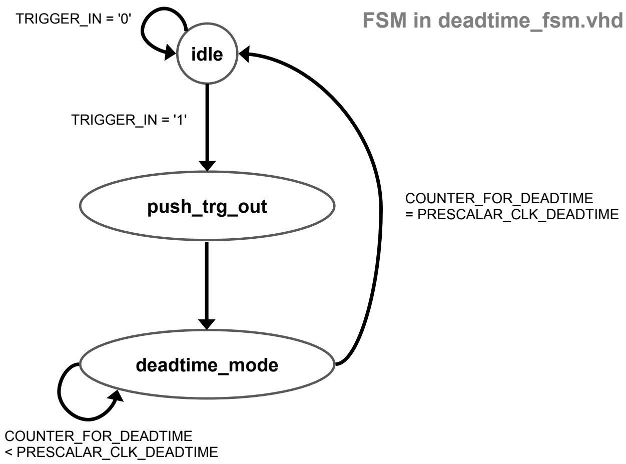

Figure 3.22: Deadtime FSM module (level 2), state diagram.

Due to this behaviour a deadtime counter had to be implemented. The strategy used was to let the first valid trigger pass and then block all consecutive triggers for the deadtime t_{off}.

This has been realised using a finite state machine (FSM). The FSM is described by Fig. 3.22. In FPGA development FSMs are often utilised to create event-based logic. These are easily implemented using the built-in type `state_type`.

We will now outline the associated FSM for each of its three states:

`idle` -

The FSM is in the idle after a global reset (*RST*), release from state `deadtime_mode` or when no trigger is detected. Upon registering a valid trigger on the input port (*TRIGGER_IN* next state, `push_trg_out`, is entered.

`push_trg_out` -

In this state the module provides a single firing of its output port (*TRIGGER_OUT*). On the next clock cycle it immediately enters the next state, `deadtime_mode`.

`deadtime_mode` -

The module allows no further input trigger events to pass until the deadtime t_{off} has passed. this is implemented with a binary counter which increments the register *COUNTER_FOR_DEADTIME* by one every clock cycle until it reaches the value *PRESCALAR_CLK_DEADTIME*. Once this occurs the counter resets and jumps back to state `idle`.

It should be noted that the deadtime FSM can be deactivated by choosing the parameter *DEAD_TIME_ON* = ’0’ in module `complete_counter_unit_v2`. In this case the Xilinx toolchain removes the related logic and passes every valid trigger event to to counter which will be described next.

Module (level 2): `counter`

In the last component within the module `complete_counter_unit_v2` the number of valid trigger events is accounted for in a M-bit binary counter (*CNT_x*). The trigger pulses may have passed the deadtime FSM or not depending on the settings on the parent module `complete_counter_unit_v2`.

The counter is implemented in a way that it increase its value every clock cycle if and only if its *EN* is active-high. This is caused by the passed on trigger pulse. The module is also connected to the global reset (*RST*). In addition, it has an overflow flag. However, in the present design it is not connected.

Currently, a 32-bit ($M = 32$) counter is in use, allowing for low probability of an overflow. Such event can be detected inside the OBC readout software and be accounted for. The output of the counter is a M-bit parallel data bus which also serves as output of the parent module `complete_counter_unit_v2`.

With this submodule the description of the event counting logic is complete and we will outline the remaining SPI slave and multiplexer (MUX).

Module (level 2): `MUX`

In order to access the correct counter register a multiplexer (MUX) was necessary. Since only two counters are presently in use the MUX has not been implemented in a separate module but was directly placed inside the top module `cptscope_top_final`.

The module `MUX`, shown in Fig. 3.30, has been added for clarity and to explain the interconnection between the counters and the SPI slave FSM.

The MUX is a simple asynchronous one based on the VHDL `case` command [40]. It uses little resources and since all inputs are synchronous to the global clock domain it can be used[31]. A synchronous version has also been implemented. Since both perform equally the asynchronous one has been chosen.

The M-bit counter values from counter0 and counter1 serve as input to the MUX. The selection is done by using the 8-bit address bit vector from the SPI slave (see below, *ADDRESS(7:0)*). Here the following address assignment has been done:

- *ADDRESS* = ”10000000” $\Rightarrow$ output = counter0;
- *ADDRESS* = ”01000000” $\Rightarrow$ output = counter1;
- for all other cases a 32-bit bit vector with zeros (’0’) is provided as output.

Module (level 1): `spi_slave`

The FPGA communicates with the OBC via a quasi-SPI (hereafter called SPI) interface. While the FPGA is the SPI slave the OBC is the SPI master.

---

[31] Personal communications with B. Najafiuchevler, Mar. 2015.

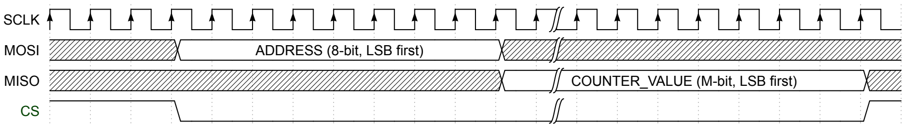

Figure 3.23: SPI transmission protocol waveform for FPGA, created using the online WaveDrom application.

The (standard[32]) Serial Peripheral Interface (SPI, [37]), also known as four-wire serial bus, is a synchronous serial communication protocol. It requires four signal lines which will be explained below:

SCLK -
serial clock (from master), synchronisation.

CS -
chip select (from master), active low, indicates on-going transmission when low.

MOSI -
master out slave in (from master), data transmitted from master to slave.

MISO -
master in slave out (from slave), data transmitted from slave to master.

SPI allows for full-duplex communication between devices. For each additional slave the master must provide an additional CS line or a ”daisy chain” configuration must be implemented with compatible hardware. In the present case only one slave is used and hence the aforementioned four signals are sufficient.

A transmission is initiated by the SPI master pulling the CS line low and the SCLK signal toggles. There are four different SPI modes as outlined in [37]. In the present case mode 0 is used i.e. the SCLK line when idele is low (CPOL=0). Then at each SCLK rising edge (CPA=0) the values of the MISO and MOSI line are read by the master and slave, respectively. In many examples the transmission is starting with the most-significant bit (MSB) first f.i. as described in [56].

However, in the present implementation the least-significant bit (LSB) is sent first. For the implemented SPI-slave a typical transmission is shown in Fig. 3.23.

Assuming SPI mode 0 and LSB-first: the 8-bit address is sent by the master on the MOSI line first. This address is used by the MUX to provide the correct counter value which has been requested.

Then the slave transmits the respective 32-bit counter value LSB-first. After this the master pulls the CS line high which terminates the transmission. The total transmission is 40 SCLK cycles long. Due to the fact that LSB-first is used and the transmission protocol

---

[32] In fact there are many ”standards” for SPI; one example being the STMicroelectronics protocol implementation [56]. It should be noted that their signal name varies with the one used in this text.

being non-standard the implemented serial communication protocol is referred to as quasi-SPI.

At a SCLK frequency of 40 kHz this translates to a total transmission time of 1 ms per counter value. This assumes that no OBC OS background tasks may interrupt the on-going transmission or a lower frequency is used. However, a typical reading of a counter value should not take longer than 5 ms.

Usually, SPI uses significantly higher speeds on the order of 1 MHz. However, due to limitations in the Python implementation to access and control its GPIOs one has to accept lower speeds for software-based SPI (soft-SPI). This has been found acceptable.

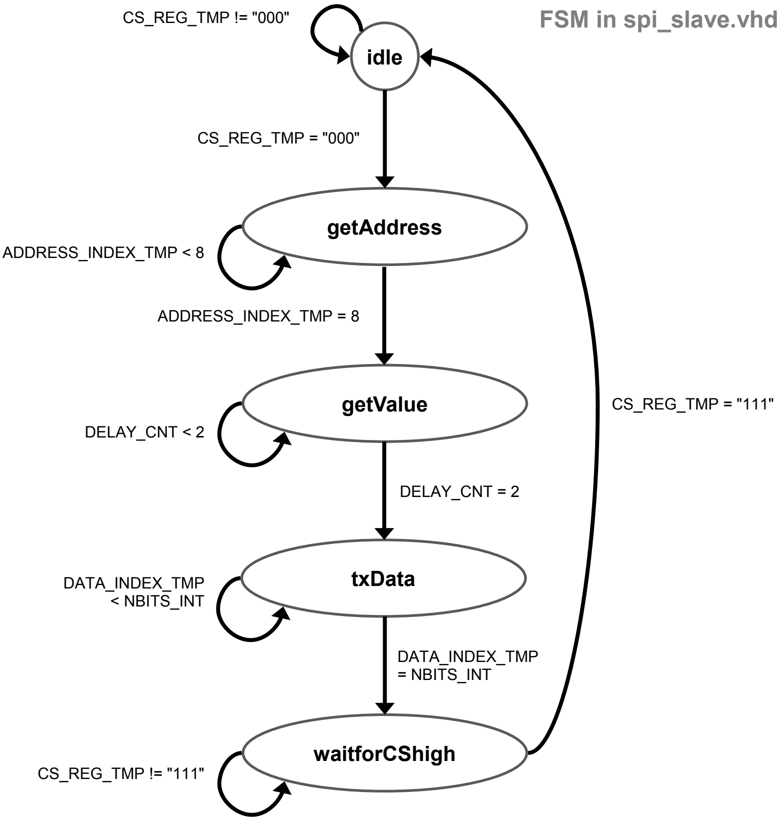

Figure 3.24: FPGA FSM for SPI slave.

On the FPGA the SPI slave is implemented using a FSM. It uses five different states as shown in Fig. 3.24. These and their behaviour are described below.

In order to recognise an on-going transmission the CS line is sampled in a process running parallel to the FSM. For robustness and better edge detection a 3-bit shift register is implemented storing the last three sampled logic values for the CS-line. This register is named *CS_REG_TMP*. Similarly, the SCLK signal is also sampled with a 3-bit shift register (*SCLK_REG_TMP*) in order to carry out edge detection. This approach also allows correct transmissions even when irregular OBC-generated SCLK timings occur.

The SPI slave FSM will now be briefly outlined:

`idle` -
: Until the CS line goes low or a global reset occurs (*RST*) the FSM remains in state `idle`. All SPI slave internal registers and counters are reset. When the shift register *CS_REG_TMP* = ”000” takes the value the FSM enters the next state, `getAddress`.

`getAddress` -
: In this state the SPI slave receives the 8-bit address of the requested counter. This is done by reading the MOSI line at every SCLK positive edge, in total eight times (LSB-first). Once the counter *ADDRESS_INDEX_TMP* = 8, the next state is entered, `getValue`.

`getValue` -
: A delay counter, *DELAY_CNT*, is incremented at CLK (!) speed while the counter register value is loaded. Theoretically this state is not necessary. However, by including a waiting state the transmission improved significantly. When the delay counter is equal 2 (i.e. 3 CLK cycles = ca. 94 ns) the next state,`txData`, is entered. The caused delay is negligible compared to the SCLK period (ca. 25 μs).

`txData` -
: In this state the requested 32-bit counter value is transmitted LSB-first. The MISO line is toggled at every SCLK falling edge such that the OBC reads the proper value at the rising edge as defined in SPI mode 0 [37]. Once the bit counter *DATA_INDEX_TMP* has reached the number *NBITS_INT* (=32), the final state is entered: `waitforCShigh`.

`waitforCShigh` -
: Here the shift register *CS_REG_TMP* is monitored. When the SPI master releases the slave the CS line will go high. Hence, when *CS_REG_TMP* = ”111” is detected the FSM returns to the initial state `idle`. As long as this condition is not met the FSM remains in the present state.

The SPI slave also catches glitches of the transmission and returns to the `idle` state. A busy flag during the transmission and a test output are provided but not utilised in the final version.

Before the SPI slave implementation the FPGA actually severed as SPI master. A different module was successfully written and tested. However, due to the non-deterministic delays on the OBC side this implementation was not working in many transmission causing erroneous readings. The SPI slave implementation has proven to be stable and reliable. Higher transmission speeds are possible by at least a factor of 10 based on the FPGA design.

FPGA implementation summary and remarks
It was possible to successfully implement a high-speed counter with two available channels. 32-bit counters are used, along with an asynchronous multiplexer and SPI slave. The design can be synthesised and works on the Spartan-3E FPGA. The slowest possible speed in the VHDL design is 41.8 MHz (based on Xilinx ISE design simulation). This value is still higher than the actual FPGA board speed of 32 MHz. In terms of FPGA hardware utilisation only 1% of the available flip-flop slices and 3% of the 4-LUT are used. Of the available 48 GPIOs on the used Papilio One 500K FPGA board only 10(+1 CLK) are used (21%). Three of them being optional for testing and debugging.

Hence, the present design is light weight and the Spartan-3E can be used for designs involving more input channels, as required by CPT-SCOPE.

3.3 Selected Simulation and Test Findings

Both the hard- and software was characterised or often debugged during the course of this project. While many technical points regarding the hardware and electronics have been discussed at the respective section above, in this section we will on:

- the simulation of VHDL modules,
- and actual tests of the OBC-FPGA quasi-SPI communication.

3.3.1 VHDL module simulations

We will first describe simulation results for the following VHDL modules:

- `complete_counter_unit_v2`,
- `async_in_oneshot_sync_out_v2`,
- `deadtime_fsm`,
- and `spi_slave`.

The simulations were carried out using the free Xilinx ISim (v.: 14.7) software after VHDL code synthesis. For each tested VHDL module a so-called test bench had to be written setting parameters and providing stimuli. For brevity the test benches will be omitted and only simulation results be shown and discussed. For a good introduction to VHDL test benches the reader is referred to [47] or similar text books.

3.3.1.1 VHDL Simulation: `async_in_oneshot_sync_out_v2`

In this test bench the VHDL module `async_in_oneshot_sync_out_v2` is evaluated. The findings are shown in Fig. 3.25. The following signals are shown: i) Global clock

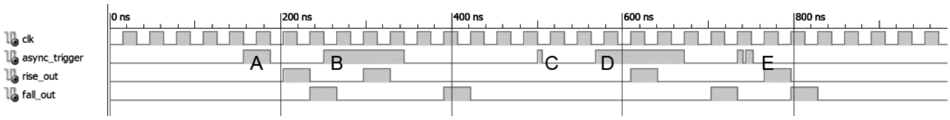

Figure 3.25: ISim simulation results for VHDL module `async_in_oneshot_sync_out_v2`.

(*clk*), ii) an asynchronous trigger input (*async_trigger*), iii) the output for a detected rising edge (*rise_out*) and iv) the detection of a falling edge (*fall_out*).

Five stimuli (A-E) have been given: A) a regular pulse lasting for one CLK period, B) a pulse with duration of three clock cycles, C) a short pulse which disappears before the sampling rising edge, D) a long trigger pulse with small phase shift compared to the main clock and E) two short consecutive pulses with a smaller duration than CLK, only one is present at the sampling CLK rising edge.

From the module description we expect the following behaviour: A asynchronous trigger causes a single firing of the rising and falling edge detection. This is true for a trigger pulse which is present at the sampling positive edge of SCLK.

For the above stimuli this condition is only met for A), B), D) and E). Trigger pulse C) is not sampled and hence not detected. This situation cannot arise for valid triggers in our setup since the trigger pulse has a duration of the order of 100 ns, which is longer than the FPGA clock at 31.25 ns. The same is true for the second pulse in E). Since it is not present at a sampling edge and the circuit has fired already this event will not be reported. As outlined before such case is not valid for our instrument.

The simulation shows nicely that both the rising and falling edge detection works, and only fires once for each valid pulse. The small delay for the edge detection is due to the use of 3 DFFs which are synchronous with CLK.

3.3.1.2 VHDL Simulation: `deadtime_fsm`

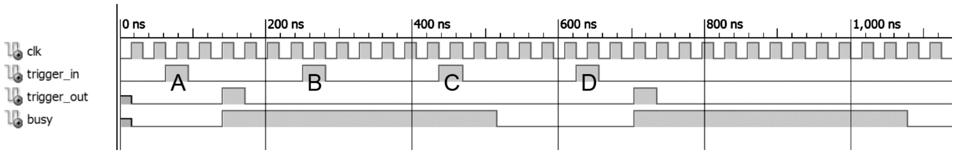

Figure 3.26: ISim simulation results for VHDL module `deadtime_fsm`.

With the module `deadtime_fsm` present a valid input trigger pulse, e.g. from module `async_in_oneshot_sync_out_v2`, may only pass to the output if and only if no other has been detected within a given time t_{off}. In order to test the module four input pulses (all synchronous and one clock cycle long) were prepared: A) a first regular pulse, B) and C) both with the deadtime and D) after the deadtime.

The results for these stimuli are shown in Fig. 3.26. The following lines are shown: i) global clock (*CLK*), ii) input trigger (*trigger_in*), iii) output trigger (*trigger_out*) and iv) a busy status indicator which is high when the deadtime FSM is blocking incoming triggers from propagating.

The expected behaviour is observed, only input pulses A) and D) are let through.

3.3.1.3 VHDL Simulation: `complete_counter_unit_v2`

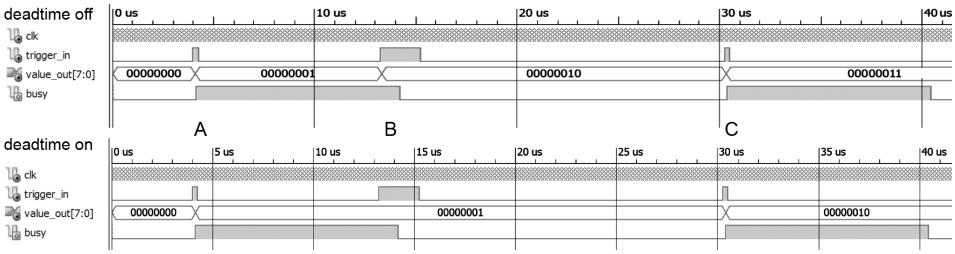

Figure 3.27: ISim simulation results for VHDL module `complete_counter_unit_v2`.

In this simulation the entire module `complete_counter_unit_v2` is used. Three stimuli are provided as asynchronous inputs: A) a regular trigger pulse with 250 ns duration, B) a second longer pulse with 2 μs which begins 9 μs after A) and C) a regular pulse with 250 ns starting significantly later than B). The deadtime is 10 μs and the global clock period 31.25 ns long, identical to the real implementation.

Fig. 3.27 is divided into two sections: the top one has the deadtime FSM deactivated while the lower one has it turned on. Each show the simulation results for identical stimuli A)-C).

The following signals are shown: i) the first line shows the global clock (*CLK*), ii) the asynchronous input trigger (*trigger_in*), iii) the counter value (here 8-bit) and iv) the deadtime FSM busy indicator. When iv) is high the deadtime FSM should prevent inputs from ii) to pass through when active. Furthermore, for each valid trigger (rising edge) the counter value should increase only by one if allowed through the deadtime FSM.

The result is clear: The initial counter value is zero. Upon event A) the counter increases and the deadtime FSM is activated for the lower simulation, as expected. Since B) contributes only a falling edge in the sensitive (*busy* = '0') time period, the trigger event is rejected and the counter value remains the same for the lower graph (deadtime FSM is off). However, the counter value of the top simulation is correctly increased since the rising edge fell within the sensitive time period. Although *busy* is shown to be active the deadtime FSM is simply skipped. The last trigger C) is detected by both settings correctly and the counter increases again by one.

Therefore, the expected behaviour is reproduced by the above simulation result and it is quite likely that the digital logic circuit will function in the real instrument application.

3.3.1.4 VHDL Simulation: `spi_slave`

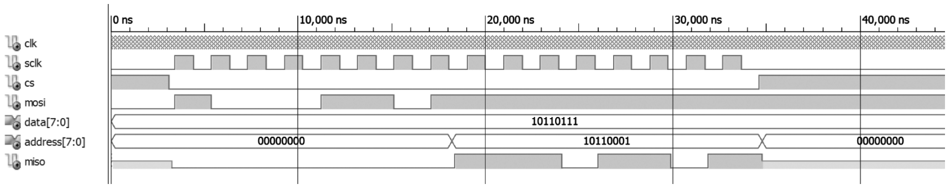

Figure 3.28: ISim simulation results for VHDL module `spi_slave`.

Lastly, the SPI slave FSM will be simulated and its findings are shown in Fig. 3.28. The figure shows the following signals: i) global clock *CLK*, ii) a slower *SCLK*, iii) *CS*, iv) *MOSI*, v) predefined *data*, vi) the receiving *address* register and vii) *MISO* output.

The respective VHDL module `spi_slave` gives the following results with predefined 8-bit *data* = ”10110111” and *address* = ”10110001”: Upon initiating a SPI transmission by pulling *CS* low the SPI slave FSM activates. The MOSI line is read to obtain the 8-bit address LSB first. Once this is completed (see change in *address* value) the *MISO* transmission of the *data* register starts, also LSB first. Once the transmission is complete the *CS* line is set high until the next transaction. The simulation indicates full functionality for the SPI slave implemented on the FPGA.

In the following section the results of two real OBC-FPGA SPI transactions will be elaborated.

3.3.1.5 SPI communication between OBC and FPGA

For this measurement an IKALOGIC ScanaPLUS[33] (V2): 9-Channel, 100MHz Logic Analyser and its data acquisition / analysis software ScanaStudio (v.2.305) has been used. The data of a SPI transaction between the OBC and FPGA is shown in Fig. 3.29. The following lines are shown (top to bottom): i) *CS*, ii) *SCLK*, iii) *MOSI* and iv) *MISO*.

Here VHDL test code was written such that the *data(7:0)* register is equal ”11101101” for *address(7:0)* = ”00000010”. While for other cases the data register would be different, mostly resulting into a zero vector. One can see that the transaction can be separated into 5 sections labelled A1) - D). These are: A1) begin of transaction, *CS* low. A2) string operations and other preprocessing causes delays until B) the *SCLK* line starts toggling and the requested address is send via *MOSI* (LSB first). After completion of phase B) another short delay appears as the Python script modifies the OBC GPIO settings. C) marks the sending of the data register from the FPGA via the *MISO* line (LSB first). The transmission is finished as the OBC sets *CS* high.

The ScanaStudio built-in SPI decoder show the correct results for both the *MOSI* (address) and *MISO* (data) line. Hence confirming that the SPI implementation works on both the

---

[33] IKALOGIC ScanaPLUS: `http://www.ikalogic.com/ikalogic-products/scanaplus-9-channels-100mhz-logic-analyzer/`.

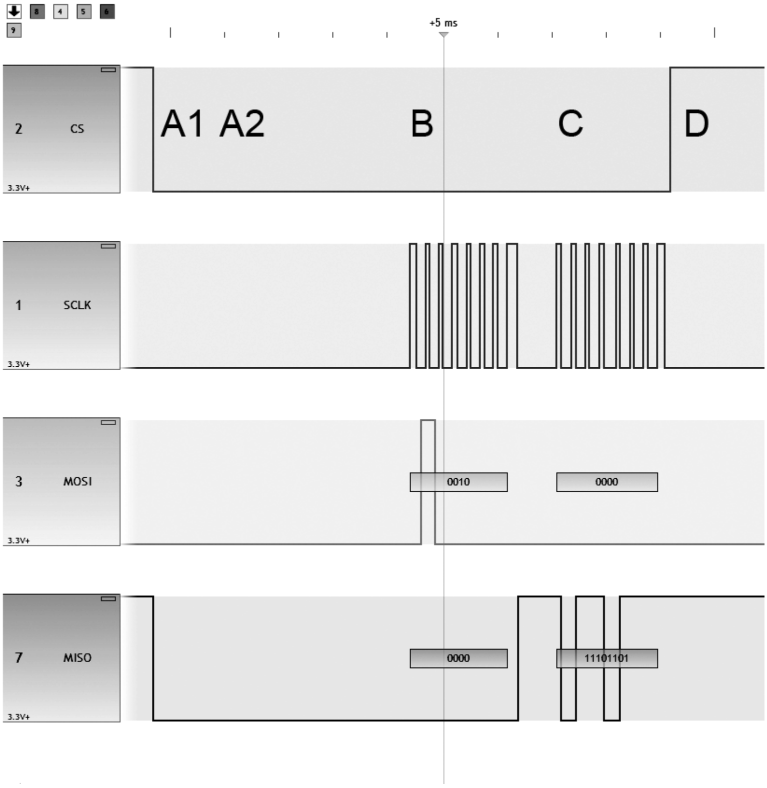

Figure 3.29: A typical SPI transaction between the OBC and FPGA with a 8-bit counter value.

OBC and FPGA, likewise.

However, it should be noted that in phase A for *all* transactions a delay of approx. 0.4 ms occurs. It is not quite clear as to why this happens but most likely due to some string operations which take place. Furthermore, in a number of cases a transmission is delayed due to other background tasks taking CPU runtime. This may cause delays up to 1 ms (data not shown).

A typical transaction requires approx. 900 ms with a SCLK clock speed of some 30-40 kHz if not interrupted. This speed is low compared to other SPI implementations but caused by the soft-SPI used by the Python OBC SPI master script. Overall, the function of the defined quasi-SPI protocol could be verified both by simulations and measurements.

Tools such as logic analysers or oscilloscopes have proven useful when debugging issues or verifying the proper operation of equipment.

Numerous other characterisation measurements were undertaken. These, however, would go beyond the scope of this document and are hence omitted.

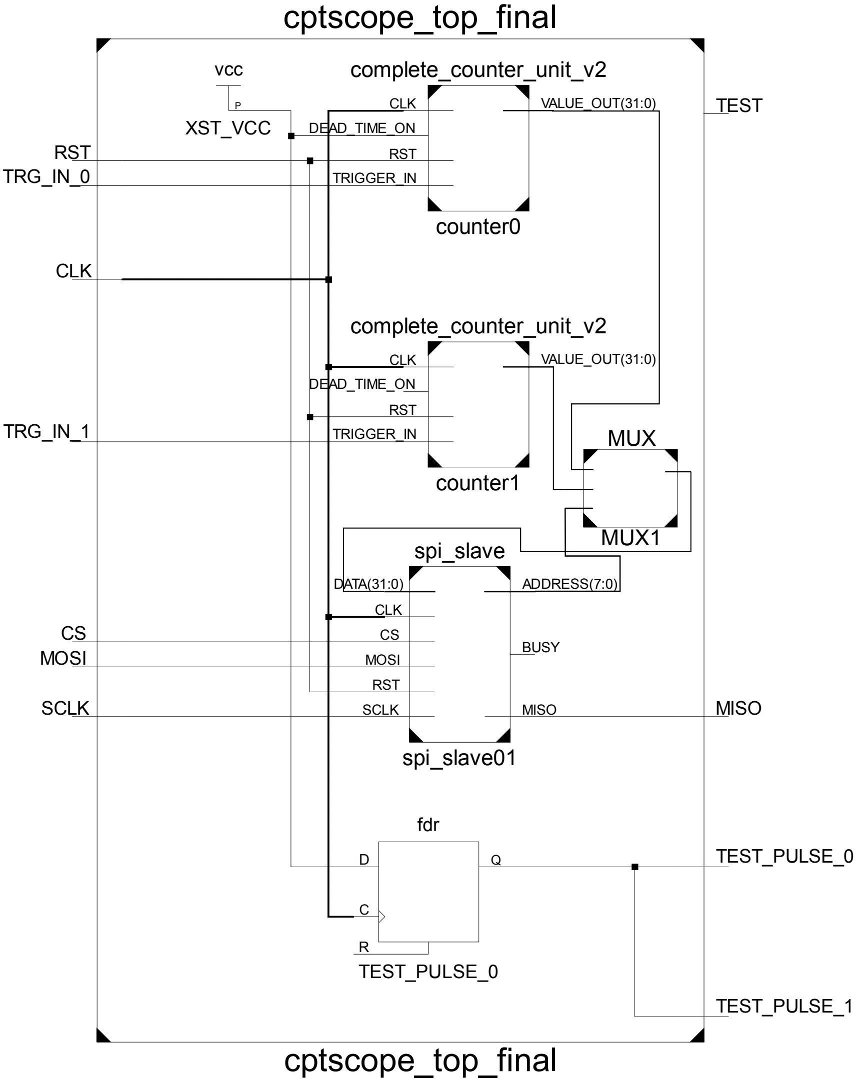

Figure 3.30: Detailed overview of the FPGA implementation and its main VHDL modules. See the text about module `cptscope_top_final` for more details.

Chapter 4

Testing the Device: Background and Radioactive Source Measurements

4.1 Measurements

Using the aforementioned hard- and software implementation the technology demonstrator became a functioning radiation monitor prototype. A selected number of these measurements, their results and implications will be presented in this section.

It is essential to understand that the main task of the present thesis work is the instrument development and not the scientific results of the following measurements. These only serve for testing and verification purposes that the initial goals have, indeed, been fulfilled.

The following measurements were done:

- Count rate R^{k} over source-detector distance d for Am-241,
- Threshold spectra of several sources i.e. R^{k} over DAC threshold value T_{thres},
- Time series data to study background and time variations i.e. R^{k} over time t with fixed DAC threshold values T_{thres}.

Before we begin the used radioactive sources will be explained.

Table 4.1: Suitable radioactive sources at IDEAS and their basic parameters.

ID	Isotope	Primary decay	Half life	Dated	Initial activity
1	Am-241	alpha, gamma	432.6 a	1993-10-19	111 MBq
2	Co-57	EC, gamma	271.8 d	2002-12-03	111 MBq
3	Sr-90	beta(-)	28.8 a	1992-12-11	3.7 kBq
4	Na-22	beta(+)	2.6 a	2003-10-01	37 MBq
5	Eu-152	beta, gamma	13.5 a	2015-04-20	37 kBq
6	Tl-204	beta(-)	3.79 a	2015-04-20	9.25 kBq

4.1.1 Radioactive Sources

Two source types were sought after: i) energetic particle emitters, ii) low-energetic gamma ray sources and iii) sources with sufficiently high activity A.

For gamma ray sources the acceptable energy range is well defined as shown in Fig. 3.16: for absorption efficiencies of higher than 10% the photon has to have an energy of 2 keV to 30 keV. For lower or higher energies the efficiency drops sharply.

For particle sources the restrictions are similarly defined by the used sensor: Due to the epoxy window on the FS X100-7 Si diode no alpha particles nor low-energetic X-rays or betas will be detectable. Hence only energetic beta emitters may be used. In addition, energetic cosmic ray secondaries, in particular muons, can be detected.

Table 4.2: Radioactive sources and their remaining activity. The assumed current data was 2015-05-10 ± 5 days.

ID	Isotope	Remaining activity	Current activity	Age
1	Am-241	96.6%	107 MBq	21.5 a
2	Co-57	0.001%	1.1 kBq	4528 d
3	Sr-90	58.2%	2.1 kBq	22.5 a
4	Na-22	4.54%	1.7 MBq	11.6 a
5	Eu-152	100%	37 kBq	0 a
6	Tl-204	100%	9.25 kBq	0 a

In addition, the source of radiation must deposit sufficient energy in the absorber material and reach the front-end electronics (keyword: total instrument efficiency). This depends also on the noise of the setup and its environment. Therefore it is difficult to make precise predictions to numerical values and, therefore, measurements are inevitable.

The sources presented in Tab. 4.1 were either available at IDEAS or purchased for this project[1], and fulfil the above criteria. Their expected current activity levels are calculated using Eq. (2.2) and are reported in Tab. 4.2.

There are two types of radioactive sources in use: i) pellet type - only allowing gamma rays to exit (stored in a brass / lead container) and ii) disc sources with a laminated window to

---

[1] The Eu-152 and Tl-204 sources were purchased from Spectrum Techniques ([58]) for CPT-SCOPE.

allow beta particles to exit. Sources 1, 2 and 4 are strong gamma source and manufactured as pellet type, while sources 3, 5 and 6 are laminated disks.

Radiation safety is an important aspect of laboratory work related to nuclear physics. A comprehensive guide is provided in [14]. For the following beta particle measurements only IAEA-exempt sources with low-activity were used for particles. Furthermore, beta sources are easily shielded with a thin metal sheet as described in chapter 2.

However, some of the used gamma ray sources were either with high activity (source 1 and 3) or emit high energetic gamma rays (source 2 and 4). In order to reduce exposure lead (Pb) and brass shielding was used. In terms of shielding for gamma sources a description is found in [44] and [14].

Table 4.3: Required Pb shielding length l_0 for various gamma ray energies E_γ for transmission ratio of 1% and 0.1%, source for μ-values: [44].

Energy / keV	$\mu^{(\mathrm{Pb})}$ / cm^{-1}	$l_0^{(1\%)}$ / cm	$l_0^{(0.1\%)}$ / cm
100	60.4	0.08	0.11
200	10.6	0.44	0.65
500	1.70	2.71	4.06
1000	0.77	5.98	8.97

The Tab. 4.3 summarises the required Pb shielding thickness to allow 1% and 0.1%, respectively, of gamma rays to be transmitted for energies of $E_\gamma = \{100, 200, 500, 1000\}$ keV. From the above it becomes clear that the Am-241 and Co-57 sources are easily shielded by a regular lead sheet. However, the more energetic Na-22 gamma rays are still penetrating in significant amounts the environment.

Care has to be taken when handling radioactive source. In general, the best strategy is to reduce the amount of time handling the sources (exposure) and use shielding as much as possible. A personal dosimeter has to be used when handling strong sources.

Before continuing with the actual measurement sets two sources will be excluded based on our previous analysis:

i) The Na-22 source (ID: 4) emits energetic gamma rays at 1.2 MeV due to the dominant β^+-decay mode [7]. The positron annihilates inside the source container and causes two additional gamma rays at 511 keV to be released. Both gamma ray energies are too high for the used Si diode and its efficiency is well below 1%. Only the Compton scattering background caused by the photopeaks will be visible and dominate. This has been verified by threshold scan measurements (data not shown). Furthermore, the source poses a health risk when only marginally shielded. Therefore no further experiments were carried out with this source since no knowledge gain about the instrument's performance can be expected.

ii) The Co-57 source (ID: 2) can easily be shielded since its main gamma lines, caused by an EC decay, are at energies $E_\gamma = 122$ and 136 keV [4]. This source would have been ideal at initial activity to obtain photopeaks or additional features in a threshold scan. However, due to its extremely low remaining activity of 1.1 kBq, combined with the low detector efficiency at gamma energies higher than 100 keV, not enough data could be obtained within an acceptable integration time. In test measurements no useful data could be obtained and hence further experiments with the Co-57 source were not conducted.

4.1.2 Count Rate over Distance

The dead timed this measurement was to verify the expected drop in count rate over distance d as predicted in Eq. (2.27) (for an isotropic source) and estimate the detector dead time after [36]. In this measurement the Am-241 source (ID:1) has been used. The pellet containing the radionuclide has been placed in a protective brass container which has been fixed onto a plastic sheet. The source is held in place using thin Kapton tape (not shown) and a hole has been cut into the plastic where the source is located. The distance to the detector is varied by changing four M3 spacers which are available in several lengths. In this way a multitude of distances, of the order of 1 cm, can be achieved. The source setup is shown in Fig. 4.1.

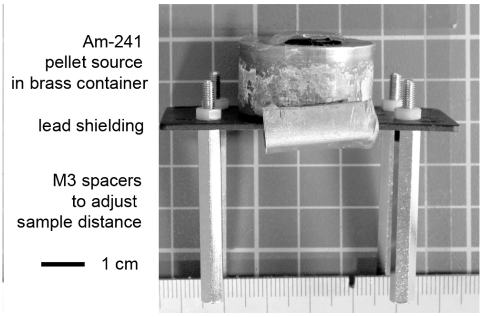

Figure 4.1: Am-241 source setup for count rate measurements over distance. The distance was varied using M3 spacers. All other components are labelled.

Aim of this measurement was to record the count rate R as function of distance d. A total of 24 distances were recorded in the range of 17 mm to 109 mm from the detector with an error of 0.5 mm. These were measured using a digital caliper. While mounting the spacers the lead shield was placed in front of the source. For measurements the sheet was removed.

The VATA465 input channel IN_01 and output trigger T_OUT01A was used in double gain mode and with the dead time counter being active. The threshold for T_OUT01A was $T_{thres} = 10$. This is based on threshold scan results presented below. For each data point a total of ten exposures were taken with each 10s integration time. Such low-integration time was possible due to the high activity of the source. The data was taken with a modified version of the script: `meas_fixedthreshold_timeseries.py`.

The average count rate R and its standard deviation ΔR have been calculated from the raw data. The measured values of R and d with their respective error are shown in Tab.

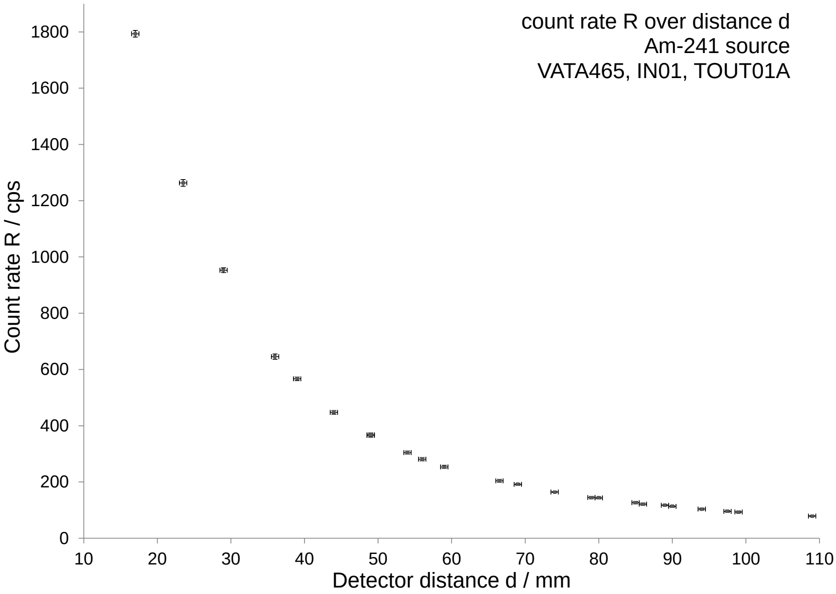

Figure 4.2: Graph showing measurement results for the Am-241 source count rate R (y-axis) over distance d (x-axis) with error bars.

5.1 (Appendix).

4.1.3 Time Series: Count rate over time

In this set of measurements the detector is recording the count rates $R^{(\mathrm{k})}$ for a fixed threshold $T^{(\mathrm{k})}_{thres.}$ and exposure time t_{exp}. This is done for N data points. A time stamp is saved for each point in order to analyse the resulting time series afterwards. Again the VATA465 input channel IN_01 was used. However, this time the count rates for triggers T_OUT01A (dead time counter: active) and T_OUT01B (dead time counter: deactivated) were recorded. Both use double gain mode since they share the same pre-amplifier.

For all time series measurements the following device settings were used: $t_{exp} = 10$ s, $T^{(\mathrm{TOUT01A})}_{thres.} = 30$ and $T^{(\mathrm{TOUT01B})}_{thres.} = 1$. In every run $N = 1000$ data points are obtained and stored. A measurement campaign is composed of several runs, typically 4-6. All data was taken using the measurement script: `meas_fixedthreshold_timeseries.py`. The instrument was located in the same place, the top-floor of a building in Northern Oslo, Norway.

Over the time period of April 29, and May 14, 2015, a total of 63,000 data points were acquired, corresponding to 175 hours of total exposure time. A typical time series graph is shown in Fig. 4.4.

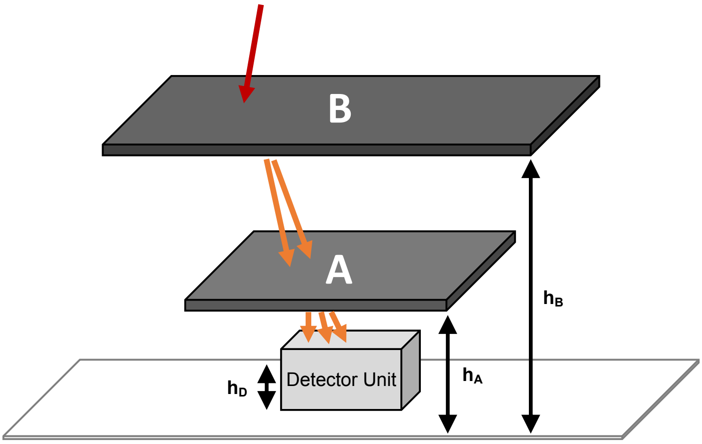

Figure 4.3: Time series measurement setup with Pb targets (A) and (B). The primary particle (red arrow) generates secondaries (orange arrows) which can be detected. The original trajectory of the primary would not have lead to a detection.

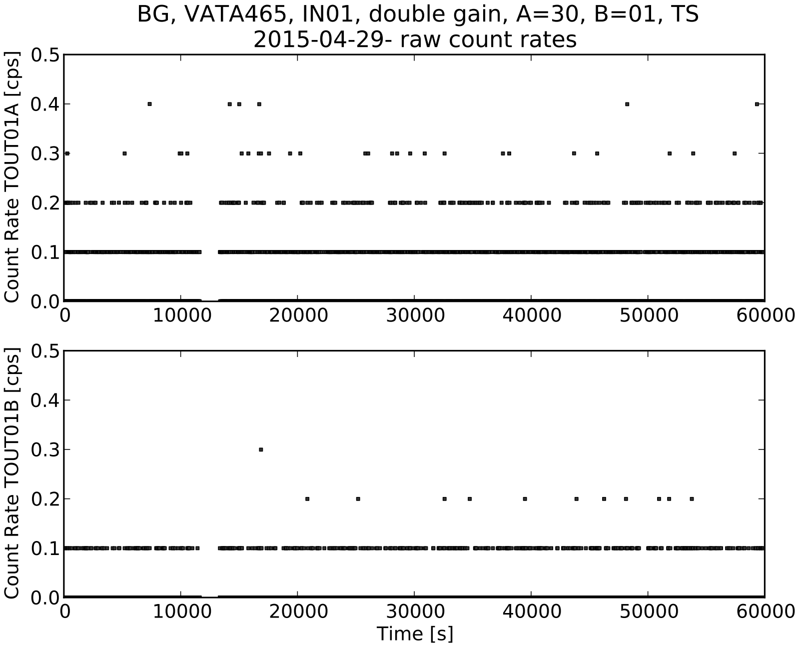

Figure 4.4: Time series for background data, taken on 2015-04-29 without Pb target.

In the figure the top graph shows the count rate R for trigger output T_OUT01A while the lower one shows R for T_OUT01B in units of counts per second (cps). The x-axis indicates the elapsed time since the beginning of the measurement (mid-point time). In the present example the measurement has a total of 6,000 data points. The campaign was started on 2015-04-29 at 15:26 UTC.

For such long measurement campaigns the email functionality of the data acquisition script has proven useful to keep track of the experiment status.

Besides regular measurements (no Pb target) where the detector unit is left inside the instrument box, three additional campaigns have been carried out with a modified geometry: i) For one set of measurements on 2015-05-01 a single Pb sheet (A) has been placed on top of the instrument box (height h_A) to serve as target for cosmic rays. In additional two campaigns two Pb sheets (A, B) have been placed with distances h_A and h_B from the instrument bottom surface (double target). This is shown in Fig. 4.3. The thickness of sheets A and B are 1.2 mm and 2.0 mm, respectively. The sheets have dimensions of 18 cm x 37 cm and 37 cm x 68.5 cm for A and B, respectively. The detected particles have to further pass through two layers of Al sheet, each approx. 1 mm thick, before being able to reach the detector which is located at height h_D = 3.5 cm in respect of the instrument box bottom. The relevant target heights are shown in Tab. 4.4. The sheets are kept in place by cardboard boxes which are negligible due to their low-Z value.

Table 4.4: Height information of targets A and B, as well as the detector.

ID	**Date**	**Target**	**h_D / cm**	**h_A / cm**	**h_B / cm**
10	2015-05-01	Single	3.5	11	N/A
11	2015-04-30	Double	3.5	11	30
12	2015-05-02	Double	3.5	11	41.5

The dead timed installing the Pb targets was to generate secondary particle showers (orange arrows) caused by a cosmic ray (red arrow). However, the number of counts should not be increased due to the larger number of ionising radiation in the shower, but due to the larger geometric acceptance of the instrument. This is shown by the fictional event in Fig. 4.3. In the sketch the primary particle would not have been detected since its trajectory does not pass through the detector. However, due to the shower caused by targets A and B, ionising particles may enter the detector.

Nevertheless, the main dead timed the time series data was to study the amount of detectable background radiation, their distribution over time and effect on the instrument. This is important in order to correct for background effects in more sensitive measurements. The expected main contribution should be originating from atmospheric secondary cosmic ray particles (mainly muons, ca. 4 GeV) [8]. These particles are so energetic that no trivial shielding technique can be used.

An overview over all time series campaigns, their parameters and selected results are summarised in Tab. 4.6 (Chapter Results). The individual time series graphs can be found in the Appendix and will be discussed later.

4.1.4 Threshold Scan Spectra

The motivation for trigger rate-based spectra is to verify the energy deposition of particle and gamma sources in the instrument, their characteristics and hence being able to distinguish them.

The DAC threshold value controls the minimum charge, and therefore energy, necessary to cause the firing of the trigger output.

Classically, the analogue pulse height histogram would be obtained and analysed as energy spectrum. By sweeping the DAC threshold value T and measuring the associated count rate $R(T)$ one obtains a cumulative spectrum. By taking the "derivative" of the data $R'(T)$ a course energy spectrum can be deduced.

This technique will be utilised for this set of measurements. For the data acquisition the `meas_threshold_scan.py` script has been used.

For the following radioisotopes data has been taken:

- Am-241,
- Sr-90,
- Eu-152 and
- Tl-204.

In addition, several background scans have been made. All samples are beta emitters with the exception of Am-241 which is used due to its low-energetic gamma rays at 59 keV [7] and high activity.

Table 4.5: Overview over threshold scan data sets and their parameter. These are (from left to right): i) ID, ii) date, iii) max. threshold value, iv) min. threshold value for TOUT01A, v) exposure time t_{exp} per data point and vi) number of data sets per campaign. Note BG stands for background and in the final analysis only threshold value ≤ 10 will be used.

ID	Sample	Date	T_A(max)	T_A(min)	t_{exp} / s	N_{scan}
1	Eu-152	2015-05-11	181	1	60	6
2	Tl-204	2015-05-12	181	1	60	5
3	Sr-90	2015-05-13	181	1	60	5
4	Am-241	2015-05-12	51	1	60	4
5	BG	2015-05-16	185	1	60	3

For all measurements the threshold T scan is carried out from the highest to the lowest value due to improved noise performance (less noise feedback). The minimum reliable count rate reading can be done at threshold $T = 10$ for trigger outputs T_OUT0xA due to a retriggering. Input IN_01 is used along with triggers T_OUT01A (dead time counter: on) and T_OUT01B (dead time counter: off). Both triggers are kept at the same threshold value and double gain mode is active. The integration time per data point was for all samples fixed to $t_{exp} = 60$ s. The raw sample count rates of trigger T_OUT01A are shown in the following figures: i) Eu-152: Fig. 4.5, ii) Tl-204: Fig. 4.6, iii) Sr-90: Fig. 4.7, iv) Am-241: Fig. 4.8, v) and for the background (BG): Fig. 4.9.

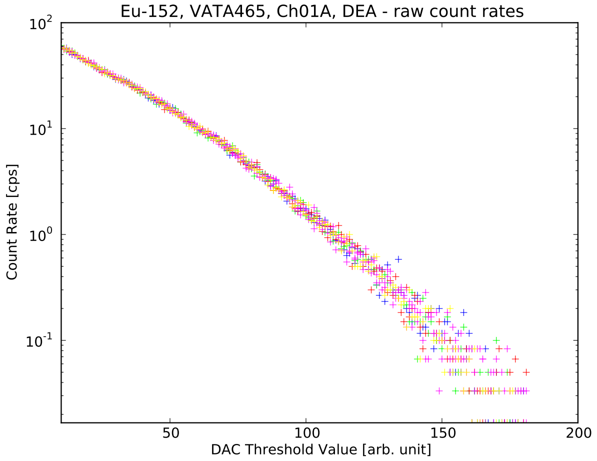

Figure 4.5: Raw count rates for individual threshold scan measurements of Eu-152.

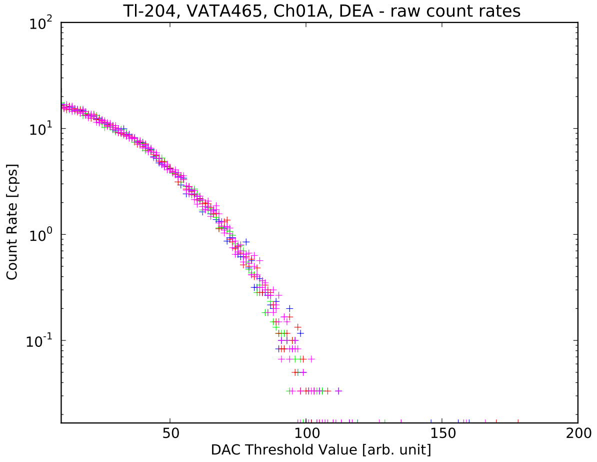

Figure 4.6: Raw count rates for individual threshold scan measurements of Tl-204.

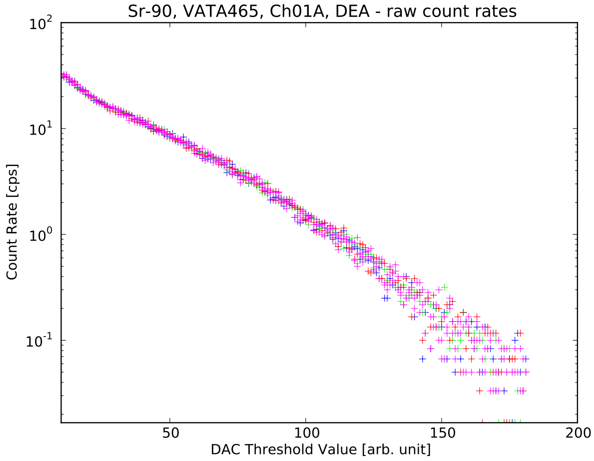

Figure 4.7: Raw count rates for individual threshold scan measurements of Sr-90.

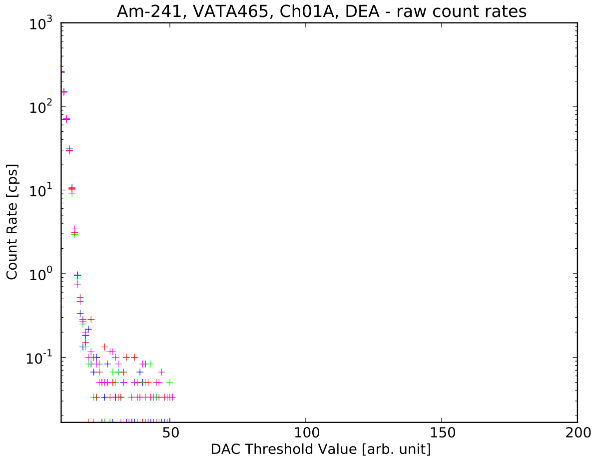

Figure 4.8: Raw count rates for individual threshold scan measurements of Am-241.

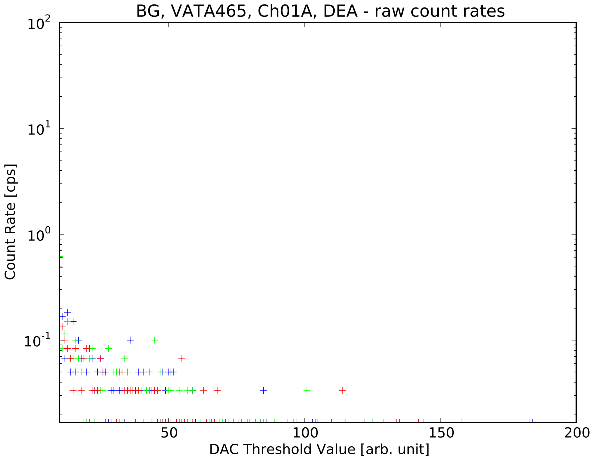

Figure 4.9: Raw count rates for individual threshold scans for background radiation.

4.2 Data Analysis and Results

In this section we will summarise the post-processing and results of the measurements described before.

4.2.1 Remarks on Data Processing

The post-processing is carried out using Python (v.2.7) and OriginPro 8. Python libraries `matplotlib`[2] and `numpy`[3] have been extensively utilised. Since the raw data is stored in a standard format of comma-separated values (CSV, data) and the header, clearly marked by hashtags (#), each file is easily read by both human and computer. In some cases using standard scientific spreadsheet programs such as Origin was sufficient for all practical purposes. We will now go into the details of the individual data analysis and their results.

4.2.2 Count Rate over Distance

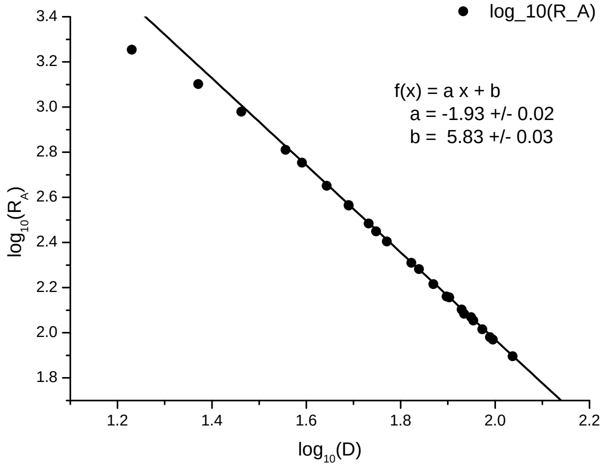

Figure 4.10: Fitting of parameters for rate measurements over distance.

The measurement of count rate R_A as function of distance d for Am-241 (shown in Fig. 4.2) can help to estimate various instrument parameters, namely the instrument efficiency η for gamma rays at 59 keV [7] and to first-order estimate the detector dead time τ [36].

---

[2] Python library `matplotlib`: `http://matplotlib.org/`.

[3] Python library `numpy`: `http://www.numpy.org/`.

First we try to model the count rate R_A as function of the distance d. In a coarse approach we neglect the interaction of gamma rays in air and geometric factors. One can then expect a decrease of R_A over d^{-2} as described in chapter 2. In order to test these assumptions one can plot the measured R_A in a double-logarithmic graph and fit a linear function to it. Mathematically, the simplified model for the count rate R is expressed as:

$$R(d) = R_0 \cdot d^a. \tag{4.1}$$

Where R_0 is the source activity, d the distance and a the model exponent. We take the common logarithm (base 10) and rewrite Eq. (4.1) as:

$$\log\left(R(d)\right) = a \cdot \log\left(d\right) + b \quad \mathrm{with\ b = \log\left(R_0\right)}. \tag{4.2}$$

This equation may be fitted to a linear expression ($f(x) = a\,x + b$) with parameters a and b.

When inspecting the double logarithmic plot in Fig. 4.10 one realises that only for large values of x (=log (d)) a proper linear relation is followed. The closer the detector gets to the source the less the count rate R_A increases.

This is due to a phenomenon called dead time which will be discussed later. At the present stage it is only relevant that the linear fit should contain data points that have a large distance $d >$ 55 mm (log(55)=1.74). The above value was determined by visual inspection. In that distance range the measured (R_A) and real count rate R_S are identical in the great majority of cases (dead time effects are neglible).

Using the Origin built-in linear regression the following parameters[4] were found:

$$a = (-1.93 \pm 0.03)$$

and

$$b = (5.83 \pm 0.03).$$

The fit of the model is good as indicated by the grey line in Fig. 4.10. From these model parameter we can deduce a number of results:

- i) The measured source activity is $R_0 = 10^b \approx 630$ kcps according to Eq. (4.2). We can compare this number to its expected value for the Am-241 source and its geometry. By doing so one can determine the instrument's overall efficiency η for gamma rays at 59 keV.
- ii) The measured exponent $a = -1.93$ is close to the expected value of -2. In fact it is within 3 sigma from the expected exponent and its offset may be caused by systematic errors such as not considering the details of the source and detector geometry.

---

[4] For clarity the physical units of b, namely log (s), are omitted.

4.2.2.1 Detector efficiency estimation

We will now estimate the detector efficiency η for 59 keV gamma rays. The extrapolated value for b has been 5.83 which leads to a expected instrument count rate of ca. 630 kcps for the source. As indicated in Tab. 4.2, the expected remaining activity of the actual Am-241 source should be $A_0 = 107$ MBq. The detected number of events is well below one percent, when not accounting for geometric effects and interaction along the path.

However, at least the radiation source and instrument geometry must be considered. We will make estimates to obtain a lower limit for the instrument efficiency. First the above source activity is emitted uniformly in all directions. However, only event can be detected which are emitted trough the opening towards the detector. We will overestimate this portion being the entire hemisphere i.e. half of the radiation is detectable by the instrument. We introduce the geometric efficiency $G = 0.5$. Furthermore, for Am-241 in only P_γ =35.9% of disintegrations a 59 keV gamma ray is emitted [7]. However, with the used settings only the 59 keV line of Am-241 can be detected (see threshold scan results below). This need to be accounted for as well.

From this we obtain the following instrument efficiency η for the Am-241 source: $\eta = R_0/(P_\gamma \cdot G \cdot A_0)$. This leads to a value of

$$\eta(59\ \text{keV}) = 3.3\%.$$

Such value is in agreement with the expected gamma absorption probability of the FS X100-7 Si detector [1] which is approx. 3% (cf. Fig. 3.16). This means that most detected events are transferred and registered by the instrument. Hence the overall instrument efficiency for these low-energetic gamma rays is dominated by the detector response. Indeed, for the VATA465 the efficiency is excellent ($> 99\%$) for test pulses injected into the inputs as shown in [46, 54]. This is in agreement with the above findings. However, it should be noted that the efficiency measurement requires further investigation as for the low threshold value used, namely $T = 10$, noise triggers can be substantial. Such systematic error source may reduce the true instrument efficiency.

4.2.2.2 Detector deadtime estimation

Lastly, we will make a rough estimate of the detector dead time. For this we inspect Fig. 4.10. A diversion from the model fit is increasingly visible starting at count rates R_A of the order of 1,000 cps. At that point the incident particles create pile-up at the VATA pre-amplifier which causes dead time effects i.e. the missing detection of true events. In a rough estimate we can deduce that the dead time τ is on the order of several 100 μs which is in agreement with the expected value for the VATA465 pre-amplifier[5]. A more elaborate evaluation of the dead time can be carried out for a paralyzable system, such as the VATA465, as outlined in chapter 17 of [36].

---

[5] Personal communications with D. Meier, May 2015.

4.2.3 Time Series

The time series measurements have been covering a total of 175 hours in exposure time. This allows for a careful study of background events in particular the ones caused by cosmic rays at sea level. The different measurement campaigns and their parameters are summarised in Tab. 4.6.

From visual inspection of the time series graphs we find no significant difference between the individual time series campaign data as shown in Figs. 5.1 - 5.12. Furthermore, we cannot identify a clear difference between data campaigns studying the effect of no, single or double Pb target(s). This is somewhat unexpected since the acceptance of the instrument has been increased by placing the lead sheets above.

Table 4.6: Overview about time series measurements. The table contains the following information (left-to-right):
i) ID - campaign identifier, ii) the date (2015-MM-DD), iii) threshold for TOUT01A, iv) threshold for TOUT01B, v) exposure time in sec., vi) number of points (k = 1,000), vii) Pb target information, viii) TOUT01A count rate R_A / cps, ix) standard deviation of R_A / cps, x) TOUT01B count rate R_B and xi) R_B standard deviation / cps.

ID i	**Date**	T_A	T_B	t_{exp}	N	**Target**	$R_A^{(i)}$	$\sigma(R_A^{(i))}$	$R_B^{(i)}$	$\sigma(R_B^{(i)})$
1	04-29	30	1	10	5k	None	0.0351	0.0602	0.0083	0.0286
2	05-03	30	1	10	6k	None	0.0357	0.0608	0.0082	0.0286
3	05-05	30	1	10	6k	None	0.0347	0.0585	0.0074	0.0274
4	05-06	30	1	10	1k	None	0.0358	0.0608	0.0076	0.0279
5	05-06	30	1	10	6k	None	0.0342	0.0586	0.0077	0.0278
6	05-07	30	1	10	7k	None	0.0351	0.0591	0.0080	0.0282
7	05-08	30	1	10	6k	None	0.0353	0.0590	0.0085	0.0290
8	05-14	30	1	10	5k	None	0.0358	0.0590	0.0072	0.0263
9	05-15	30	1	10	3k	None	0.0364	0.0602	0.0079	0.0278
10	05-01	30	1	10	6k	Single	0.0338	0.0594	0.0069	0.0265
11	04-30	30	1	10	6k	Double	0.0354	0.0592	0.0086	0.0291
12	05-02	30	1	10	6k	Double	0.0341	0.0589	0.0076	0.0276

We will now study the presented data numerically. For each campaign the average count rate for triggers T_OUT01A and T_OUT01B has been calculated. These are labelled $R_A^{(i)}$ and $R_B^{(i)}$, respectively. In this case i refers to the campaign ID. Furthermore, the sample standard deviation has been calculated for each campaign and channel as well, labelled $\sigma(R_A^{(i)})$ and $\sigma(R_B^{(i)})$. Their numerical values are also included in Tab. 4.6.

We can see that the campaign standard deviations, $\sigma(R_A^{(i)})$ and $\sigma(R_B^{(i)})$, have similar values for each channel regardless of type of measurement (target or none). We will not include their values in further discussions since it is also difficult to give these values a concrete and relevant physical meaning.

In the next step we will study the total average count rate for the two channels, namely R_A and R_B. Note that the identifier i is now removed. The will lead us to the flux of energetic background particles for each channel, F_A and F_B. From the aforementioned visual inspection we came to the conclusion that no difference is visible in the time series graphs between the case of a target or none. However, the numerical analysis may reveal differences. Therefore only the campaign values will be considered which have no target in front of the detector i.e. IDs 1-9. These reflect a total of 45,000 data points corresponding to 125 hours of integration time (71% of all data).

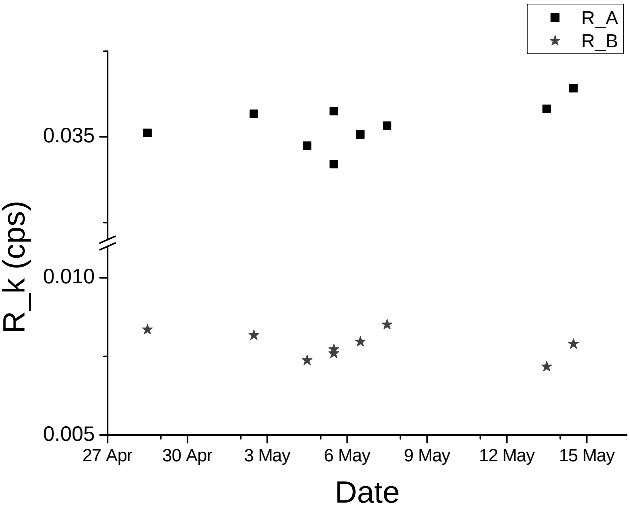

Figure 4.11: Change of counting rates R_k over time.

When looking at the time evolution of the average count rates $R_A^{(i)}$ and $R_B^{(i)}$ for measurements without target (ID 1-9) only a small variation can be observed as shown in Fig. 4.11. This indicates that no local source or time-varying source is causing the dominant portion of the measured background. The best explanation for this are cosmic rays which are fairly constant in their flux, at least at the resolution and time scale at hand. Here the average trigger rate of TOUT01A (squares) and TOUT01B (stars) follow each other closely. While not being statistically significant it may indicate that both parameters are coupled. This would be expected since cosmic rays are mainly energetic muons. These can deposit enough energy to trigger both output comparators. However, only in a little less than a third of detected events the TOUT01B output triggers. The correlation between triggers TOUT01A and TOUT01B has been investigated (data not shown). However, no significant conclusion were possible to be drawn.

Based on the individual count rate R_k a weighted average is calculated with weight w_i. In this case we use the number of data points as weight. The total count rate R_k is then evaluated by the following equation:

$$R_k = \frac{\sum_i \left(w_i \cdot R_k^{(i)} \right)}{\sum_i w_i}. \tag{4.3}$$

In this case indicates k the respective channel. In addition to the average we also want to compute the weighted standard deviation[6] of the sample σ_k. Its square value is described by:

$$\sigma_k^2 = \frac{\sum_{i=1}^{M} w_i \left(R_k^{(i)} - R_k \right)^2}{\left(\frac{M-1}{M}\right) \cdot \sum_{i=1}^{M} w_i}. \tag{4.4}$$

Here the number of non-zero weights is $M = 9$. The value of σ_k is the positive square-root of expression Eq. (4.4).

4.2.3.1 Cosmic ray background and time evolution

We find for the time series campaigns ID1-9 the following results for the total count rate and their standard deviation indicated as error behind the (+/-) symbol:

$$R_A = (0.0352 \pm 0.0006)\ \mathrm{cps}$$

and

$$R_B = (0.0079 \pm 0.0005)\ \mathrm{cps}.$$

These values are important when measuring weak sources as done in the threshold scans. In order to obtain a good signal to noise ratio (S/N) the sample should cause a significantly stronger count rate than the background.

Since we know the instrument geometry well we can convert these instrument count rates to flux values F_A and F_B:

$$F_A = (2.112 \pm 0.036)\,\mathrm{cm}^{-2}\,\mathrm{min}^{-1}$$

and

$$F_B = (0.474 \pm 0.030)\,\mathrm{cm}^{-2}\,\mathrm{min}^{-1}.$$

Here we have used the fact that the detector surface is 1 cm^2. This is quite a remarkable result. The flux of background particles is on the order of 1 particle per minute and cm^2. This value is compatible with the same literature value f.i. in [8]. When assuming that the detector is sensitive to all particles entering from the upper hemisphere its solid angle Ω can be estimated with $\Omega \approx 2\pi$. Under this assumption we can estimate the flux per solid angle, I_A and I_B with $I_k = (F_k/\Omega)$. We obtain the following values after converting to appropriate units:

$$I_A = (56.0 \pm 1.0)\,\mathrm{m}^{-2}\,\mathrm{s}^{-1}\,\mathrm{sr}^{-1}$$

and

$$I_B = (12.5 \pm 0.9)\,\mathrm{m}^{-2}\,\mathrm{s}^{-1}\,\mathrm{sr}^{-1}.$$

We can go further and compare the value of I_k to more specific literature values given in ”Cosmic Ray Fluxes” (section 26 in [8]). Beringer *et al.* (2012) report the following expected flux values per steradian (sr) for the vertical direction:

---

[6] Weighted standard deviation reference:
`http://www.itl.nist.gov/div898/software/dataplot/refman2/ch2/weightsd.pdf`.

Total I	**Hard component ($\mu^{\pm}$)**	**Soft component ($e^{\pm}$)**	**Unit**
110	80	30	$\mathrm{m}^{-2}\ \mathrm{s}^{-1}\ \mathrm{sr}^{-1}$

Our values are below the reported once above. Nevertheless, it is likely that the absolute flux I is larger due to losses and wrong estimates of the experiment's solid angle and acceptance. A detailed guide for the calculation of a particle detector acceptance etc. can be found in [57]. The above table also shows the flux values for the hard i.e. energetic muons and soft component (electrons and positrons). From our value we can establish the opinion that our device is not only susceptible to the soft but to the hard component as well.

Furthermore, the finding that $F_A > F_B$ is also no surprise. With the present threshold settings of $T_{thres.}^{(\mathrm{TOUT01A})} = 30$ and $T_{thres.}^{(\mathrm{TOUT01B})} = 1$ the B-trigger requires a higher deposited energy. At higher energies the particle flux decreases [8]. It would be interesting to carry out time series measurements for various threshold and reconstruct the spectrum of the background sources. This may be compared to conventional pulse height spectroscopy with the same device. With this we will conclude the discussion of the background particle flux for measurements done without target.

For measurement sets with targets (ID 10-12) we find that the numerical value of the count rates $R_k^{(i)}$ is lowest for the single target (ID 10), while the double target sets are similar to measurements done without any Pb sheets. Due to the small number of measurements it remains speculative but this may indicate that in the geometry of the single target a net-reduction occurs due to the present lead. This is unlikely true for energetic cosmic rays. However, the soft component such as electrons may be stopped. For the double configuration this effect may be compensated for by the larger acceptance of the instrument due to the larger Pb sheet (B) being placed on top. More measurements in varying instrument geometries are necessary to shed a light on this.

In conclusion for the time series data one can find that: i) the measured background data is consistent with literature values for cosmic rays at sea level and ii) that their contribution to other measurements done with the current setup is better understood and hence can be accounted for.

4.2.4 Threshold Spectra

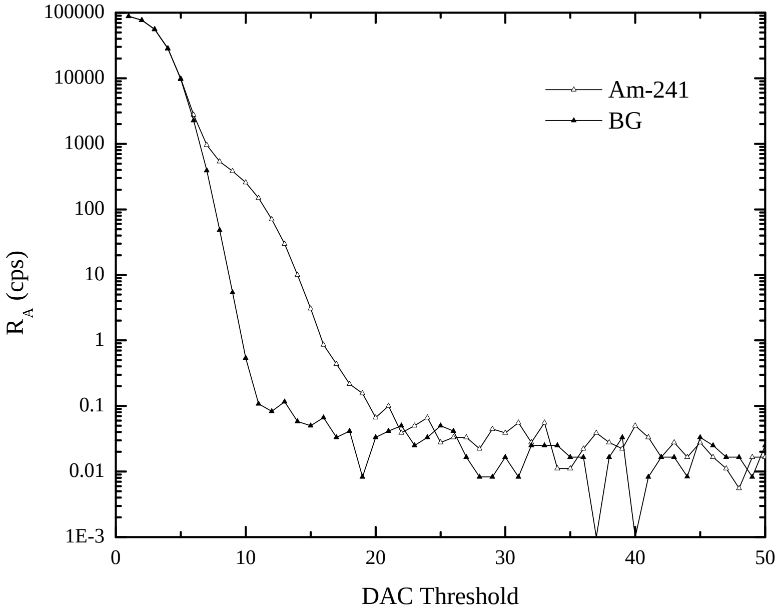

Figure 4.12: Count rates of Am-241 and background (BG) over DAC threshold values T. Besides the noise peak for low threshold values (T<10) a clear contribution of the Am-241 sample is visible.

In this section we will present the findings for the threshold scan spectra of various sources. Its aim is to verify that the goal of being able to detect energetic particles and low-energetic gamma rays has been fulfilled.

The raw count rates R have been shown for all sources already in the measurement section in Figs. 4.5 - 4.9.

For the data analysis a Python script has been written which reads in all data sets for a given source. If more than one count rate value is available the largest count rate value is excluded for further processing. By introducing this step contamination from background events (cosmic rays) were effectively mitigated. This strategy has proven reliable in particular for readings at high thresholds due to the reduced count rate. For typical data sets with 3-6 measurements with 60 s exposure time (t_{exp}) per data point, removing one sample is sufficient. If the number of samples taken with fixed t_{exp} is increased, more values must be excluded accordingly. The above value has been deducted experimentally and conforms with the results of the time series data.

The remaining raw count rates for trigger output T_OUT01A are averaged and their standard deviation calculated. The latter serves as error estimate. These numbers are exported from the Python script and entered into a spread sheet in Origin for further processing.

The nature of the observed radionuclides will now be summarised listing the most relevant information to interpret the experimental data:

Sr-90 -
- beta (-) decay into Y-90 (unstable, beta(-)):
max.: 545.9 keV, avg.: 196.0 keV (100 / 100 disint.)
Source: [6, 11].

Eu-152 -
- beta (-) decay to Gd-152 (long half life: 10^{14} a) (27.9%):
max.: 695.6 keV, avg.: 221.7 keV, (13.8 / 100 disintegrations)
max.: 1474.5 keV, avg.: 535.4 keV, (8.2 / 100 disintegrations.)
- EC decay to Sm-152 (observationally stable) (72.1%):
several high-energetic gamma rays (E_γ =>120 keV)
Source: [5].

Tl-204 -
-beta (-) decay into Pb-204 (observationally stable):
max.: 763.7 keV, avg.: 243.9 keV, (97.1 / 100 disintegrations.)
Source: [5].

Am-241 -
- alpha decay into Np-237 (long half life: 10^6 a, alpha):
alphas not detectable, secondary gammas
(dominant line at $E_\gamma = $ 59.54 keV (35.9 / 100 disintegrations))
Source: [7].

The aforementioned references contain detailed decay schemes, probabilities and other useful information in regard to the individual radionuclides.

From the VATA465 validation report [46] the following empirical relation between the trigger threshold value T for outputs T_OUTxA in double gain mode and critical charge Q_c (see [54]) has been measured:

$$Q_c(T) = (0.1521 \cdot T)\,\mathrm{fC} + 0.1855\,\mathrm{fC}. \tag{4.5}$$

Here the critical charge Q_c correspondents to the necessary injected charge into the ASIC input to fire the trigger at threshold T for aforementioned settings. From the introduction section we recall that in order to create an electron hole pair in Si 3.6 eV are necessary [52] and that the following conversion can be done between number of electrons and fC:

$$1\,\mathrm{fC} \quad \Leftrightarrow \quad 6241\,\mathrm{e}^-.$$

We can use this information to gain insights into the presented data.

4.2.4.1 Spectrum of Am-241 and gamma photopeak

Figure 4.12 shows the averaged threshold scan (count rate R over threshold T, hereafter referred to RT-scan). Note that the y-axis is logarithmic showing the wide dynamic range of the measurement. The background spectrum is dominate by the noise and retriggering of the front-end electronics for very low threshold values of $T < 10$. The background then falls off sharply to values of 0.1 cps or less. However, the Am-241 data shows an excess in the threshold range of $T = 10$ and 20. For these threshold values the BG count rate is overcome by at least 2 orders of magnitude. When applying Eq. (4.5) for a central value of $T_c = 13$ we obtain an input charge of $Q_c = 2.2$ fC. This charge can be converted to a minimum required energy to release this number of electrons, which evaluates to approx. 50 keV. This value is close to the expected, dominant Am-241 gamma line at 59.54 keV (corresponding to $T = 16$).

We therefore identify the described feature as the signature of the 59 keV Am-241 line. Due to its close proximity to the noise peak it is impossible to analyse the peak further. However, by the above observation one of the master thesis's main goals, of detecting low-energetic gamma rays, has likely been achieved.

Furthermore the equivalent noise charge (ENC) of the instrument can be estimated for the TOUT01A output to be equal of 1.7 fC or 10,650 electrons (for $T_N = 10$). These values are higher than the bare VATA465 fast shaper ENC values (ENC = 1,200 in single gain mode[7], [41]). However, this is expected since the detector and other external components contribute to the overall noise figure.

4.2.4.2 Spectra of beta emitters

For all beta sources the respective averaged count rates R_A are shown in Fig. 4.13 (indicated by the sample name). The figure shows the count rate R_A over the DAC threshold T in a logarithmic scale (error bars note shown). Even after averaging the count rate graph is not entirely smooth, in particular for large thresholds where noise dominates (right).

In order to reduce noise further the data is smoothed using a Savitzky-Golay (S-G) filter [48, 50] of order 4 and window size[8] 12. While reducing the high-frequency noise component the slowly changing actual data remains intact [48]. The method's positive effect on the data is evident in Fig. 4.13.

The obtained smoothed count rates are shown again in Fig. 4.14. The smoothed background curve (BG) is also included (bottom). When compared to at DAC threshold values of ca. 20 the graphs show the following samples (top to bottom): Eu-152, Sr-90, Tl-204 and BG. It is evident that all samples have count rates 2-3 orders higher than the background. Furthermore, the graphs of the various sources differs greatly among each other.

---

[7] The ENC figure should double for the used double gain mode: ENC = 2,400; personal communications with D. Meier, May 2015.)

[8] This means that a fourth order polynomial is fitted to a running window containing 12 data points at the time.

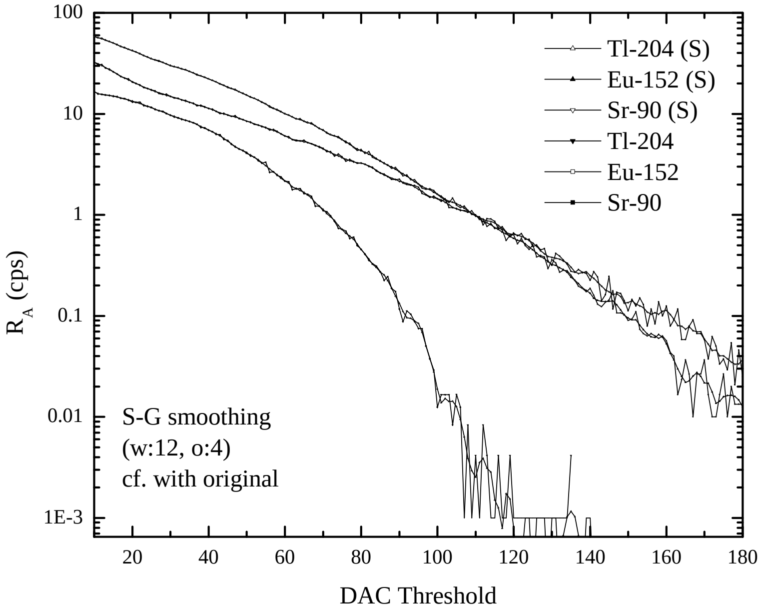

Figure 4.13: The graph shows the effect of (S-G) filtering on the averaged count rate curves of various beta emitters. The graphs show the following samples: Eu-152 (top), Sr-90 (middle) and Tl-204 (bottom) when compared at DAC threshold 20 (left).

From this we can draw two conclusions: i) the device is able to detect energetic beta particles (one of the main goal); and ii) they exhibit different characteristics and can hence be further studied using RT-scans.

Tl-204 sample:

We find that the Tl-204 sample RT-scan quickly falls off and drops to BG-levels around $T_c = 120$. Using Eq. (4.5) we can obtain a signal charge of $Q_c = 18.4$ fC which translates to about 413 keV as minimum deposited energy into the detector.

The maximum possible energy for a Tl-204 beta particle is 763.7 keV. The measured value is well below but of the same order of magnitude. Furthermore, the beta has interacted with matter along its trajectory, namely air and the epoxy layer, before being absorbed in the detector's active layer. This can account for the observed energy losses.

Tl-204 is a particular nice sample since it only undergoes a single, well known beta(-) decay into the ground state of its daughter nuclide, Pb-204 which is stable. Hence no gamma rays are emitted in the process ("pure beta emitter", [36]).

Eu-152 sample:

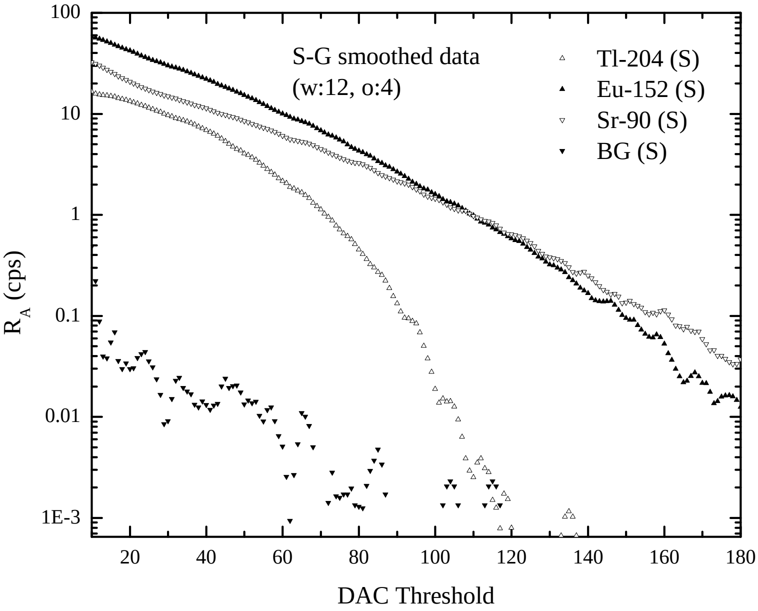

Figure 4.14: (S-G) smoothed count rate curves of various beta emitters: Eu-152 (top), Sr-90 (middle) and Tl-204 (bottom) when compared at DAC threshold 20 (left). At the very bottom the background spectrum is presented.

In the case of Eu-152 the decay process is more complex. In most cases it undergoes electron capture (EC) which causes high energetic gamma rays. From previous discussions it is evident that these will not be detectable with the present setup and can be neglected. However in 28% of cases two different beta(-) decays to Gd-152 can occur. The dominant one having similar energies to the Tl-204 decay, and a higher energetic one with a maximum energy of 1,475 keV. The later decay channel will produce a signature in RT-scans which should go far beyond the Tl-204 cut-off threshold. Indeed, in the entire range of thresholds the signal drops off, but never reaches BG-levels. With the present data at hand the best estimate for the cut-off threshold is $T_c \approx 230$. This correspondents to $Q_c = 35.2$ fC which translates to about 790 keV. Also this value has the right order of magnitude. The more complex decay scheme and losses along the beta's trajectory should account for the difference in deposited energy. However, new measurements are necessary to confirm the above extrapolated cut-off value.

Sr-90 sample:

In the last example we will use Sr-90 a pure beta(-) emitter similar to Tl-204. In this way the above hypothesis, that the RT-scan graph follows the expected cut-off energy of the beta particle, can be tested.

Sr-90 decays into Y-90 by emitting a beta(-) particle with cut-off energy of 546 keV, which is less than the maximum energy of the Tl-204 decay. Therefore one should expect that the cut-off threshold T_c for Sr-90 should be below the value for Tl-204 ($T_c = 120$).

However, when looking at Fig. 4.14 one finds that this is not true. In fact, Sr-90 maintains a significant count rate even for threshold larger than 120. Its slope is lower than of the Eu-152 sample. Is our theory wrong?

Luckily, this observation is easily explained by the Sr-90 daughter nuclide Y-90. It is a short-lived radionuclide with 2.6 days half-live (cf. 28.8 a for Sr-90) and decays via a beta(-) channel [6] to a stable Zr-90 nuclide. The beta particles have an average and maximum energy of 2278.7 keV and 926.7 keV, respectively. Thereby, overtaking even the energetic Eu-152 beta(-) decay. The expected released charge at maximum energy is ca. 100 fC which is about three times the saturation charge for the lower window high-gain comparator in double mode (TOUT0xA). In order to study this sample properly the upper window comparator TOUTxB should be used instead.

This is an important finding towards the CPT-SCOPE instrument which will study energetic particle precipitation in the stratosphere.

Lastly, it was attempted to obtain energy spectra from RT-scans. This was done by taking a numerical derivative off the averaged and (S-G) smoothed data for the beta(-) source scans. The result is shown in Fig. 4.15. These graphs show the derivative of the sampled RT-scans with a reversed, linear scale. The three samples have different graphs, both in amplitude and form.

The small scale variations are due to variations in the original data set caused by noise, even after (S-G) filtering. The overall shape appears continuous as expected for a beta source. No line features or similar are visible. The Tl-204 curve drops to background levels first around $T = 100$, followed by the Sr-90 and Eu-152 samples ($T \approx 120$). The exact shape and implications need to be studied further using more data points in order to reduce noise. Preferred to sources of continues energy particles (cf. beta) are mono-energetic one such as generated in particle accelerators. However, access to such facilities is limited and would be beyond the scope of this work.

4.2.5 Summary of Measurement Results

The instrument is functioning and can be operated remotely.

The discussed study of the beta(-) emitters confirms the instrument's capability to detect and characterise energetic particles.

While the detection of the Am-241 59 keV photopeak furthers validates the capability to detect low-energetic gamma rays as well.

The measured flux of cosmic rays on sea level agrees with literature values. Therefore sensitivity for energetic muons can also be assumed.

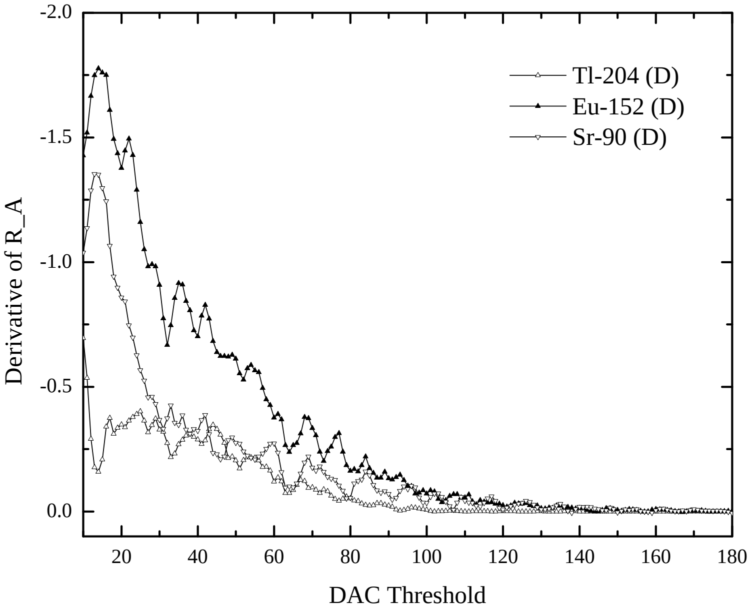

Figure 4.15: Derivative of the (S-G) filtered count rates for various beta emitters. The graphs show the following samples Eu-152 (top), Sr-90 (middle) and Tl-204 (bottom) when compared at DAC threshold 20 (left). Note that the y-axis is linear and reverse.

The noise figure, efficiency and dead time of the system were estimated providing valuable insights into the radiation monitor's performance.

Chapter 5

Conclusion

A functioning radiation monitor prototype has been developed, implemented and tested. First measurements of cosmic ray background, beta particle and low-energetic gamma ray sources verify its functionality.

This marks a major milestone towards a compact radiation monitor for nanosatellites. While this work deals with a technology demonstrator, it directly contributes to the CPT-SCOPE project.

The finished CPT-SCOPE instrument and its flight aboard BEXUS 20 in October 2015 will be the next milestone. In the future this should lead towards CPT-SCOPE 2.0, a CubeSat-ready compact radiation monitor.

The project demonstrated the usability of COTS components in hybrid with specialised, radiation-hard integrated circuits for radiation detection. This approach allows for rapid and inexpensive developments for small satellite and CubeSat instrumentation.

Bibliography

[1] F. S. AG. First Sensor PIN PD Data Sheet (X100-7 THD). Technical report, First Sensor AG, 2013. URL `http://www.first-sensor.com/cms/upload/datasheets/X100-7_THD_501400.pdf`.

[2] J. Als-Nielsen and D. McMorrow. *Elements of Modern X-ray Physics*. John Wiley & Sons, second edition, 2011. ISBN 978-0-470-97394-3.

[3] D. Baker, S. Kanekal, V. Hoxie, S. Batiste, M. Bolton, X. Li, S. Elkington, S. Monk, R. Reukauf, S. Steg, J. Westfall, C. Belting, B. Bolton, D. Braun, B. Cervelli, K. Hubbell, M. Kien, S. Knappmiller, S. Wade, B. Lamprecht, K. Stevens, J. Wallace, A. Yehle, H. Spence, and R. Friedel. The Relativistic Electron-Proton Telescope (REPT) Instrument on Board the Radiation Belt Storm Probes (RBSP) Spacecraft: Characterization of Earths Radiation Belt High-Energy Particle Populations. In N. Fox and J. Burch, editors, *The Van Allen Probes Mission*, pages 337–381. Springer US, 2014. ISBN 978-1-4899-7432-7. doi: 10.1007/978-1-4899-7433-4_11. URL `http://dx.doi.org/10.1007/978-1-4899-7433-4_11`.

[4] M.-M. Bé, V. Chisté, C. Dulieu, E. Browne, V. Chechev, N. Kuzmenko, R. Helmer, A. Nichols, E. Schönfeld, and R. Dersch. *Table of Radionuclides*, volume 1 of *Monographie BIPM-5*. Bureau International des Poids et Mesures, Pavillon de Breteuil, F-92310 Sèvres, France, 2004. ISBN 92-822-2206-3. URL `http://www.bipm.org/utils/common/pdf/monographieRI/Monographie_BIPM-5_Tables_Vol1.pdf`.

[5] M.-M. Bé, V. Chisté, C. Dulieu, E. Browne, V. Chechev, N. Kuzmenko, R. Helmer, A. Nichols, E. Schönfeld, and R. Dersch. *Table of Radionuclides*, volume 2 of *Monographie BIPM-5*. Bureau International des Poids et Mesures, Pavillon de Breteuil, F-92310 Sèvres, France, 2004. ISBN 92-822-2207-1. URL `http://www.bipm.org/utils/common/pdf/monographieRI/Monographie_BIPM-5_Tables_Vol2.pdf`.

[6] M.-M. Bé, V. Chisté, C. Dulieu, E. Browne, C. Baglin, V. Chechev, N. Kuzmenko, R. Helmer, F. Kondev, D. MacMahon, and K. Lee. *Table of*

Radionuclides, volume 3 of *Monographie BIPM-5*. Bureau International des Poids et Mesures, Pavillon de Breteuil, F-92310 Sèvres, France, 2006. ISBN 92-822-2218-7. URL `http://www.bipm.org/utils/common/pdf/monographieRI/Monographie_BIPM-5_Tables_Vol3.pdf`.

[7] M.-M. Bé, V. Chisté, C. Dulieu, X. Mougeot, E. Browne, V. Chechev, N. Kuzmenko, F. Kondev, A. Luca, M. Galán, A. Nichols, A. Arinc, and X. Huang. *Table of Radionuclides*, volume 5 of *Monographie BIPM-5*. Bureau International des Poids et Mesures, Pavillon de Breteuil, F-92310 Sèvres, France, 2010. ISBN 92-822-2234-8. URL `http://www.bipm.org/utils/common/pdf/monographieRI/Monographie_BIPM-5_Tables_Vol5.pdf`.

[8] J. Beringer, J. F. Arguin, R. M. Barnett, K. Copic, O. Dahl, D. E. Groom, C. J. Lin, J. Lys, H. Murayama, C. G. Wohl, and et al. Review of Particle Physics. *Phys. Rev. D*, 86(1), Jul 2012. ISSN 1550-2368. doi: 10.1103/physrevd.86.010001. URL `http://dx.doi.org/10.1103/PhysRevD.86.010001`.

[9] R. Birkeland, T. Stein, et al. The NUTS CubeSat Project: Spin-offs and Technology Development. In *Proceedings of the 22nd ESA Symposium on European Rocket and Balloon Programmes and Related Research*, ESA Special Publication. ESA, 2015.

[10] C. Boggs, A. Doak, and F. Walls. Measurement of voltage noise in chemical batteries. In *Frequency Control Symposium, 1995. 49th., Proceedings of the 1995 IEEE International*, pages 367–373, May 1995. doi: 10.1109/FREQ.1995.483923. URL `http://tf.nist.gov/timefreq/general/pdf/1133.pdf`.

[11] E. Browne. Nuclear Data Sheets for A = 90. *Nuclear Data Sheets*, 82(3):379–546, Nov 1997. ISSN 0090-3752. doi: 10.1006/ndsh.1997.0021. URL `http://dx.doi.org/10.1006/ndsh.1997.0021`.

[12] E. Buchen. SpaceWorks 2014 Nano/Microsatellite Market Assessment (SSC14-I-3). *Proceedings of the AIAA/USU Conference on Small Satellites*, pages 1–5, 2014. URL `http://digitalcommons.usu.edu/smallsat/2014/PrivEnd/3/`.

[13] CalPoly CubeSat Lab. CubeSat Information - Developers, 2015. URL `http://www.cubesat.org/index.php/documents/developers`.

[14] S. R. Cherry, J. A. Sorenson, and M. E. Phelps. *Physics in Nuclear Medicine*. Elsevier Health Sciences, fourth edition, 2012. ISBN 978-1-4160-5198-5. doi: 10.1016/B978-1-4160-5198-5.00033-2.

[15] P. P. Chu. *FPGA prototyping by VHDL examples: Xilinx Spartan-3 version*. John Wiley & Sons, 2008. ISBN 9780470185315.

[16] A. H. Compton. A quantum theory of the scattering of X-rays by light elements. *Physical review*, 21(5):483, 1923.

[17] V. Damme. Data sheet: Van Damme - Pro Grade Classic XKE Pro-patch cable. Technical report, Van Damme, 2014. URL `http://www.van-damme.com/_pdf/16%20Pro%20Grade%20Classic%20XKE%20Pro-patch%20cable.pdf`.

[18] O. E. Design. 2nd order CR Low-pass Filter Design Tool, 2015. URL `http://sim.okawa-denshi.jp/en/CRCRkeisan.htm`.

[19] Doulos. Synchronization and Edge-detection, 2014. URL `https://www.doulos.com/knowhow/fpga/synchronisation/`.

[20] P. Dubock, F. Spoto, J. Simpson, D. Spencer, E. Schutte, and H. Sontag. The Envisat satellite and its integration. *ESA bulletin*, 106:26–45, 2001. URL `http://www.esa.int/esapub/bulletin/bullet106/bul106_2.pdf`.

[21] Duracell. Data sheet: 9V Duracell MN1604 6LR61 battery. Technical report, Duracell. URL `http://ww2.duracell.com/media/en-US/pdf/gtcl/Product_Data_Sheet/NA_DATASHEETS/MN1604_6LR61_US_CT.pdf`.

[22] Eveready. Data sheet: 22.5V Eveready 412 battery. Technical report, Energizer. URL `http://www.mouser.com/ds/2/133/412-11961.pdf`.

[23] G. Factory. Papilio One Hardware, 2013. URL `http://papilio.cc/index.php?n=Papilio.PapilioOne`.

[24] F. Flakus. Detecting and Measuring Ionizing Radiation - A Short History. *IAEA bulletin*, 23(4):31–36, 1982.

[25] B. C. Gabrielson and M. J. Reimold. Suppression of powerline noise with isolation transformers. *EMC EXPO87 San Diego*, 1987.

[26] D. Griffiths. *Introduction to elementary particles*. John Wiley & Sons, second edition, 2008. ISBN 978-3527406012.

[27] C. Grupen and I. Buvat. *Handbook of particle detection and imaging*. Springer Science & Business Media, 2011. ISBN 978-3-642-13270-4. doi: 10.1007/978-3-642-13271-1.

[28] C. Grupen and B. Shwartz. *Particle Detectors*, volume 26. Cambridge Univ. Press, 2nd edition, 2008. ISBN 9780521840064.

[29] N. Guerrini, R. Turchetta, D. Griffin, T. Morse, A. Morse, O. Poyntz-Wright, S. Woodward, E. Daly, A. Menicucci, H. Araujo, and et al. Design and characterisation of a highly miniaturised radiation monitor HMRM. *Nuclear Instruments and Methods in Physics Research Section A: Accelerators, Spectrometers, Detectors and Associated Equipment*, 731:154–159, Dec 2013. ISSN 0168-9002. doi: 10.1016/j.nima.2013.06.073. URL `http://dx.doi.org/10.1016/j.nima.2013.06.073`.

[30] J. H. Hubbell and S. M. Seltzer. Tables of X-ray mass attenuation coefficients and mass energy-absorption coefficients 1 keV to 20 MeV for elements Z= 1 to 92 and 48 additional substances of dosimetric interest. Technical report, National Inst. of Standards and Technology-PL, Gaithersburg, MD (United States). Ionizing Radiation Div., 1995. URL `http://www.nist.gov/pml/data/xraycoef/`.

[31] IEEE. IEEE Standard Multivalue Logic System for VHDL Model Interoperability (Stdlogic1164). *IEEE Std 1164-1993*, 1993. doi: 10.1109/IEEESTD.

1993.115571. URL `http://ieeexplore.ieee.org/servlet/opac?punumber=2823`.

[32] IEEE. IEEE Standard VHDL Mathematical Packages. *IEEE Std 1076.2-1996*, 1997. doi: 10.1109/IEEESTD.1997.81589.

[33] IEEE. IEEE Standard VHDL Language Reference Manual. *IEEE Std 1076-2008 (Revision of IEEE Std 1076-2002)*, pages 1–626, Jan 2009. doi: 10.1109/IEEESTD.2009.4772740.

[34] ISO. ISO 261:1998 - ISO general purpose metric screw threads - General plan, 1998. URL `http://www.iso.org/iso/iso_catalogue/catalogue_tc/catalogue_detail.htm?csnumber=4165`.

[35] O. Klein and Y. Nishina. Über die Streuung von Strahlung durch freie Elektronen nach der neuen relativistischen Quantendynamik von Dirac. *Zeitschrift für Physik*, 52(11-12):853–868, Nov 1929. ISSN 0044-3328. doi: 10.1007/bf01366453. URL `http://dx.doi.org/10.1007/BF01366453`.

[36] G. F. Knoll. *Radiation detection and measurement*. John Wiley & Sons, fourth edition, 2010. ISBN 978-0470131480.

[37] F. Leens. An introduction to I^2C and SPI protocols. *Instrumentation Measurement Magazine, IEEE*, 12(1):8–13, February 2009. ISSN 1094-6969. doi: 10.1109/MIM.2009.4762946.

[38] LEMO. Overview and data sheet: LEMO K Connector (Push-Pull self-latching). Technical report, LEMO, 2014. URL `http://www.lemo.com/en/standard-range/k-connector`.

[39] X. Li, Q. Schiller, L. Blum, S. Califf, H. Zhao, W. Tu, D. L. Turner, D. Gerhardt, S. Palo, S. Kanekal, and et al. First results from CSSWE CubeSat: Characteristics of relativistic electrons in the near-Earth environment during the October 2012 magnetic storms. *Journal of Geophysical Research: Space Physics*, 118(10):6489–6499, Oct 2013. ISSN 2169-9380. doi: 10.1002/2013ja019342. URL `http://dx.doi.org/10.1002/2013JA019342`.

[40] B. Mealy and F. Tappero. Free Range VHDL - The no-frills guide to writing powerful code for your digital implementations., 2013. URL `http://www.freerangefactory.org/site/pmwiki.php/Main/DownloadBooks`.

[41] D. Meier. VATA465 Datasheet (NGRM-IDEAS-DS-0003, Rev. 1.4). 2014. URL `http://www.ideas.no/`.

[42] E. F. Mitchell, H. M. Arajo, E. Daly, N. Guerrini, S. Gunes-Lasnet, D. Griffin, A. Marshall, A. Menicucci, T. Morse, O. Poyntz-Wright, R. Turchetta, and S. Woodward. The Highly Miniaturised Radiation Monitor. 2014. URL `http://arxiv.org/abs/1401.3533`.

[43] A. Mohammadzadeh, H. Evans, P. Nieminen, E. Daly, P. Vuilleumier, P. Buhler, C. Eggel, W. Hajdas, N. Schlumpf, A. Zehnder, et al. The ESA Standard Radiation

Environment Monitor program first results from PROBA-I and INTEGRAL. *IEEE Transactions on Nuclear Science*, 50(6):2272–2277, 2003.

[44] G. Nelson and D. Reilly. Gamma-ray interactions with matter, 1991. URL `www.lanl.gov/orgs/n/n1/panda/00326397.pdf`.

[45] K. Olive. Review of Particle Physics. *Chinese Physics C*, 38(9):090001, Aug 2014. ISSN 1674-1137. doi: 10.1088/1674-1137/38/9/090001. URL `http://dx.doi.org/10.1088/1674-1137/38/9/090001`.

[46] P. Pahlsson. VATA465 Validation Report (NGRM-TR-0003). 2014.

[47] V. A. Pedroni. *Circuit design and simulation with VHDL*. The MIT Press, 2010. ISBN 978-0262014335.

[48] W. H. Press, S. A. Teukolsky, W. T. Vetterling, and B. P. Flannery. *Numerical Recipes in C*, volume 2. Cambridge university press Cambridge, 1996.

[49] E. Reilly and K. Smith, editors. *Passive Nondestructive Assay Manual-PANDA*. 1991. ISBN 0-16-032724-5. URL `http://www.lanl.gov/orgs/n/n1/panda/`.

[50] A. Savitzky and M. J. E. Golay. Smoothing and Differentiation of Data by Simplified Least Squares Procedures. *Analytical Chemistry*, 36(8):1627–1639, Jul 1964. ISSN 1520-6882. doi: 10.1021/ac60214a047. URL `http://dx.doi.org/10.1021/ac60214a047`.

[51] B. Segret, J. Vannitsen, M. Agnan, A. Porquet, O. Sleimi, F. Deleflie, J.-J. Miau, J.-C. Juang, and K. Wang. BIRDY: an interplanetary CubeSat to collect radiation data on the way to Mars and back to prepare the future manned missions. In *SPIE Astronomical Telescopes+ Instrumentation*, pages 91501N–91501N. International Society for Optics and Photonics, 2014. doi: 10.1117/12.2056114.

[52] H. Spieler. *Semiconductor detector systems*, volume 12. Oxford university press, 2005. ISBN 978-0-19-852784-8.

[53] T. Stein et al. Student Experiment Documentation (SED) for BEXUS: CPT-SCOPE, version 2.1. 2015.

[54] T. A. Stein. Report for Physics - Special Syllabus (FY3490): Characterisation of the IDEAS ASIC VATA465 with focus on temperature and input-signal frequency response. 2014.

[55] T. A. Stein. CubeSat-ready Radiation Monitor Front-End Electronics. 2014. URL `https://www.cubesatsymposium.eu/`.

[56] STMicroelectronics. Technical note (TN0897): ST SPI protocol (Rev. 2). Technical report, STMicroelectronics, 2013. URL `http://www.st.com/st-web-ui/static/active/en/resource/technical/document/technical_note/DM00054618.pdf`.

[57] J. Sullivan. Geometric factor and directional response of single and multi-element particle telescopes. *Nuclear Instruments and methods*, 95(1):5–11, 1971.

[58] S. Techniques. Disc and Laminated Sources, 2015. URL `http://spectrumtechniques.com/disc&laminated_sources.htm`.

[59] C. P. S. The CubeSat Program. CubeSat Design Specification (CDS), Rev. 13, 2015. URL `http://www.cubesat.org/images/developers/cds_rev13_final2.pdf`.

[60] A. C. Thompson et al. *X-Ray Data Booklet*. LBNL, third edition, 2009. URL `http://xdb.lbl.gov/`.

[61] E. Tutorials. Passive Low Pass Filter, 2015. URL `http://www.electronics-tutorials.ws/filter/filter_2.html`.

[62] WIMA. Data sheet: WIMA MKS 2 - Metalized Polyester (PET) capacitors. Technical report, WIMA, 2012. URL `http://www.wima.com/EN/WIMA_MKS_2.pdf`.

[63] WIMA. Data sheet: WIMA FKP 2 - Polypropylene (PP) Film and Foil capacitors. Technical report, WIMA, 2012. URL `http://www.wima.com/EN/WIMA_FKP_2.pdf`.

[64] Xilinx. Application Note: Spartan-3 FPGA Series, Using Look-Up Tables as Shift Registers (SRL16) in Spartan-3 Generation FPGAs (XAPP465, v1.1). Technical report, Xilinx, 2005. URL `http://www.xilinx.com/support/documentation/application_notes/xapp465.pdf`.

[65] Xilinx. Spartan-3E FPGA Family Data Sheet, v.4.1. Technical report, 2013. URL `http://www.xilinx.com/support/documentation/data_sheets/ds312.pdf`.

Appendix

Measurement data

Distance measurement

Table 5.1: Count rate R as function of distance d for the Am-241 source (ID: 1). The respective error in position and count rate is also given.

d **/ mm**	Δd **/ mm**	R **/ cps**	ΔR **/ cps**
109.0	0.5	78.8	2.0
99.0	0.5	93.3	3.5
94.0	0.5	103.7	3.4
89.0	0.5	117.3	2.5
86.0	0.5	121.3	3.8
79.0	0.5	144.7	4.1
74.0	0.5	164.2	1.8
69.0	0.5	191.5	3.2
66.5	0.5	204.1	5.1
59.0	0.5	253.6	5.6
54.0	0.5	304.5	5.4
49.0	0.5	365.7	6.3
97.5	0.5	95.5	3.1
90.0	0.5	113.2	3.3
85.0	0.5	126.6	4.1
80.0	0.5	143.4	3.5
56.0	0.5	281.0	5.7
49.0	0.5	367.5	6.7
44.0	0.5	447.5	6.4
39.0	0.5	566.7	6.2
36.0	0.5	645.6	9.3
29.0	0.5	953.0	8.3
23.5	0.5	1263.3	11.8
17.0	0.5	1793.5	11.7

Time Series Data

No target

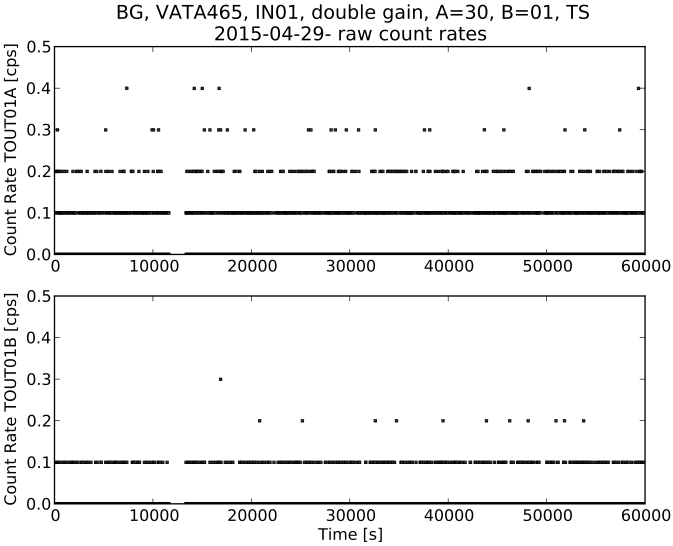

Figure 5.1: Time series graphs (BG): ID1 - 2015-04-29 (no target).

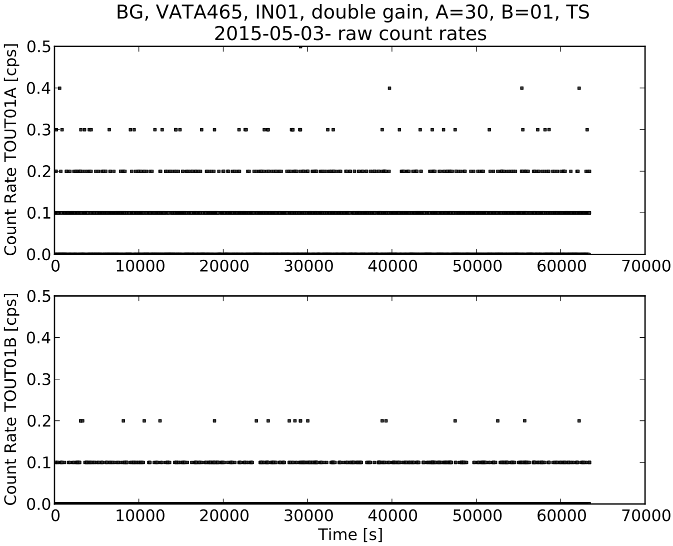

Figure 5.2: Time series graphs (BG): ID2 - 2015-05-03 (no target).

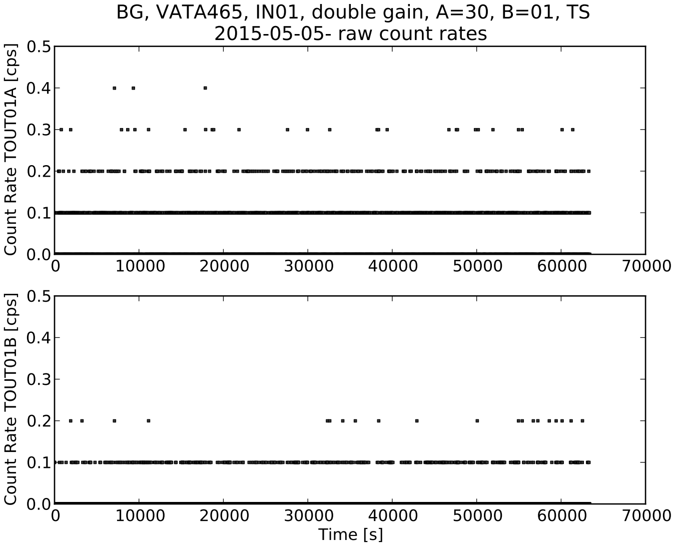

Figure 5.3: Time series graphs (BG): ID3 - 2015-05-05 (no target).

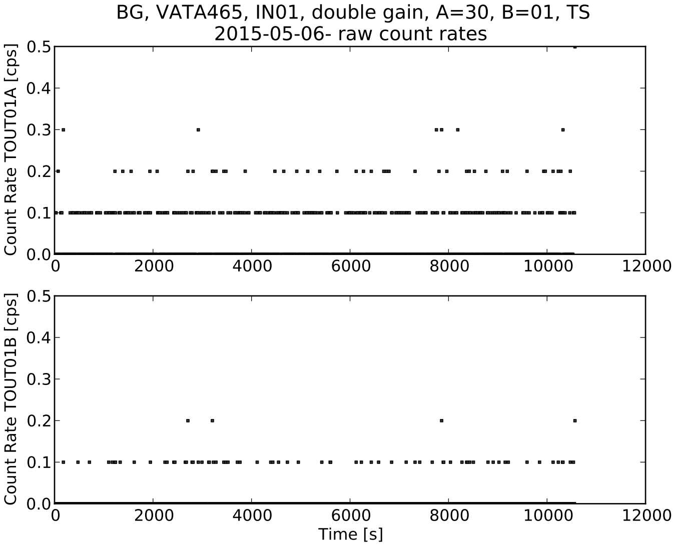

Figure 5.4: Time series graphs (BG): ID4 - 2015-05-06 (no target).

Single target

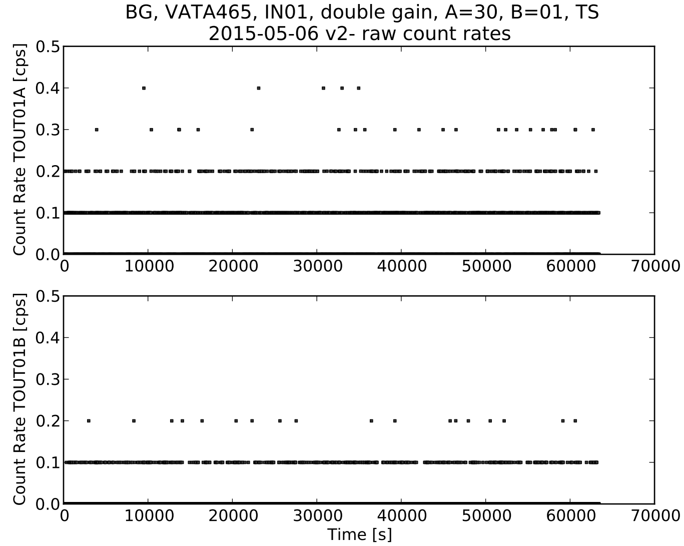

Figure 5.5: Time series graphs (BG): ID5 - 2015-05-06 v. 2 (no target).

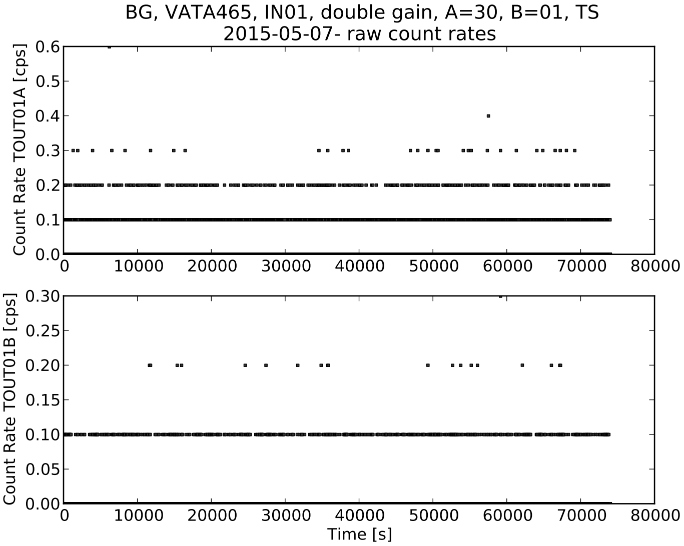

Figure 5.6: Time series graphs (BG): ID6 - 2015-05-07 (no target).

Double target

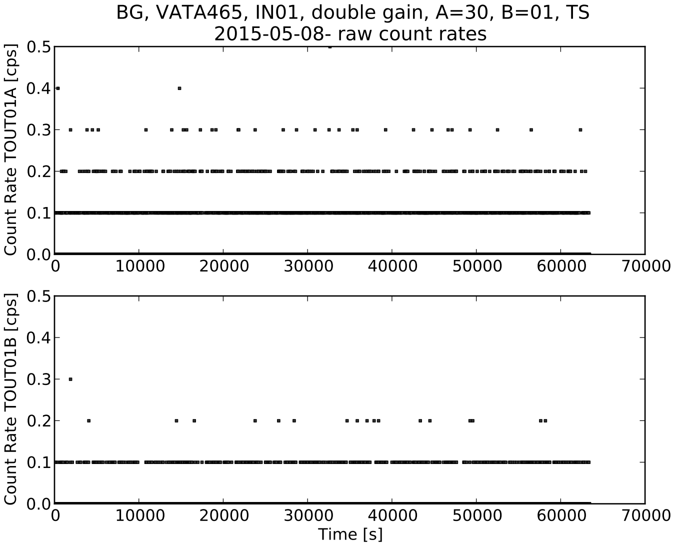

Figure 5.7: Time series graphs (BG): ID7 - 2015-05-08 (no target).

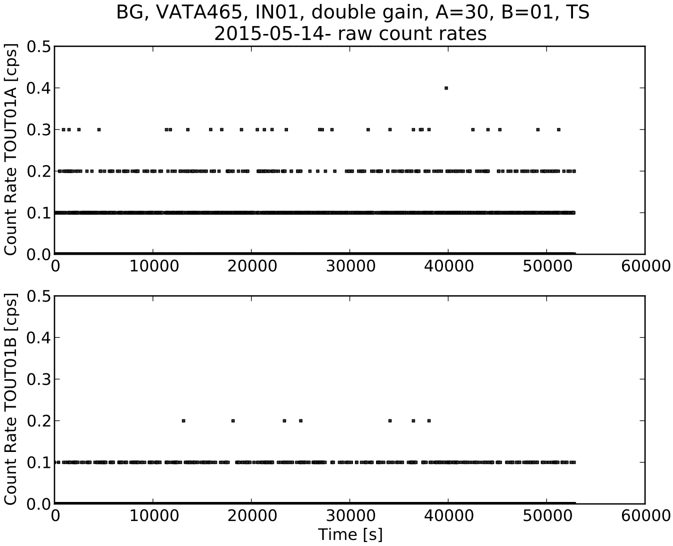

Figure 5.8: Time series graphs (BG): ID8 - 2015-05-014 (no target).

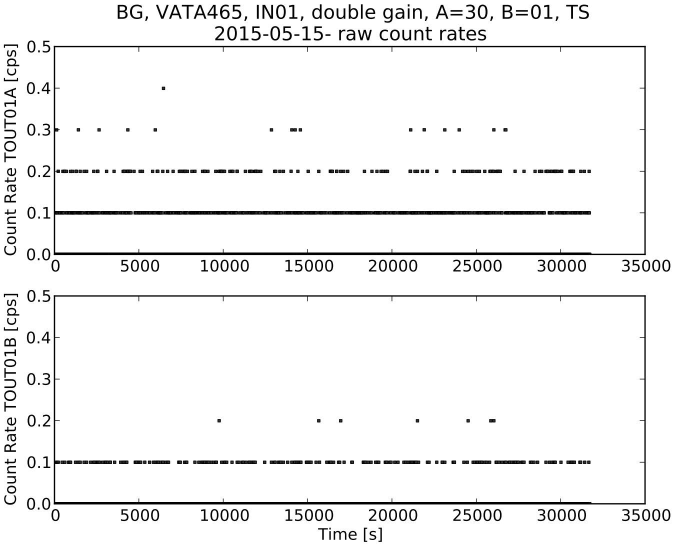

Figure 5.9: Time series graphs (BG): ID9 - 2015-05-015 (no target).

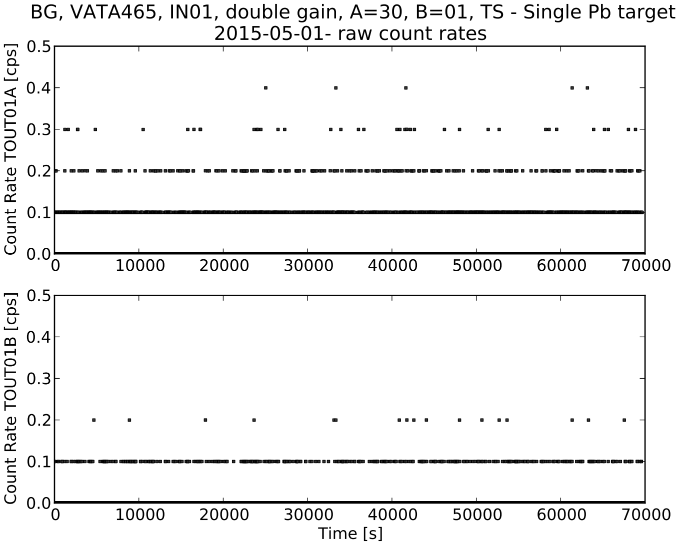

Figure 5.10: Time series graphs (BG): ID10 - 2015-05-01 (single target, A).

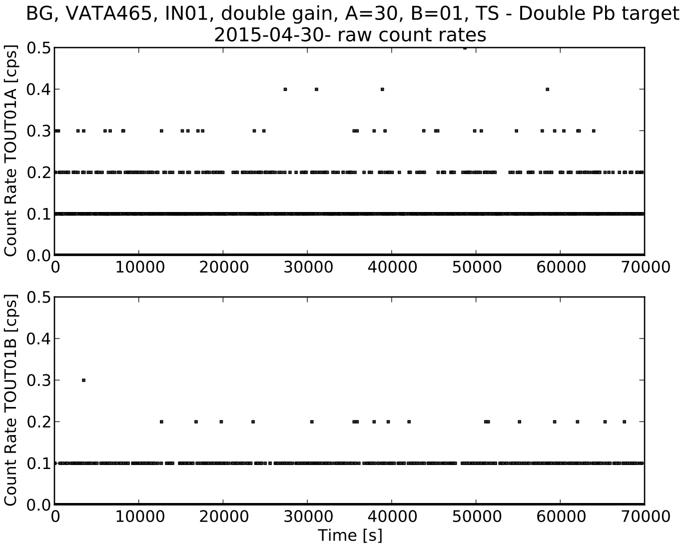

Figure 5.11: Time series graphs (BG): ID11 - 2015-04-30 (double target, A+B).

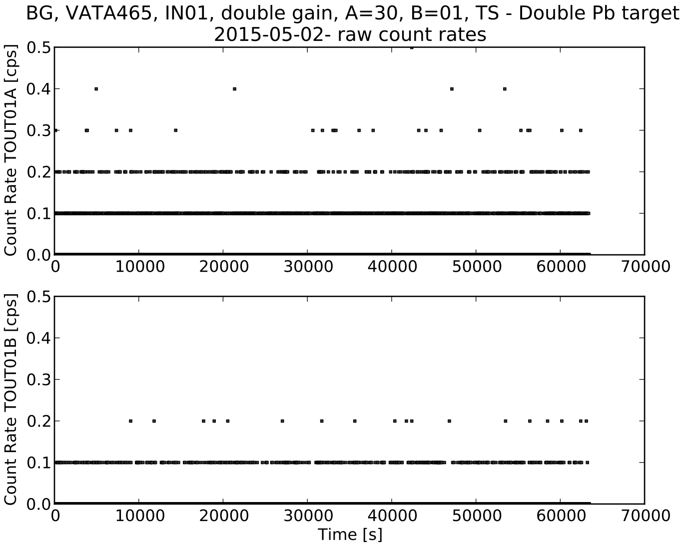

Figure 5.12: Time series graphs (BG): ID12 - 2015-05-02 (double target, A+B).